ELECTRON MICROSCOPY STUDY OF THE CHEMICAL AND STRUCTURAL EVOLUTION OF LITHIUM-ION BATTERY CATHODE MATERIALS

By

HANSHUO LIU, M.Eng

A Thesis
Submitted to the School of Graduate Studies
in Partial Fulfillment of the Requirements
for the Degree of
Doctor of Philosophy

McMaster University

DOCTOR OF PHILOSOPHY (2017)

Department of Materials Science and Engineering

McMaster University, Hamilton, Ontario, Canada

TITLE: Electron Microscopy Study of the Chemical and Structural Evolution of Lithium-Ion Battery Cathode Materials

AUTHOR: Hanshuo Liu, M.Eng

SUPERVISOR: Dr. Gianluigi A. Botton

NUMBER OF PAGES: xv, 157

ABSTRACT

Layered lithium transition metal oxides represent a major type of cathode materials that are widely used in commercial lithium-ion batteries. Nevertheless, these layered cathode materials suffer structural changes during electrochemical cycling that could adversely affect the battery performance. Clear explanations of the cathode degradation process and its initiation, however, are still under debate and are not yet fully understood. In this thesis, the cycling-induced chemical and structural evolution of $LiNi_{1/3}Mn_{1/3}Co_{1/3}O_2$ (NMC) and high-energy $Li_{1.2}Ni_{0.13}Mn_{0.54}Co_{0.13}O_2$ (HENMC) cathodes are investigated in details using state-of-the-art electron microscopy techniques combined with other bulk measurements to uncover the mechanisms at the source of cell deterioration.

Using high-resolution electron energy loss spectroscopy (HR-EELS), the role of transition metals (TMs) of NMC cathode material in the charge compensation process at different state-of-charges (SOCs) is clarified. The cathode evolution is studied in details from the first-charge to long-term cycling using EELS, aberration-corrected scanning transmission electron microscope (STEM) and complementary diagnostic tools. The results reveal that the surface degradation of NMC initiates in the first-charging stage with a surface reduction layer formed at particle surface. Besides the study on NMC, the degradation mechanism of a promising cathode material candidate, high-energy Li-rich layered oxide (HENMC), is investigated thoroughly. In addition to demonstrating the surface degradation of HENMC during cycling, we clearly reveal the drastic evolutions from the cathode interior. Instead of attributing the overall performance decay to the surface evolution, our findings uncover the complexed transitions in the bulk material, which are potentially the main sources for the rapid performance decay of Li-rich cathodes.

As complement to two-dimensional (2D) characterization, the three-dimensional (3D) microstructure of pristine and cycled NMC and HENMC cathodes are also analyzed using focused ion beam-scanning electron microscopy (FIB-SEM) 3D reconstruction. The spatial distribution of active material, carbon-doped binder and pore spaces are successfully reconstructed by appropriate image processing. Meanwhile, the connectivity between carbon-doped binder phase and active material phase in NMC and HENMC cathodes, assessed using a “neighbor counting” method, showed an appreciable decrease after cycling which indicates a detachment of carbon-doped binder from active particles.

ACKNOWLEDGEMENTS

It has been a challenging and enjoyable journey for me in pursuing the Ph. D degree during the past years. I would like to take this opportunity to express my gratitude to the people who helped and supported me during these years.

My deepest gratitude goes first and foremost to my supervisor, Dr. Gianluigi Botton, who has always been supportive throughout my Ph. D study. I benefit a lot from your profound knowledge of electron microscopy. Your rigorous academic attitude and endless pursuit for high quality research set a good example for my future career. My sincere thanks to your invaluable advices and patient instructions on my research projects. Without your constant help and guidance, this work would not be completed.

I am truly thankful to my supervisory committee members, Dr. Gillian Goward and Dr. Anthony Petric, for your encouragements, constructive advices and insightful comments on my research.

I am sincerely grateful to my collaborators in the APC project for lithium-ion battery research, Dr. Gillian Goward and her group members (Dr. Kristopher Harris, Mark Dunham, Matteo Tessaro, Dr. Sergey Krachkovskiy), Dr. Bartosz Protas and his group members (Dr. Jamie Foster and Dr. Adam Gully), Dr. Meng Jiang and Dr. Yan Wu from General Motors, who made great contributions to this thesis and provided generous help and support on my research. I would also like to thank my other collaborators, Dr. Xueliang Sun and Biwei Xiao from Western University, Dr. Jeff Dahn and Jing Li from Dalhousie University, Dr. Ion Halalay from General Motors. I am very honored to work with you all.

I am greatly indebted to Dr. Matthieu Bugnet for training me on the spectroscopic instruments and helping me with other microscopy issues. Many thanks to your encouragements, valuable suggestions and the extensive discussions we had on my work. I would like to thank Dr. Andreas Korinek and Dr. Carmen Andrei for training me on the TEM instruments, Dr. Glynis de Silveira and Chris Butcher for training me

on the SEM instruments, Travis Casagrande and Andy Duft for helping me on the sample preparation.

I am very glad and fortunate of joining the Microscopy of Nanoscale Materials group. Here, I met a bunch of people who are talented and enthusiastic. Special thanks to some former and senior members, Edson Bellido, Sagar Prabhudev, Samantha Stambula, Steffi Woo, Guozhen Zhu and David Rossouw, for always being helpful and supportive during the years of my Ph. D study.

Finally, I would like to thank my dear parents and my husband Siwei Ma for supporting me on pursuing the Ph. D degree. Thank you for your unconditional support and encouragements.

OUTLINE

LIST OF FIGURES

LIST OF TABLES

LIST OF ABBREVIATIONS AND SYMBOLS

β	Collection Semi-Angle
λ	Radiation Wavelength
ϵ	Dielectric Constant
μ	Refractive Index
σ	Cross Section
θ	Scattering Angle
E^0	Standard Potential
Ec	Critical Ionization Energy
ΔG	Change in Gibbs Free Energy
Z	Atomic Number
ADF	Annular Dark Field
CEI	Cathode Electrolyte Interface
DOS	Density of State
DP	Diffraction Pattern
EDX	Energy Dispersive X-ray Spectrometry
EELS	Electron Energy Loss Spectroscopy
EV	Electric Vehicles
FIB	Focused Ion Beam
HAADF	High Angle Annular Dark Field
HEV	Hybrid Electric Vehicles
HENMC	High-Energy NMC ($Li_{1.2}Ni_{0.13}Mn_{0.64}Co_{0.13}O_2$)
MATPASS	Magic Angle Turning Phase Adjusted Spinning Sideband
MLLS	Multiple Linear Least Square
NBED	Nano Beam Electron Diffraction
ND	Neutron Diffraction

NMC	$LiNi_xMn_yCo_{1-x-y}O_2$
NMP	N-Methyl-2-Pyrrolidene
NMR	Nuclear Magnetic Resonance
PVDF	Polyvinylidene Fluoride
RS	Rock-Salt
SAED	Selected Area Electron Diffraction
SEI	Solid Electrolyte Interface
SEM	Scanning Electron Microscopy
SI	Spectrum Image
SOC	State of Charge
SRL	Surface Reconstruction Layer
STEM	Scanning Transmission Electron Microscopy
TEM	Transmission Electron Microscopy
TM	Transition Metal
XAS	X-ray Absorption Spectroscopy
XRD	X-ray Diffraction
ZLP	Zero-Loss Peak

Chapter 1

Introduction

Ever since the development of engine technology in 17th century, fossil fuels have been extensively utilized as primary energy sources. So far, the majority of energy is still being supplied by fossil fuels. With the increasing need for energy, the demand of fossil fuels is growing. Such fuels, however, are not renewable as they requires millions of years to form. On one hand, the continuous consumption of these non-renewable energy resources will eventually lead to price increases, thus, the threat of global energy resources depletion would eventually obstruct the development of human society. On the other hand, with increasing attention to the global warming issue, it has been realized that one of the major causes of greenhouse gas emission is the combustion of fossil fuels. Carbon dioxide is a main greenhouse gas produced by burning fossil fuels, such as, oil, gas and coal. Meanwhile, fossil fuel combustion also produces sulfur dioxide, carbon monoxide, nitrogen dioxide, which are all detrimental to the environment.

With these concerns, researchers try to find alternative energy sources that can complement or replace fossil fuels, such as nuclear and renewable sources. The challenges associated with nuclear energy is the storage of radioactive waste which will last for thousands of years, bringing serious safety concerns. Renewable sources, such as solar and wind, are sustainable and environmental friendly, however, they are intermittent and cyclic in nature. Therefore, these energy sources cannot be easily built into portable forms. Unlike these renewable sources, the electric energy storage systems, such as batteries, can be used whenever needed, thus play an indispensable role in people's everyday life. Batteries are one form of electric energy storage systems that convert chemical energy into electricity.[1] With a large number of applications in portable electronic devices, back-up energy supply for electric grids and the recent development of plug-in/hybrid-electric vehicles (P/HEVs) and electric vehicles (EVs), lithium-ion batteries have become one of the most promising electrical storage systems because of their high volumetric and gravimetric energy density. Nevertheless, the rapid development of automotive electrification, consumer electronics, and even aircrafts requires lithium-ion battery systems to provide higher energy-density, longer cycle life, and lower cost. The necessity for such battery systems strongly depends on the development of electrode materials that can deliver higher specific energy and possess improved structural and chemical stability. Advances in electrode materials' development therefore become one of the most important tasks in lithium-ion battery research.

Lithium-ion battery electrodes are known to suffer structural changes during electrochemical cycling that leads to capacity fade which would influence the stability and lifetime of the battery. As a major component in lithium-ion battery, the cathode plays a key role in the battery performance since it provides the Li ions source in a lithium-ion battery configuration in most of the cases. Although cathodes do not exhibit large volume changes during Li intercalation-deintercalation process compared to anodes,[2,3] they suffer irreversible structural reconstruction, electrode-electrolyte side reactions and chemical evolution during cycling, which adversely affect the performance of the battery. Hence, the work carried out in this thesis is focused on the exploration of the possible mechanisms at the origins of the degradation of lithium-ion battery cathodes.

In this thesis, the chemical evolution and structural change of layered structured cathodes during electrochemical cycling are thoroughly investigated from two-dimensional (2D) and three-dimensional (3D) perspectives using different state-of-the-art microscopy techniques, aiming to unravel the degradation mechanism of lithium-ion battery cathodes. Chapter 2 introduces the history of different battery technologies and the fundamentals of lithium-ion battery system. The development of batteries, from the first primary battery system to the recent development of secondary batteries, are introduced. More information on the working principle and application of lithium-ion batteries are described in this chapter. Moreover, the development and challenges in different types of lithium-ion battery cathodes are discussed in detail. In Chapter 3, the basics of transmission electron microscopy (TEM) and its application in the study of lithium-ion battery cathodes are discussed. The fundamentals and instrument information related to analytical TEM are introduced in this chapter. A review on the charge compensation mechanism of layered lithium transition metal oxides with different compositions during lithiation-delithiation process is included. Meanwhile, previous studies on the cycling-induced evolutions of layered cathode involving phase transformation and chemical changes are summarized and discussed.

Chapter 4 and 5 mainly demonstrate the results on the structural and chemical evolutions on two different layered cathode materials: $LiNi_{1/3}Mn_{1/3}Co_{1/3}O_2$ (NMC) and high-energy $Li_{1.2}Ni_{0.13}Mn_{0.54}Co_{0.13}O_2$ (HENMC). Layered lithium transition metal oxides are some of the most important types of cathode materials in lithium-ion batteries. Nevertheless, these layered cathode materials suffer performance deterioration during electrochemical cycling, whereas the origins of such degradation have not yet been fully understood. In Chapter 4, results of the study on charge compensation process of NMC during charge-discharge using spatially-resolved electron energy-loss spectroscopy (EELS) are demonstrated. The structural and chemical evolution of NMC cathode during long-term cycling are investigated in order to unravel the performance deterioration of the cell. In Chapter 5, the structural and chemical evolutions of a promising cathode candidate, HENMC, which possesses exceptional high capacity but suffers rapid performance decay, is fully investigated. A detailed study on the structure and composition of pristine HENMC cathode material is performed. With a better understanding of the starting material, the phase transformation and chemical evolution of HENMC during the first and extended cycles are investigated thoroughly from the surface to the bulk, revealing the possible failure mechanisms of this layered high-energy cathode.

Although we have obtained a wealth of useful information from 2D perspective in understanding the performance decay of the layered cathodes, a complementary 3D investigation on the structural evolution of the cathodes is still of great importance. Thus, in Chapter 6, a study on the 3D microstructural evolution of NMC and HENMC cathodes using state-of-the-art focused ion beam-scanning electron microscopy (FIB-SEM) 3D reconstruction is presented. The spatial distribution of the three phases: active material; carbon-doped binder; and pore spaces within the cathode is clearly resolved in 3D. The particle size distribution and the connectivity between the carbon-binder phase and active particles in both cathodes are evaluated from the reconstructed model.

At the end of the thesis, Chapter 7 concludes the work completed in this thesis. The suggested future work and possible applications of TEM in the study of lithium-ion battery are discussed in Chapter 8.

Chapter 2

Overview of Lithium-Ion Batteries

Lithium-ion batteries are promising energy storage systems that have been widely used in people's everyday life. The presence of lithium-ion battery enables the proliferation of portable electronic devices due to its high volumetric and gravimetric energy density comparing to the conventional nickel-cadmium (Ni-Cd), nickel-metal hydride (Ni-MH), and lead-acid secondary battery systems. These characteristics also promote the blooming of automotive industry, while, on the other hand, the development of hybrid electric and electric vehicles (HEVs/EVs) places stringent demand on battery systems that enable higher energy density, longer cycle-life, better safety, and lower cost. With these concerns, lithium-ion batteries with different electrode systems, such as graphite/$LiCoO_2$, graphite/$LiFePO_4$, $Li_4Ti_5O_{12}$/$LiMn_2O_4$, etc. have been developed, and the exploration of new electrode materials are still ongoing. In this chapter, an overview of battery history and working principle of lithium-ion batteries are introduced. The development and challenges in lithium-ion battery positive electrode, or cathode, are being discussed.

2.1 Basics of Batteries

An electrochemical cell is a device that converts the chemical energy stored in the active materials into electrical energy by means of electrochemical redox reactions, which is also referred to as a galvanic cell.[4] A battery usually consists of multiple electrochemical cells, although it may also represent a single cell under some circumstances. In an electrochemical cell, the material with lower standard electrode potential is defined as the negative electrode or anode, which is oxidized during discharge and gives up electrons through external circuit. On the contrary, the material with higher standard electrode potential is called positive electrode or cathode, which is reduced during discharge process and accepts electrons from the external circuit. The electrolyte is an ionic conductor, which acts as a medium for ion transfer between the anode and cathode inside the cell. Practically, the anode and cathode are physically isolated by a separator to prevent internal short circuit, while the separator is permeable to electrolyte so that the ions are able to transfer between the two electrodes and maintains a good ionic conductivity. The galvanic reaction can occur spontaneously when the two electrodes with different standard potentials are connected through an external electronic load as the reaction leads to a decrease in the free energy of the whole system ($\Delta G < 0$).

The theoretical standard voltage ($E^0(cell)$) of a galvanic cell can be basically determined by the difference between the standard electrode potential of the cathode ($E^0(cathode)$) and the anode ($E^0(anode)$) by the equation:

$$E^0(cell) = E^0(cathode) - E^0(anode) \tag{2.1}$$

Equation 2.1 can be further modified by taken into account of the nonstandard state of the reacting components in order to evaluate the actual open circuit potential for a battery at fully charged state as:

$$E = E^0(cell) - RTlnQ \tag{2.2}$$

where Q is the reaction quotient for the overall chemical reaction, $Q=\frac{a_{re}}{a_{ox}}$, where a is the chemical activity for the reactants and products in the reaction. R is the gas constant

(R=8.31 J/kmol).[4] The operation voltage of a cell is lower than the theoretical potential as a result of polarization during the reaction and the IR drop (I denotes the current generated during reaction and R represents the cell internal resistance), of course, the actual operating voltage needs to be sufficient for the intended application.

Depending on whether the batteries can be electrically recharged or not, they can be classified into two categories: primary battery and secondary battery. A primary battery refers to a battery system that can only be used once, and is no longer available after its reactants are consumed by the discharge process. In contrast, a secondary battery is capable of reversible charge and discharge reactions with electrons transferred through the external electric circuit. The discharge reaction in a battery is thermadynamically favorable ($\Delta G < 0$) and occurs spontaneously, whereas in order to charge a secondary battery, a minimum potential needs to be applied to inverse the reaction, which can be calculated from:

$$\Delta \mathrm{G} = -\mathrm{nFE} \tag{2.3}$$

Where n is the number of positive charges carried by the ions transferred during the reaction, and F is Faraday’s constant. Therefore, if an electrical potential that larger than the voltage given off during discharge is applied to the cell, the charging reaction can take place. Once the cell is at fully charged state, the thermodynamically favorable discharge reaction may occur spontaneously when an electronic load is connected, thus, the secondary cell can be used repeatedly.

2.1.1 Full Cells and Half Cells

Depending on the choice of electrodes, the electrochemical cells fall into two categories: half cells and full cells. A half-cell is a cell that constructed with an electrode of interest (can be either an anode or a cathode) and a counter electrode used as a reference electrode, which facilitates the electrochemical test and the analysis of activities at different operation voltages. This is usually used for the investigation on the properties of certain electrode materials. In contrast, a full cell is a cell constructed in a complete form of an electrochemical cell, where the redox reactions occur at both the anode and cathode, and reflects the battery performance in a more realistic way.

2.1.2 Capacity

The theoretical capacity is referred to the total quantity of electricity that can be obtained through the electrochemical reaction of active materials, thus, the theoretical capacity is directly related with the amount of active materials in the cell. The unit for cell capacity is coulombs (C) or ampere-hours (Ah), and can be calculated by:

$$C = xF \tag{2.4}$$

where C is the theoretical capacity, x is the number of electrons being provided by the active material during discharge, in the unit of mole. F is Faraday’s constant. In the real battery configurations, the practical capacity is smaller than the theoretical value as the active components have not fully reacted during cycling, meanwhile, the parasitic reactions could also consume the active reactants in the cell.

2.1.3 Energy Density

The energy of a battery system is defined by both the quantity of electricity that can be delivered during the electrochemical process and the cell voltage:

$$\text{Watthour (Wh)} = \text{voltage (V)} \times \text{ampere-hour (Ah)} \tag{2.5}$$

The energy density is related directly with the specific capacity and voltage, which is usually measured in Wh/kg, Wh/g or Wh/l. In a real battery system, the theoretical energy density cannot be fully achieved because: (i) the weight or volume of the battery includes electrolyte and nonreactive components, such as current collector, separator, container, which adding up the total weight and volume of the battery; (ii) the operation voltage is not necessarily the same as the theoretical voltage, and the terminating discharge voltage may not reach the minimum, which lowering the average voltage.

2.2 History of Batteries

Historically, the first battery was introduced by an Italian researcher Volta in 1800, who invented the Voltaic Pile, in which an electric current is produced by connecting the two ends of a stack of two metals disks (zinc and copper) which are separated by a cloth or cardboard soaked in an alkaline solution (Figure 2.1).[5] This model is considered to be the first form of a battery. In 1836, a British chemist, John F. Daniel improved the Volta Pile and developed a battery system with Zn|ZnSO4||CuSO4|Cu configuration, which is then named as Daniel cell. The Daniel cell was capable of providing a voltage of 1.1 V and was used in the telegraph system.[4] With the development of battery technology, the initial zinc/copper electrode configuration has been gradually replaced by many other advanced battery systems, which will be described in the following content.

Figure 2.1 A photo of “Volta Pile”. From reference [4].

2.2.1 Primary Batteries

Although primary batteries are not capable of being recharged electrically and need to be discarded after fully discharge, they are convenient to use, inexpensive and usually lightweight. The primary batteries are widely used in portable electric devices, watches, digital cameras, toys, lighting, and a variety of other applications. They are easy to use, have good shelf life, acceptable energy density, reasonable cost, and require very little maintenance. The primary batteries can be manufactured in different forms in order to fit different devices. A number of anode and cathode combinations have been developed for primary battery systems ever since its discovery in 19th century, and some are still widely used in the commercial market.

Among all the primary battery systems, zinc has been a very important anode material because it is compatible with aqueous electrolytes and has good electrochemical behavior and shelf life. The first primary battery that has been widely used is the zinc-carbon battery, also known as Leclanché cell, invented by the French scientist Georges Leclanché in 1866.[4] In 1940s-1960, with the introduction of the new materials, such as manganese dioxide and zinc chloride electrolyte, the capacity and shelf life of this battery system were dramatically improved. During 1970-1990s, zinc/alkaline/manganese dioxide primary batteries replaced zinc-carbon batteries and became popular battery systems stimulated by the concurrent development of portable electronic devices. The zinc/mercuric oxide is another important primary battery with a zinc anode, which was developed during World War II. But this battery system is gradually phased out with the environmental concerns associated with mercury.

The zinc/air battery and battery system using other anode materials have been developed to replace the mercury battery system in many applications. The zinc/air battery has advantages of inexhaustible cathode reactant, high energy density, and low cost. However, the usage and storage of this system is restricted to the environmental conditions, such as temperature and humidity. The zinc/air battery was preliminary applied in signaling and navigational applications which require long-term and low rate discharge. With the development of this battery system into smaller button-type cells, the zinc/air battery has also been widely used in hearing aids and medical devices.

Aluminum is considered to be another attractive anode candidate because of its high standard potential and energy density, whereas, this material has not been successfully used in a commercial battery system. With the formation of a “protective” oxide film on the aluminum anode surface, the voltage that can be achieved by the primary battery is considerably lower than the theoretical value, meanwhile, it also leads to voltage delay of the battery. Although the film can be removed by using proper electrolytes, the accompanied corrosion issue result in poor shelf life and problems in long-term usage.

Magnesium is also an attractive anode material in battery system. It has high standard potential, low atomic weight, high energy density, and low cost. The magnesium primary batteries have been successfully used in commercial market in the system of magnesium/manganese dioxide (Mg/MnO_2). The advantages of this battery system are the higher voltage and doubled capacity comparing to that of zinc/carbon batteries. It also has good capacity retention under a wide temperature range during storage. However, the magnesium batteries have problems with voltage delay and parasitic reactions during discharge that lead to the generation of hydrogen and heat. The storage time will also be greatly reduced once the cell has been partially discharged, therefore, is not suitable for intermittent use. In recent years, the use of magnesium batteries in applications such as military equipment has ceased and they are being replaced by batteries with higher energy density and better rate capability, like lithium primary batteries and lithium-ion batteries

Due to the demand of high energy density of battery systems, the introduction of lithium as an anode material into a battery system has drawn increasing interest since 1970th. The first commercialized lithium primary battery with lithium/manganese dioxide configuration was released by Sanyo Electric Co. in 1975.[4] Lithium batteries have the advantage of high energy density, wide temperature range and long shelf life, whereas the application of lithium batteries are restricted by their high cost. The specific capacity of primary battery systems has been improved from about 50 Wh/kg for the early zinc/carbon batteries to more than 300 Wh/kg achieved by zinc/air and lithium primary batteries (Figure 2.2a). Although lithium primary batteries can provide high energy density, they cannot fully replace alkaline batteries in the commercial market, since the manufacturing of lithium battery is a high technology business due to the reactivity of lithium and requires much higher cost. Meanwhile, among all these primary battery systems, lithium primary batteries have the advantage of high working voltage close to or above 3 V depending on the choice of cathode, as shown in Figure 2.2b. In comparison, the commonly used zinc alkaline batteries have a discharge voltage range of 1.4 V to 0.9 V.

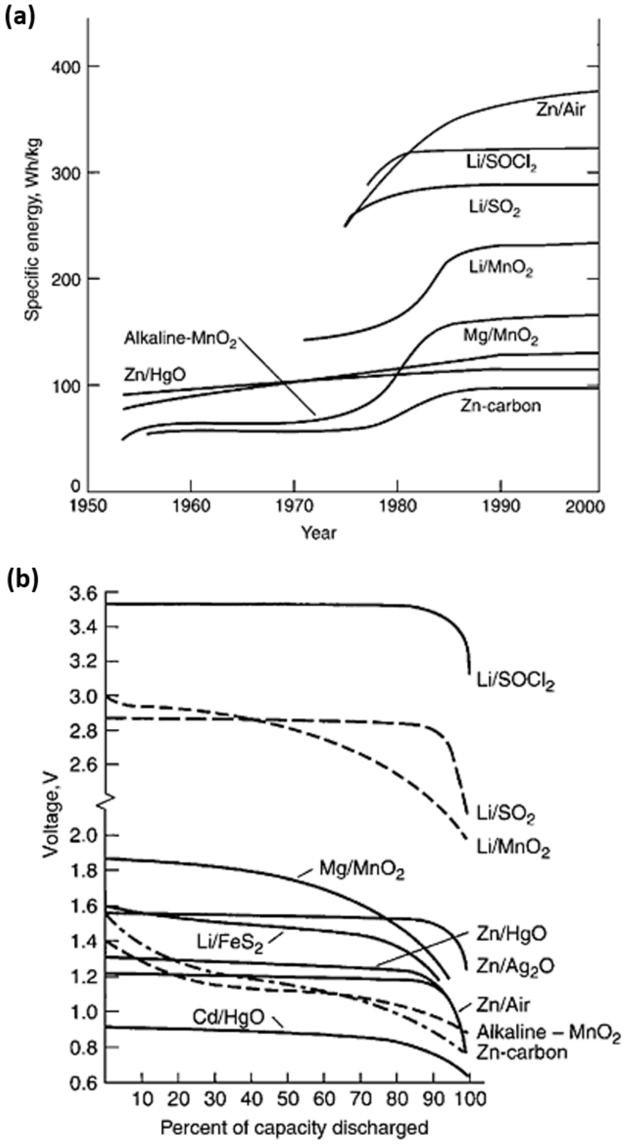

Figure 2.2 Comparison of cycling performances of different primary battery systems. (a) Development of specific energy of primary batteries in the 20th century. (b) Discharge profile of primary battery systems. From reference [6].

2.2.2 Secondary Batteries

In contrast to primary batteries, secondary batteries are systems that can be effectively reused multiple times. After being discharged, the secondary battery can be recharged by applying an external electrical power to promote the reversed reaction. Such a charge-discharge process is termed as an electrochemical cycle. Nevertheless, the cell cannot be used infinitely and needs to be discarded when the capacity drops below a certain level. Secondary batteries are widely used in many applications. One major applications are power sources for portable devices, such as tools, radio, lighting, and electronic devices, such as mobile phones, laptop computers, tablets, etc. Other common usages including starting, lighting and ignition (SLI) for automobiles, emergency and standby power. With the rapid development in automotive industry, secondary batteries have also been applied in hybrid electric or electric vehicles (H/EVs) as power sources.

There has been a long history for secondary batteries. The first rechargeable lead-acid battery was invented in 1859, by a French physicist Gaston Planté. The lead-acid battery has two electrodes that both consist of lead, and the electrolyte is acidic. The original lead-acid cell contains two lead electrode sheets, a spiral rolled separator and sulfuric acid electrolyte. During cycling, the lead electrodes will be corroded by electrolyte, leading to the formation of lead dioxide and spongy lead on the two electrodes, therefore, resulting in an increased capacity in the subsequent cycles. In 1880-1882, a new design of the lead-acid cell was developed by using lead as anode and a lead grid lattice with lead oxide-sulfuric acid pastes as cathode. There have been several improved lead-acid battery configurations designed after the plate grid, such as lead-antimony alloy grid and a lead-calcium grid. The lead-acid batteries are low cost, but also have relative low specific-energy density. The lead-acid batteries are commonly used in automotive applications for SLI, in e-bikes, uninterruptible power supplies, signaling, etc.

Another major category of secondary batteries are the alkaline secondary batteries that use an aqueous alkaline solution as electrolyte. Hence, the electrolyte is less reactive with the electrode materials compared to the acidic electrolyte. The first commercialized alkaline secondary battery is the nickel-cadmium (Ni-Cd) battery, which was invented in 1899 and commercialized in 1910. In this battery configuration, the cathode is nickel hydroxide mixed with graphite, the anode is cadmium hydroxide or cadmium oxide mixed with iron, and potassium hydroxide is used as electrolyte solution. This type of Ni-Cd batteries may evolve into gas generation from the decomposition of water, whereas this can be prevented by some special designs. The batteries, however, are too heavy to be applied in portable devices. With further improvements on the cell design, the sealed Ni-Cd batteries became available for portable devices, however, these Ni-Cd secondary batteries have a major drawback of “memory effect”. When the Ni-Cd batteries are not fully discharged before the initial charging process, the maximum cell voltage cannot be any longer obtained. The voltage at which the first discharge terminated will be maintained during charging.

The nickel-metal hydride (Ni-MH) battery is another alkaline secondary battery system that evolved from nickel-hydrogen battery, and was commercialized in 1989. In this battery configuration, hydrogen is acting as the anodic active material, while the cathode is conventional to the one used in Ni-Cd system, such as nickel oxide, the alkaline solution is acting as the electrolyte. In the Ni-MH battery, a metal alloy is placed at the anode side, which can reversibly absorb and desorb hydrogen during the charge-discharge process by forming a metal hydride. The development of the Ni-MH battery largely improved the energy density of the alkaline secondary battery, becoming almost twice that of a Ni-Cd battery. Because of the higher energy density, the Ni-HM batteries have been used in low-end electronics and portable electronic devices. However, this battery system is less durable than the Ni-Cd system, and also exhibits the memory effect.

The motivation of using lithium in the battery is the fact that Li is the lightest and most electropositive metallic element and can therefore provide a specific capacity almost ten times that of Pb in the lead-acid battery. In 1970’s, M. S. Whittingham at

Exxon built the first lithium secondary battery using Li-TiS_2 system.[7] Then Moli Energy commercialized lithium batteries with a $LiMoS_2$ cathode in 1980.[4] These batteries used a Li foil as the anode and various liquid organic electrolytes, which are not available presently due to their short life and safety issues: (i) high reactivity of the metallic Li anode with the electrolyte, and (ii) Li dendrite growth under a normal rate of charging (Figure 2.3a). The application of Li metal in rechargeable batteries was plagued by the safety problems arising from Li dendrite formation, so the use of Li intercalation materials for both electrodes attracted researchers' attention.

The idea of substituting metallic Li with a Li intercalation material (Figure 2.3b) was first introduced by Murphy et al. at Bell laboratories in late 1970s[8] and Lazzari et al. in 1980.[9] In the meantime, intercalation materials such as graphite used in organic solvents was discovered. Under such circumstances, research focus of cathode material shifted from transition metal disulphides to transition metal oxides because of their high insertion potential, which is necessary in order to compensate the potential difference arising from the replacement of Li metal. With the pioneering work of J. B. Goodenough who discovered an electrochemical cell with new fast ion conductors in early 1980's,[10] the lithium-ion battery was finally commercialized by Sony in 1991, with a configuration comprising $LiCoO_2$ as cathode, graphite as anode and liquid organic solution ($LiPF_6$ in 1:1 ratio ethylene carbonate and dimethyl carbonate (ED:DMC)) electrolyte. This battery could offer a potential of 4.2V after being fully charged, arising from the electrode potential difference between delithiated $Li_{1-x}CoO_2$ and lithiated graphite. The application of a graphite anode avoided the dendrite issue arising from Li metal anode, improving the safety of lithium-ion battery.

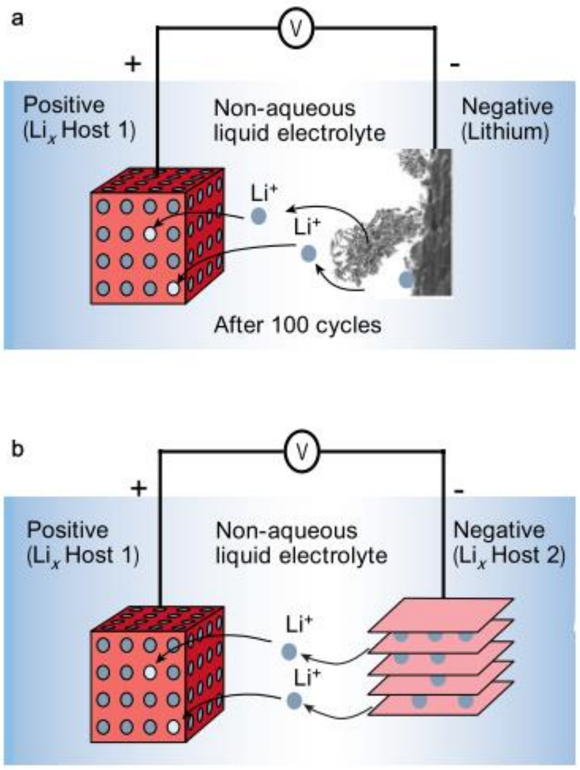

Figure 2.3 Schematic diagrams of (a) rechargeable lithium secondary battery using lithium metal as anode material, and (b) a lithium intercalation compound is used as anode material. From reference [11].

The performance of different secondary battery systems varies depending on the cell design, such as the choice of electrodes and electrolyte, as well as the specific conditions for the battery usage. Figure 2.4 illustrates the discharge behavior of different secondary batteries. The average voltage range of alkaline secondary battery systems is 1.7 V to 1.2 V, while the lead-acid battery has a cell voltage of about 2 V, higher than that of alkaline batteries. Among all these conventional secondary battery systems, the lithium-ion battery (graphite/Li_xCoO_2 system is used in this comparison) provides the highest discharge voltage, equivalent to about three Ni-Cd cells in parallel connection, which therefore enables a high power density. Meanwhile, high-voltage lithium-ion battery cathodes that enable an operation voltage up to ~4.7 V are being developed.[12]

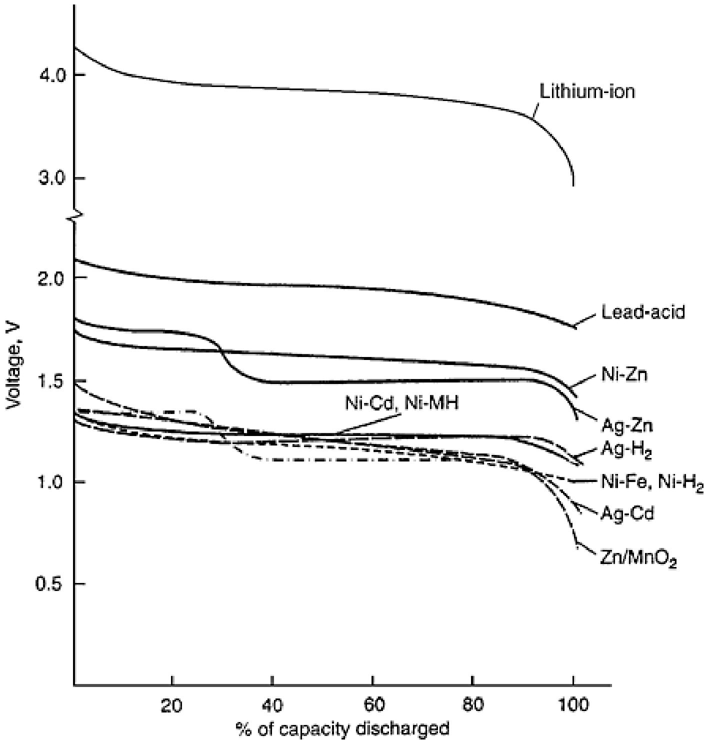

Figure 2.4 Discharge profiles of different secondary battery systems (at C/5 rate)†. From reference [6].

The amount of electrical energy that can be delivered from a battery is determined by the cell potential and capacity, which is directly associated with the cell chemistry. Among these secondary battery technologies, lithium secondary batteries show the highest energy density in both gravimetric and volumetric perspective, as illustrated in Figure 2.5.[11] Because of the superior performances, lithium secondary batteries have received most attention at both fundamental and commercial levels.

---

† The C-rate is defined as the discharge rate of a battery. 1C rate means the battery's capacity will be delivered in 1 hour, thus, C/N rate means the battery needs N hours to be fully discharged.

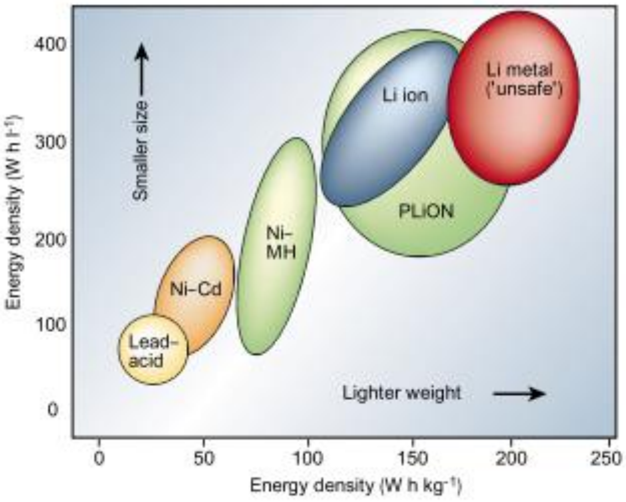

Figure 2.5 Comparison of volumetric and gravimetric energy density of different secondary battery systems. From Reference [11].

2.3 Overview of Lithium-Ion Batteries

To date, different combinations of electrodes and electrolyte for lithium-ion batteries have been developed and used in commercial applications. At the same time, new materials that enable higher operation voltage and higher capacity are being investigated and leading to promising electrode candidates for the next generation lithium-ion batteries.

2.3.1 Working Principle of Lithium-Ion Batteries

A lithium-ion battery can be schematically described in Figure 2.6.[13] Both electrodes are based on Li insertion materials which facilitate Li ions intercalation and deintercalation during electrochemical cycling. Graphite or other carbon based materials are commonly used in commercial lithium-ion batteries as the anode material which can provide a potential relative close to metallic Li. The cathode is a Li intercalation compound, usually a metal oxide with high standard potential. In this case, a layered transition metal oxide is shown in the schematic diagram in Figure 2.6. During cycling, the Li ions are reversibly intercalated and deintercalated from the two electrodes through an electrolyte which transports Li ions between the electrodes. The separator is a membrane that is made of polymers or ceramics, which physically prevents the direct contact between the positive and negative electrodes and allows ions, but not electrons, to pass through. During the charging process, the Li ions deintercalate from the cathode and are intercalated into the anode, while electrons travel through the external circuit from the cathode towards the anode. During the discharging process, the Li ions intercalate back to the cathode material accompanied with electrons transfer through the external circuit. The redox reaction of a layered cathode material is given as an example:

$$\mathrm{C} + yLi^{+} + ye^{-} \leftrightarrow Li_{y}C \qquad \text{(Anode)}$$

$$\mathrm{LiMn}O_{2} \leftrightarrow Li_{1-x}MO_{2} + xLi^{+} + xe^{-} \qquad \text{(Cathode)}$$

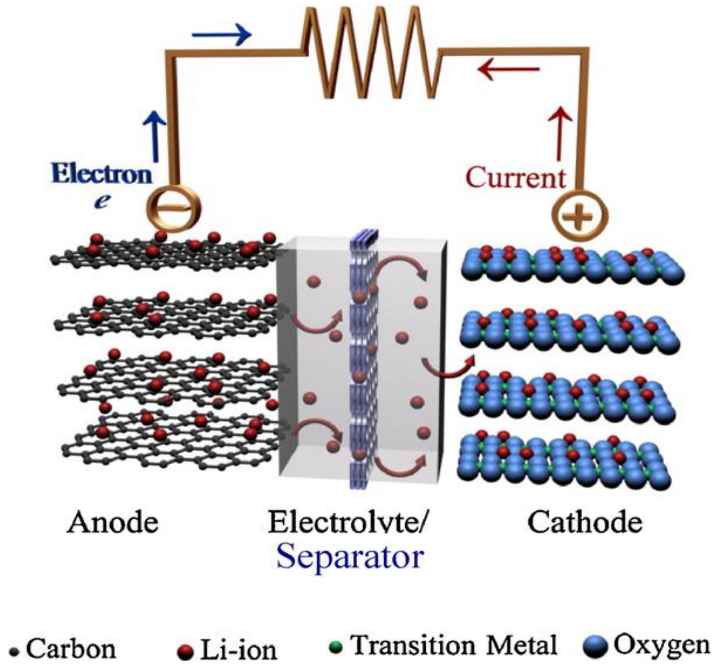

Figure 2.6 Schematic diagram showing the electrochemical process in a lithium-ion battery. From reference [13]. Graphite and a layered lithium transition metal oxide are shown as the electrode materials in the illustration.

The commercial lithium-ion batteries have been manufactured into different configurations in order to meet different demands, as show in Figure 2.7. These include: cylindrical cells, the most common form for consumer electronics (an example of cylindrical lithium-ion battery pack composed of multiple individual cells is shown in Figure 2.8); prismatic cells; single coin cells; and pouched cells. Amongst all these lithium-ion battery configurations, there are three major components that determine the performance of the battery: the positive and negative electrodes, and the electrolyte. The positive electrode, or cathode, provides the source of active lithium ions in the battery. The negative electrode, or anode, should have a low potential that is close to the electrochemical potential of lithium metal. The electrolyte should have high ionic conductivity, enabling a fast ion transfer between the two electrodes. A brief introduction of these three components is given in the following content.

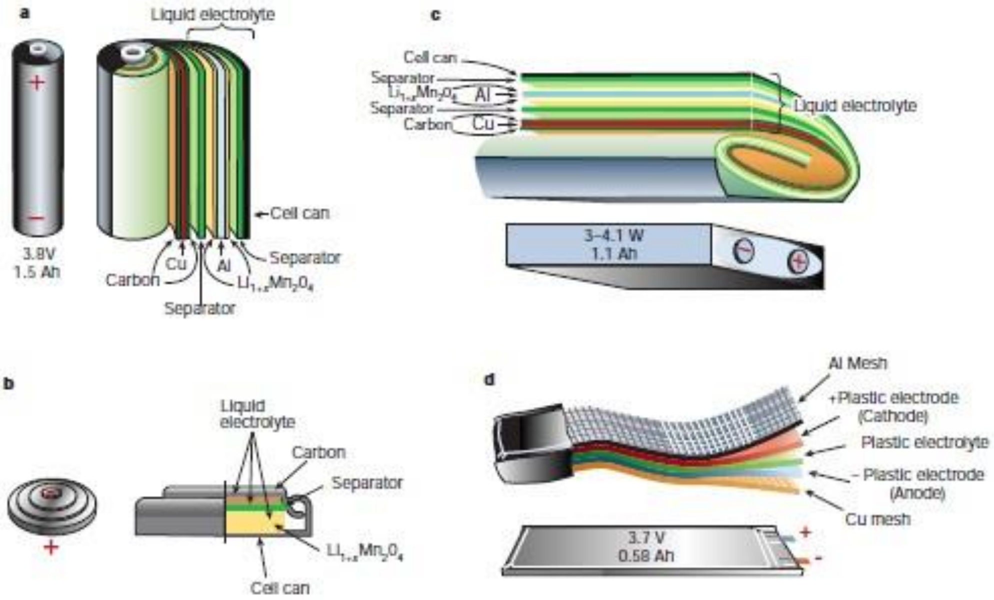

Figure 2.7 Schematic diagrams illustrate the shape and components of different lithium-ion battery configurations including: (a) cylindrical; (b) coin; (c) prismatic; (d) pouch. From reference [11].

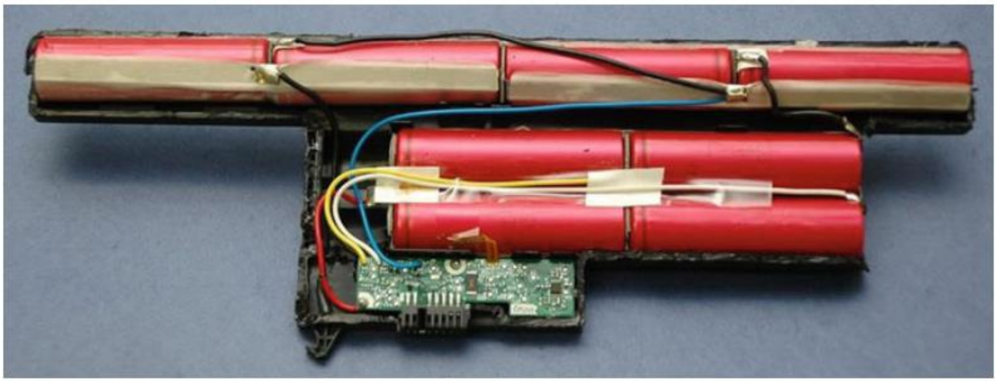

Figure 2.8 A photo of a lithium-ion battery pack that contains multiple single 18650 cylindrical cells (in red shrink-wrap). From Reference [14].

As described earlier, lithium metal was used as the anode material in the lithium secondary batteries in the early stages of their development. The dendrite formation on the lithium anode side, however proved to be problematic. Due to the safety concerns, alternative anode materials were being studied to replace lithium metal. The use of carbon-based materials enables a standard electrode potential close to that of lithium metal, thus resolving the safety issues arising from the lithium metal anode. The carbon-based anode materials experience no significant change in the crystallographic structure during lithiation and delithiation, therefore, ensure the reversible charge and discharge cycles. While graphite is the most commonly used anode material in the commercialized lithium-ion batteries, different structures of carbon-based materials are also under investigation in order to enhance the capacity of lithium-ion batteries. Furthermore, studies on non-carbon based materials such as alloys (Li-Al, Li-Si, etc.), metal oxides ($Li_4Ti_5O_{12}$, SiO_x, etc.) and metal-carbon composites (Si and Sn are some common elements in such composites) are being carried out for achieving higher specific capacity.[15]

In parallel to the anode development, the discovery of chalcogen group compounds as cathode materials laid the foundation for the development of lithium secondary battery technologies.[6,15] It has been demonstrated that chalcogen compounds, e.g. TiS_2, are able to participate in the intercalation reactions as their bulk structure maintains unchanged during lithium ion intercalation and deintercalation, therefore, enabling the repeated charge and discharge cycles for the battery. However, this type of cathode materials have disadvantages of high cost, difficult to synthesize, and low electrode potential, thus restricting their commercial application. With the commercialization of lithium-ion battery system using layered structure $LiCoO_2$ as cathode material, research on different types of oxide cathode materials evolved rapidly. More details of the recent development on cathode materials will be discussed in the following section.

In a lithium-ion battery system, the electrolyte has high ionic conductivity through which lithium ions can shuttle between the two electrodes. The electrolytes can be in the form of liquid, gel-polymer or solid-state. The liquid electrolytes is a solution with lithium salt dissolved in organic solvents (usually carbonates). Most of the commercial lithium-ion batteries now use this type of electrolyte. In addition, an ionic liquid electrolyte is also available for lithium-ion battery systems, this type of electrolytes are composed of lithium salts and molten salts with low melting point. Ionic liquid electrolytes are known of their safe operation because they do not include combustible organic solutions. Lithium-ion batteries using gel-polymer electrolyte are called lithium-ion polymer battery, in which a polymer matrix with a liquid electrolyte constitute the electrolyte component.[15] Currently, solid electrolytes attract lots of attention because of the increasing interest in the development of all-solid-state batteries, aiming to solve the instability and safety issues of the current liquid electrolyte systems. Compared to carbonate electrolytes, most of the solid electrolytes are stable under a wide voltage window (of above 5 V) and are noncombustible. This type of electrolytes, however, have not been used in real applications because of the low ionic conductivity and problems associated with interfacial compatibility between electrode and solid electrolyte.[16,17]

2.3.2 Application of Lithium-Ion Batteries

The rapid development of modern technologies has largely promoted the growth of the lithium-ion battery market. The global market for lithium-ion batteries is expected to reach $ 30 billion US dollars by 2020.[18] Currently, lithium-ion batteries have been successfully used in a variety of portable devices, such as mobile phones, tablets, laptop computers, entertainment devices, lighting, and medical applications because of their high energy density and high power density. With these superior performances, the application of lithium-ion batteries has expanded to the automotive industry. The demand for environmental friendly vehicles, including HEVs, plug-in hybrid electric vehicles (PHEVs) and battery electric vehicles (BEVs) has generated the need for high power lithium-ion batteries. Based on a 2016 report on automotive lithium-ion cell manufacturing, the annual growth rate of all the different types of EVs is expected to be 44% through 2020.[18] The demand of P/HEVs and EVs on lithium-ion battery will have a compounded annual growth rate of about 36% from 2015-2020, consisting of a need of 11 GWh in 2015 to 54 GWh in 2020, as shown in Figure 2.9. In addition to the application in automotive industry, the development of lithium-ion batteries also focuses on small electric appliances and portable electronic devices.

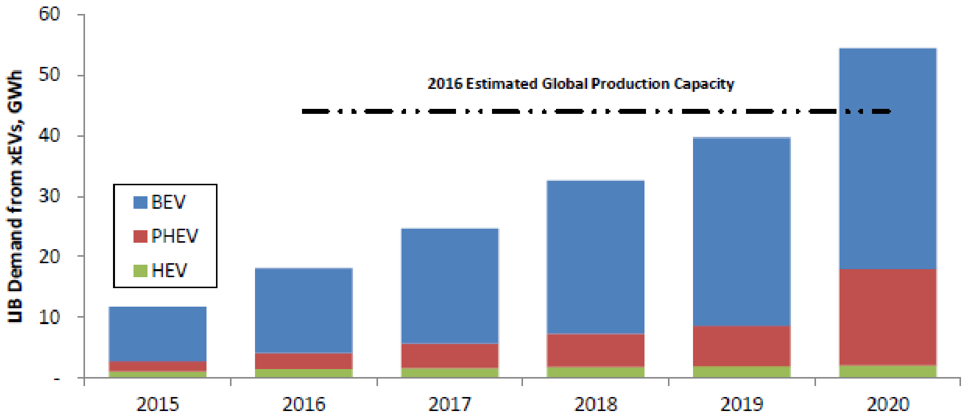

Figure 2.9 Estimated demand of lithium-ion batteries from automotive industry. From reference [18]

The safety of lithium-ion batteries for P/HEVs, EVs, and other applications is also an issue of great concern particularly in battery operations related to thermal abuse (e.g. external heating), mechanism abuse (e.g. mechanical damage), and electrical abuse (e.g. overcharge and short circuit). Considering the energy density of a lithium-ion battery is a few times that of a lead-acid battery, there is a risk of ignition of the cell component if this high energy is suddenly released following a short circuit.[14] Although the safety problems have not been fully eliminated from the lithium-ion battery applications, the development of advanced electrodes, electrolytes, separators, and controls are improving the safety level of the battery.

2.4 Cathode Materials for Lithium-Ion Batteries

As key components in lithium-ion batteries, different types of cathode materials have been developed ever since the development of lithium-ion batteries. The ideal cathode materials should display reversible behavior during Li intercalation-deintercalation and should have high electrical and ionic conductivities. The cathode materials should not undergo side reactions or irreversible phase transformation in order to maintain high cycle efficiency and battery capacity. Meanwhile, good electrochemical and thermal stability are expected for the cathode materials. Although the current cathode materials have not yet fully satisfied all these demand characteristics, the rapid development of novel materials has largely resulted in improved performance of the cathodes. Based on their crystallographic structure, the cathode materials fall into three main categories: layered type structure, spinel type structure, and olivine type structure.

The layered lithium transition metal oxides can be described by the general formula of $LiMO_2$ (M = Ni, Mn, Co, etc.) which crystallizes in a hexagonal layered structure. Oxygen layers are stacked in sequence of ABCABC… along the c-axis with Li and transition metal (TM) ions occupying the octahedral sites between oxygen atoms, as shown in Figure 2.10. Layered lithium transition metal oxides represent a major type of cathodes used in commercial market because of their high specific capacity and good stability. $LiCoO_2$, the most commonly used cathode material for commercial lithium-ion batteries, has α-$NaFeO_2$ type structure with $R\bar{3}m$ space group.[19,20] $LiCoO_2$ can provide a practical capacity of about 145 mAh/g, while overcharging (x>0.72) a $Li_{1-x}CoO_2$ cathode will lead to oxygen release, structure collapse and safety issues.[15] This cathode material is the first cathode material used in commercial cells, whereas it suffers drawbacks such as high cost and toxicity. As a result, layered $LiNiO_2$ and $LiMnO_2$ have been extensively studied as alternatives for $LiCoO_2$.[21–23]

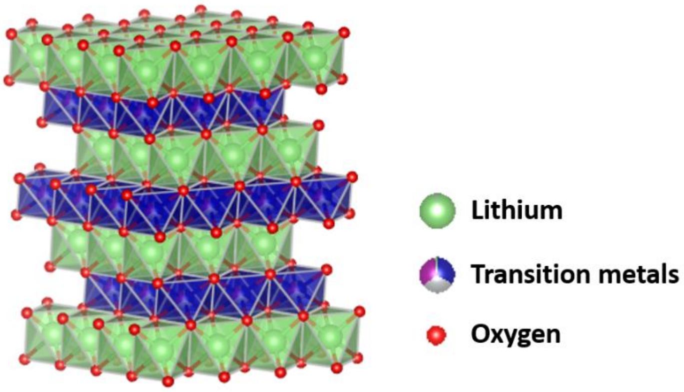

Figure 2.10 Atomic model for layered structure lithium transition metal oxide. The unit cell is outlined by the line frame.

$LiNiO_2$ has a high theoretical capacity, its actual capacity is also higher than $LiCoO_2$. However, it is difficult to synthesize stoichiometric $LiNiO_2$ due to the cation mixing arising from the similar atomic radii between Ni^{2+} and Li^+, thus resulting in nonstoichiometric $Li_{1-x}Ni_{1+x}O_2$.[24,25] The substitution of Li^+ by Ni^{2+} in nonstoichiometric $Li_{1-x}Ni_{1+x}O_2$ will hinder the lithium ion diffusion and lead to a reduced capacity.[15] This material is also metastable at elevated temperature and is accompanied by oxygen release, which leads to safety concerns.[26] $LiMnO_2$ cathode material is attractive from the economic and environmental point of view. Although the synthesis of layered $LiMnO_2$ is difficult since it is thermodynamically metastable, both the stoichiometric $LiMnO_2$ and nonstoichiometric $Li_xMn_yO_2$ have been successfully synthesized.[27] $LiMnO_2$ provides high initial capacity of 200 mAh/g when charging to 4.5 V. However, as the delithiated $Li_{1-x}MnO_2$ is unstable, this cathode material suffers irreversible phase transformation during charge-discharge. The deformation of the material due to Jahn-Teller distortion of Mn^{3+} and the rapid capacity decay arising from the detrimental phase transformation remain challenging.[28]

In light of these limitations, cathode materials with partial substitution of Co with Ni and/or Mn appear as alternative solutions to overcome these various disadvantages, and have been extensively studied. Stoichiometric $Li(Ni_xMn_yCo_{1-x-y})O_2$, described from here on as “NMC” materials, are effective cathodes for lithium-ion batteries that possess high reversible capacity and lower cost.[29–34] The $LiNi_{1/3}Mn_{1/3}Co_{1/3}O_2$ cathode material was first reported by Ohzuku's group and exhibits a higher capacity than the conventional $LiCoO_2$, it has small volume change upon cycling as well as good stability.[29,35] This cathode material has the same layered structure with $LiCoO_2$, the oxidation state of the three transition metals are Ni at 2+, Co at 3+, and Mn at 4+.[35,36] Although there are still debates on the role of TMs in the charge-discharge process, it is commonly recognized that Mn^{4+} is inactive in the redox reaction and contributes to the structural stability. More details regarding the charge compensation of layered $LiMO_2$ will be discussed in the next chapter.

The rapid development of automotive industry, such as P/HEVs and EVs, still requires improvements in energy density and power density of batteries. More recently, Li-rich cathode materials have attracted researchers' interest. These type of materials become one of the most promising cathode candidates which deliver high capacities of above 250 mAh/g when charged above 4.6V.[37–39] The Li-rich layered oxide compounds ($Li_{1+x}M_{1-x}O_2$) are derived from the conventional layered $LiMO_2$ oxides by partially substituting the transition metal (TM) cations with Li ions in the TM layers. The layered Li-rich oxides can be written in the form $x(Li_2MO_3)$-$(1-x)LiMO_2$, whereas the structure of the material, whether is a solid solution or a two-phase composite, remains ambiguous when the composition and synthesis method varies. Although a high capacity of above 300 mAh/g can be achieved during the initial charge, the Li-rich cathode has low first-cycle coulombic efficiency, there is a considerable irreversible capacity loss after the first discharge, as shown in Figure 2.11a. The rapid capacity decay and voltage fade under long-term cycling are also main limiting factors for the commercialization of this type of cathode materials (Figure 2.11b). The origins for the severe performance decay are therefore under extensive investigation,[40,41] as will be discussed in the next chapter.

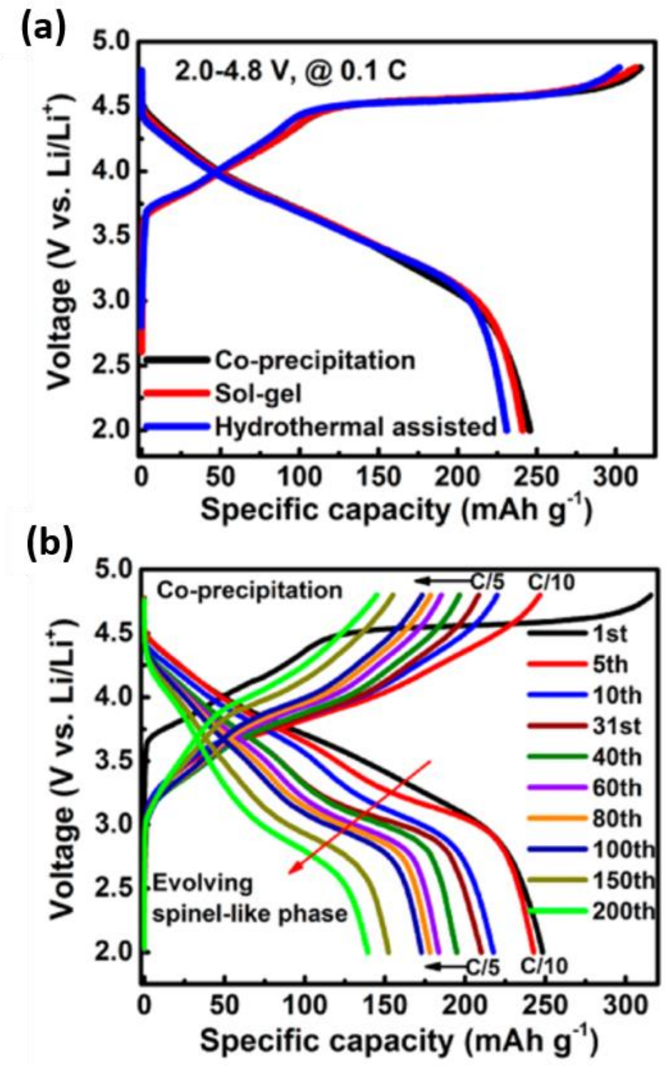

Figure 2.11 The cyclic performance of Li-rich cathodes. (a) Charge-discharge curve showing the irreversible capacity loss of Li-rich cathodes. (b) Cyclic performance showing the performance decay of Li-rich cathode during long-term cycling. From reference [42].

Another type of cathode material is the spinel structure LiM_2O_4 oxides, with $LiMn_2O_4$ as the representative material. $LiMn_2O_4$ has high theoretical energy density, is low cost and environmental friendly. [43] $LiMn_2O_4$ can provide an operating voltage of 4.1V, and its high potential analogue, $LiNi_{0.5}Mn_{1.5}O_4$, exhibits about 4.7V operation voltage.[12] The $LiMn_2O_4$ spinel crystals have the $Fd\bar{3}m$ symmetry, Li ions are occupying tetrahedral 8d sites surrounded by cubic-closed packed O atoms, Mn atoms reside in 16c octahedral sites (Figure 2.12). Unfortunately, this spinel cathode suffers severe capacity fade due to Jahn-Teller distortion of Mn^{3+}, loss of crystallinity, increasing oxygen deficiencies upon cycling, and more significantly, Mn dissolution into the electrolyte.[41,44,45] Extensive research has been devoted to improve the performance of spinel cathodes including substitutions of dopants into the spinel,[46,47] surface modifications,[48] and additives in electrolyte.[49] Furthermore, there have also been many studies focusing on the high voltage $LiNi_{0.5}Mn_{1.5}O_4$ (LNMO) spinel cathode material,[50,51] which becoming a promising cathode candidate for lithium-ion batteries.

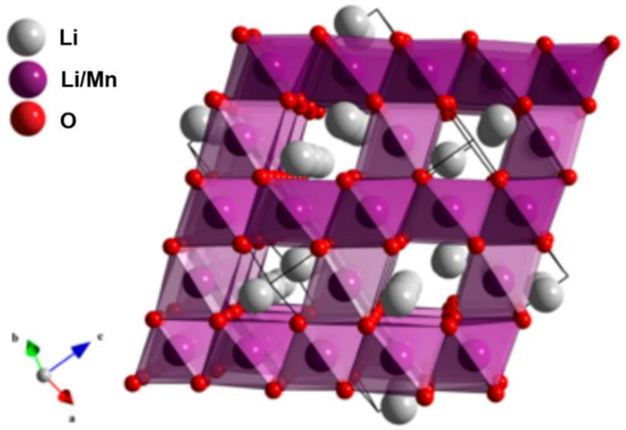

Figure 2.12 Polyhedral model of the spinel-type $LiMn_2O_4$ cathode material. From reference [46].

Olivine $LiFePO_4$ (Figure 2.13) was first reported by Pahdi et al. in 1997.[52] This cathode material satisfies many criteria for an ideal cathode material: it enables reversibly Li ion intercalation-deintercalation at 3.5V voltage, a high theoretical energy density of 170 mAh/g, good stability, and is compatible with most electrolyte systems. The abundance of the elements that composed in $LiFePO_4$ makes it a very environmental friendly cathode material. Unlike the former two types of cathode materials (layered $Li_{1+x}M_{1-x}O_2$ $(0 \leq x < 1)$ and spinel LiM_2O_4), this cathode material is limited by the poor electronic conductivity with about 1×10^{-9} S/cm at room temperature which limits the electrochemical performance of the cell since the electrons cannot be easily transported.[53] Many studies have focused on improving the electronic conductivity of $LiFePO_4$ including: carbon coating/mixing;[54–56] supervalent ion doping;[53,57] porous and nano-size structures.[58,59]

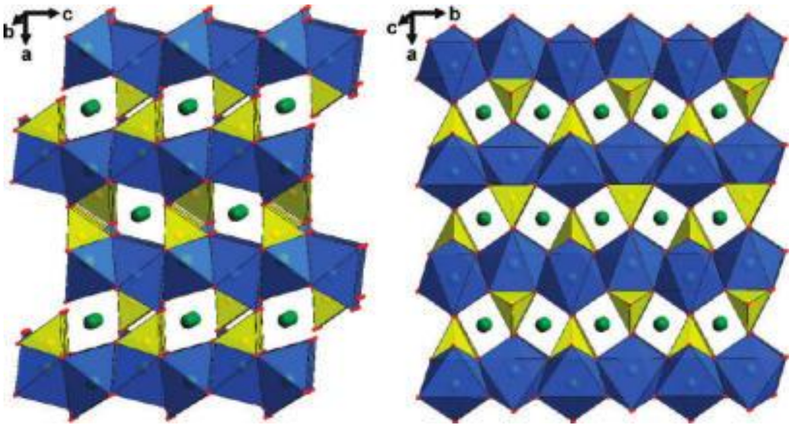

Figure 2.13 Polyhedral model of the structure of $LiFePO_4$ cathode material. From reference [49].

As a major component in lithium-ion battery, the cathode behavior highly influences the performance of the battery. Recently, high-voltage and high-capacity cathode materials that provide high-energy-density for the lithium-ion batteries have become the focus of cathode development. The effective design and modification of these promising cathode materials, however, rely on an in-depth understanding of the chemical and structural evolution of the material during electrochemical cycling. The work carried out in this thesis is focused on the study of layered structure cathodes. As will be discussed in the next chapter, there are still open questions on the charge compensation and degradation mechanisms of the layered cathode materials upon cycling. Therefore, a systematic study on the cycling-induced evolutions of layered cathode materials is hence necessary.

Chapter 3

Basics of Transmission Electron Microscopy

In order to synthesize and design electrode materials with improved cyclic performance, an in-depth understanding of the materials' behavior during electrochemical cycling is of great importance. The chemical and structural evolution of different lithium-ion battery cathode materials have been extensively studied using various techniques including X-ray absorption spectroscopy (XAS),[60–64] nuclear magnetic resonance (NMR),[65,66] X-ray diffraction (XRD),[67,68] neutron powder diffraction,[69,70] scanning electron microscopy (SEM),[71] scanning/transmission electron microscopy (S/TEM),[40,72,73] etc. Among all these techniques, TEM has shown its own potential because of its superior spatial resolution comparing to other techniques. Using aberration-corrected TEMs, one has the capability of obtaining structural information down to the atomic-level, and capturing the local chemical evolution of electrode materials during electrochemical cycling.

3.1 Overview of Transmission Electron Microscopy

A microscope can be simply described as a tool that can magnify objects that have small dimensions so that they become visible to the eye. The term “resolution” refers to the smallest distance between two points that can be resolved, in other words, the resolving power of the instruments used for magnifying. This resolution is directly related to the wavelength of the radiation used to image the object. Since the wavelength of electrons is substantially less than that of visible light, due to Louis de Broglie (1925), who theorized the wave-like characteristics of electron, an electron microscope can therefore provide a much higher spatial resolution than visible-light-microscope based on the classic Rayleigh criterion for the light-microscope.[74] From the criterion, the smallest resolvable distance (δ) is strongly dependent on the wavelength of the radiation, given approximately by

$$\delta = \frac{0.61\lambda}{\mu \sin\beta} \tag{3.1}$$

where λ is the radiation wavelength, β is the collection semi-angle, and μ is the refractive index of the medium of propagation. If taking $\mu\sin\beta$ as unity, then the resolution achieved with green light (a wavelength of about 550nm) will be about 300 nm. Now, if we considering the wavelength of an electron with an energy of 100 keV, according to the equation from Louis de Broglie, the wavelength (λ) of that electron is approximately (ignoring the relativistic effects):

$$\lambda = \frac{1.22}{E^{1/2}} \tag{3.2}$$

which is about 0.004 nm. Therefore, the spatial resolution of a microscope is pushed to smaller scale using an electron source, in theory, enabling the visualization of atoms in a material.

In practice, however, we cannot achieve the theoretical resolution based on these simplistic calculation since the electron lenses used in a TEM are not perfect. The resolution of a TEM is basically limited by the lens aberrations rather than the wavelength of the electron source. In a TEM, the electrons are focused using electromagnetic lenses. The spherical aberration in an electromagnetic lens occurs when the lens field behaves differently for off-axis rays than on-axis rays. Thus, a small point object will be imaged into a larger disk, which blurs the details in the imaging process. The chromatic aberration, on the other hand, occurs because the incident electrons are not monochromatic, the energy spread of the electron beam could be 0.3-3.0 eV depending on the electron sources used. Electrons with different energies will be focused differently, leading to a disk rather than the original point object imaged at the image plane. Nevertheless, the recent breakthroughs in the design of spherical and chromatic aberration correctors and monochromator have largely improved the resolution of modern TEMs.

When a high-energy primary electron beam interact with the specimen, there are a wide range of signals produced by this interaction, as shown in Figure 3.1. Although the signals may not be all detected by one TEM instrument (i.e. the TEM cannot collect all the signals if the specified detectors are not installed), many of them are commonly used in TEM analysis. The analytical TEM with X-ray energy-dispersive spectroscopy (EDS) and electron energy-loss spectroscopy (EELS) collect signals of characteristic X-rays and inelastically scattered primary electrons with certain energy-losses, providing valuable chemical information and many other details about the samples. The transmitted electrons or electrons used to form dark-field or bright-field images, diffraction patterns are at the basis of the operation and function of TEMs. Signals, such as backscattered electrons (scattered through angles > 90º), or secondary electrons (ejected from the sample) also contain useful information but are more generally used in a scanning electron microscope (SEM).

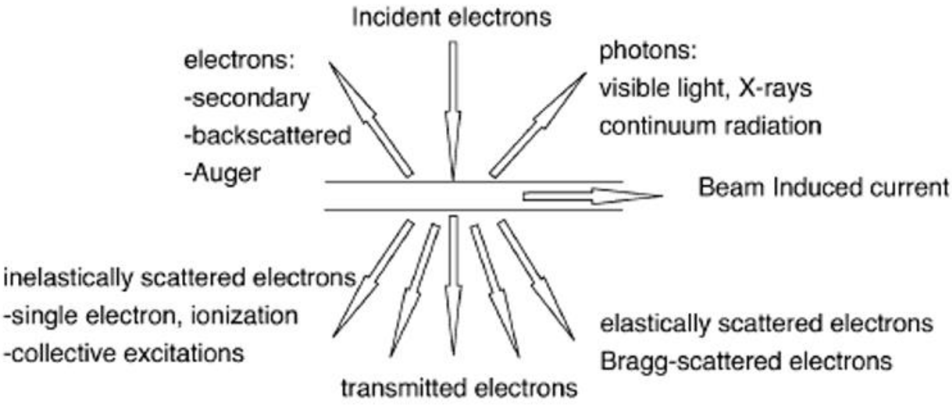

Figure 3.1 Signals generated from the interaction of incident electron beam with the specimen. From reference [75].

3.2 Introduction to Electron Scattering

Basically, when the high-energy incident electrons going through a thin specimen, some of them interact with the electrons or atomic-nuclei of the material through Coulomb (electrostatic) forces, being scattered with either no energy loss or some energy losses. The scattering events in a TEM is usually divided into two broad categories: elastic scattering and inelastic scattering. Elastic scattering involves almost no energy change in the incident electrons, which makes the main contribution to diffraction patterns and image contrast. Whereas from inelastic scattering, part of the kinetic energy of incident electrons is transferred to the electrons or atoms in the specimen. These energy-lost electrons are the main source for EELS.

3.2.1 Elastic scattering

The elastic scattering can be considered in two forms: one is scattering from single, isolated atoms, which helps in understanding the formation of Z-contrast images; the other is collective scattering from many atoms in the specimen, this form is at the basis of electron beam diffraction.[74] In the case of scattering with single atoms, the electrons can either interact with the electron cloud of an atom, or interact with the nucleus when the incident electrons penetrate the electron cloud. With respect to the electron-electron interactions, the electrons will be scattered at small angles, although in many cases, the incident electrons will suffer energy loss, resulting in an inelastic scattering events. When the incident electrons approach the positively charged nucleus, they are usually scattered through large angles because of the strong Coulomb attraction between electrons and nucleus, sometimes even leading to the generation of backscattered electrons. The differential cross section for the high angle electron-nucleus interaction was first discovered and derived by Ernest Rutherford and is therefore referred to as Rutherford differential cross section. The discovery of the Rutherford scattering is important for understanding the atomic number (Z) dependence of this high angle elastic scattering: the electrons that undergo Rutherford scattering provide information on atomic number contrast and are at the basis of Z-contrast images. More details on the Rutherford differential cross section will be discussed in section 3.4.

When referring to the phenomenon of collective scattering from many atoms, we need to think of the wave nature of the incident electron beam. In contrast to Rutherford scattering, the incident electrons are treated as plane waves and scattered by the atoms in the specimen, this being referred to as electron diffraction. The scattered electron wave front will be modified by the crystallographic arrangement of the specimen, leading to strong diffracted electron beams at small angles. These elastically scattered electrons at low angles are coherent, i.e. there are phase relationships between the scattered electrons, and the diffracted beams can be constructively interference with one another when they are in phase, or destructively interference when they are fully out of phase. The angles of the diffracted electron beams can be related to the spacing of the atomic planes in the specimen, which is described by Bragg’s law.

3.2.2 Inelastic scattering

Inelastic scattering refers to the interaction processes that leading to energy losses for the incident electrons. The signals arising from inelastic scattering process are invaluable for retrieving information about chemistry of the specimen. Some of these signals can be collected by detectors of an analytical transmission electron microscope (ATEM) and used for further analysis. Combined with the energy loss process of incident electrons, many different signals can be generated.[74,75]

When the incident electrons reach the specimen, they interact with the weakly bounded or free electrons in the conduction or valence band of the specimen and excite plasmons. The plasmons are quantized oscillations of electron gas and create localized regions with different electron density, which is most likely to occur in metals which possess large number of free electrons. The high-energy incident electrons can also penetrate the outer conduction and valence bands and interact with the tightly bound inner shell electrons. If a sufficient amount of energy is transferred from the incident electron to the inner shell electron, this electron will be ejected into the unfilled state above Fermi level, leaving a hole in the inner shell, and this atom becomes ionized. To ionize an atom, a minimum amount of energy needs to be transferred into the inner shell electron, defined as critical ionization energy (E_c). A higher E_c is required when the excited electrons are closer to the nucleus, i.e. the innermost K shell electrons will need a higher E_c than L or M shells, because the electrons are more tightly bound to the nucleus. After an atom is being ionized, it can go back to its ground state by filling the inner shell hole with an outer shell electron, and this process is accompanied with the emission of energy in the forms of X-rays or Auger electrons, as shown in Figure 3.2. The energy of this emission process is characteristic of the energy difference between the two shells, which is also dependent on the atomic number and coordination environment of the involved atom. Therefore, by collecting these secondary process signals, we are able to identify the chemical information of the specimen.

In addition to the emission of characteristic X-rays and Auger electrons, the incident beam of electrons may penetrate the inner shell electrons and interact with the atomic nucleus. In such case, the electron suffers a change in the momentum by the interaction with the nucleus and the lost energy of this electron may be in the form of bremsstrahlung X-rays. The bremsstrahlung X-ray signal contributes to the background of the characteristic X-ray spectrum, while this type of X-rays are not of much interest in analytical electron microscopy. Meanwhile, the inelastic scattering process also generates secondary electrons (SEs), which are electrons being ejected from the conduction or valence band of the specimen. Only the SEs from the specimen surface can escape from the material because of their low energy, and they are one of the major signals in SEM that provides useful topographic information of the specimen.

The inelastic scattering process generates a wealth of signals that carry a lot of information of the specimen, but we should be aware that the energy-loss electrons themselves are also of great importance, as they provide useful information about the chemistry and electronic structure of the specimen atoms. In order to analyze these primary energy-loss events, the energy distribution of the electron beam that interacted with the specimen can be obtained using EELS.

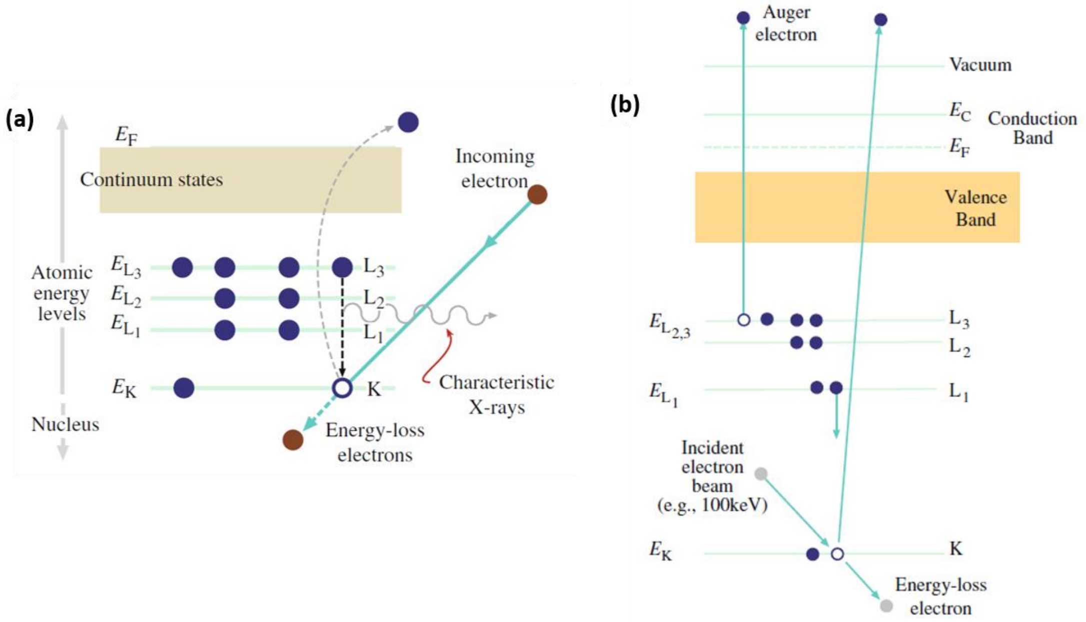

Figure 3.2 Schematic diagram showing the ionization process. (a) Generation of characteristic X-rays. (b) Generation of Auger electron. From reference [74].

3.3 Electron Energy-Loss Spectroscopy

EELS is a technique that detects the energy distribution of electrons that pass through the specimen and suffer either energy losses or no energy loss. The magnetic prism spectrometer and energy filter are used to produce an energy-loss spectrum and create energy filtered images or diffraction patterns (DPs) in a TEM.

An EELS spectrum contains electrons that have lost almost no energy, referred to as a zero-loss peak (ZLP). As shown in Figure 3.3, the ZLP primarily contains elastic scattered electrons and electrons have suffered small energy losses. Up to an energy loss of ~ 50 eV is the low-loss region, which contains electrons that have interacted with weakly bound electrons including inter/intraband transitions and plasmon interactions as introduced in section 3.2.2. Above that energy range is the high energy loss, or core-loss region, containing information arising from the ionization of an atom accompanied by the excitation of core-shell electrons. As described in section 3.2.2, to ionize an atom, a minimum energy of E_c is required. The cross-section of ionization event is highest when the energy loss E is at critical ionization energy E_c and gradually decreases with the increasing energy loss above E_c. The ionization edges can be used for identifying elemental information of the specimen, whereas, we can obtain way more than that from the core-loss spectrum.

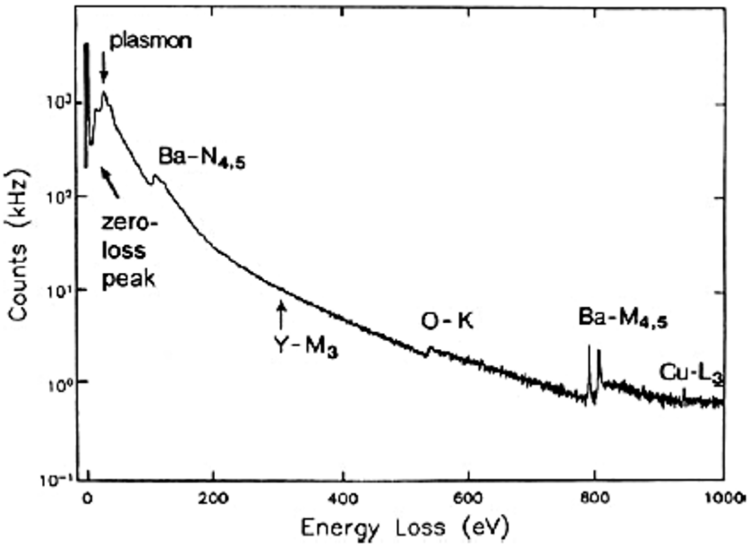

Figure 3.3 An example of EELS spectrum. From reference [76].

The core-loss spectrum can be described in two parts: energy loss near edge structure (ELNES) and extended energy-loss fine structure (EXELFS). The near edge fine structure oscillates within ~50 eV of the ionization energy E_c, which is valuable in obtaining chemical bonding information of atoms excited by the electron beam. For a basic understanding of the physics behind the ELNES, it is helpful to relate these features to the electronic density of states (DOS) and in particular the unfilled portion of the DOS in the material. When the core electrons are being ejected from their own core level states, they may not receive enough energy to escape to the vacuum level, but they transfer to the unfilled states above Fermi level. In such case, the energy being transferred from the incident electrons to the excited electrons are closely related to the unoccupied DOS. In other words, the ELNES can reflect the density of unfilled states of the target material. Because the DOS is very sensitive to the bonding character of the atoms, the shape of ELNES can be used to obtain information regarding the oxidation state and bonding environment of the ionized atoms.

In this thesis, the EELS measurements were carried out in STEM mode to ensure a spatially-resolved acquisition. The working principle of acquiring spectrum images (SIs) is shown in Figure 3.4.[75] A high energy incident electron beam is focused and scanned on a thin specimen pixel by pixel, the electrons that undergo high-angle elastic scattering are collected by a STEM detector (a detailed description of STEM detectors will be discussed in section 3.4) and form an image, while the energy-lost incident electrons that undergo inelastic scattering process are collected by the EELS spectrometer at the bottom of the microscope and recorded by a detector after the magnetic prism of the spectrometer. Thereby, a data cube with each pixel of the scanning area containing an EELS spectrum is obtained.

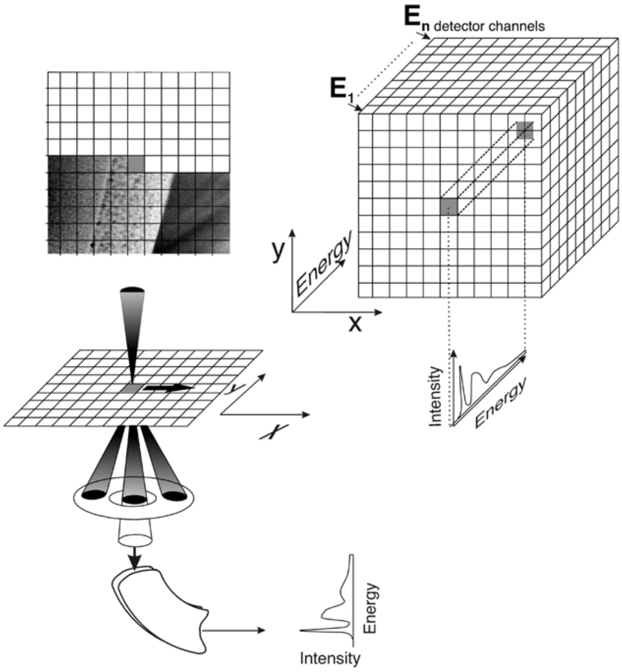

Figure 3.4 Schematic illustration of the STEM spectrum imaging acquisition. From reference [75].

The energy resolution of TEM is a key factor in determining how much information one can obtain from EELS. For vibrational modes of atoms, inter/intra-band excitation, and ELNES, an energy resolution of a few eVs is not sufficient. If the resolution of the spectrometer is not a limiting factor, the energy resolution is limited by energy spread of the incident electron beam. The normal thermionic sources can provide an energy resolution ~3 eV (W) and 1.5 eV (LaB_6), respectively, whereas a cold FEG or Schottky gun will provide a sub-eV resolution.[74] However, better solution can be achieved by further using a monochromator, which is usually a Wien filter with perpendicular electrostatic and magnetic fields that only allows the selected electrons to travel in a straight line down the TEM column.[76] An energy-selecting slit is placed in an image plane of its chromatic focus to further refine the energy spread. The monochromator is therefore used to produce an incident electron beam of small energy spread. An energy resolution below 0.1 eV can be achieved by using a monochromator and thus can be used to acquire remarkably fine details in the spectrum.

3.4 Scanning Transmission Electron Microscopy

In a TEM, the illumination system can be operated in two modes: parallel beam (TEM imaging) and convergent beam (STEM imaging). When operating in STEM mode, we can adjust the convergence angle of the beam by adjusting the condenser lenses and minimize the area of the specimen that is being illuminated. By controlling the scan coils of the pre-specimen area of the TEM, we are able to scan this focused beam (often called a "probe") on the specimen. Similar with TEM imaging, we can acquire both bright-field (BF) and annular dark-field (ADF) images in STEM mode with different detectors. As shown in the schematic of STEM imaging (figure 3.5), the different detectors are collecting electrons from different scattering angles.

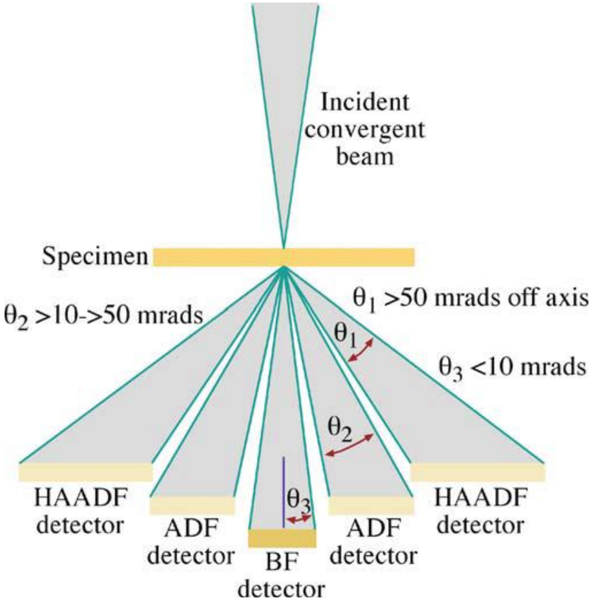

Figure 3.5 Schematic of the different detectors in a STEM imaging system, along with the range of electron scattering angles gathered by each detector. From reference [74].

The direct beam is collected by a BF detector centered on the optic axis. ADF detector is complementary to the BF detector, which is also centered on the optic axis but having a hole in the middle. When collecting the data with an ADF detector, we are forming an image using electrons that are being scattered by the nucleus (Rutherford scattering), which are incoherent (i.e. it does not depend on the defocus of the electron lens).[74] Before going into details of ADF imaging, the term "cross section" should be explained first. Cross section (σ) is used to describe the probability of any kind of interaction between the incident electron and specimen atom. The unit for cross section is 'barn', which equal to 10^{-28} m^2, or (10^{-5} nm^2). Note that the cross section is used to describe the probability of the occurrence of a scattering event, but not a physical area. The cross section will be different depending on the type of interactions and the energy of incident electron beam. The Rutherford differential cross section for high-angle scattered electrons by the nucleus can be expressed as

$$\sigma_R(\theta) = \frac{e^4 Z^2}{16(4\pi\epsilon_0 E_0)^2} \frac{d\Omega}{sin^4 \frac{\theta}{2}} \tag{3.4}$$

where E_0 (in keV) is the energy of the electrons, ϵ_0 is the dielectric constant and θ is the scattering angle. The relativistic and screening effects are ignored in this expression. For unscreened Rutherford scattering (ignoring the contributions from outer electrons), the cross section σ is proportional to Z^2 and the contrast of the images formed by Rutherford scattered electrons is termed as "Z-contrast" (heavier atoms appear bright in an image). This unscreened behavior is quite a good approximation for the high-angle scattered electrons while the screening only needs to be considered when the scattering angle is small (say < ~3°). We can further incorporate screening and relativity corrections into the expression and get the modified equation as

$$\sigma_R(\theta) = \frac{Z^2 \lambda_R^4}{64\pi^4 a_0^2} \frac{d\Omega}{\left[sin^2\left(\frac{\theta}{2}\right) + \frac{\theta_0^2}{4}\right]^2} \tag{3.5}$$

Here θ_0 is the screening parameter, the screening effect is prominent only when the incident electrons are far from the nucleus; a_0 is Bohr radius of the scattering atom when taking into consideration of the relativistic effects.

The influence of atomic number and scattering angle on the Rutherford cross section can easily be seen from the data shown in Figure 3.6. The cross section is getting smaller at higher scattering angles when approaching towards 180°. Also, with the increase of atomic number Z of the element from C to Au, the cross section increases by a factor of about 10^2. This significant change in the Rutherford cross section associated with atomic number variation contributes to the contrast of Z-contrast images.

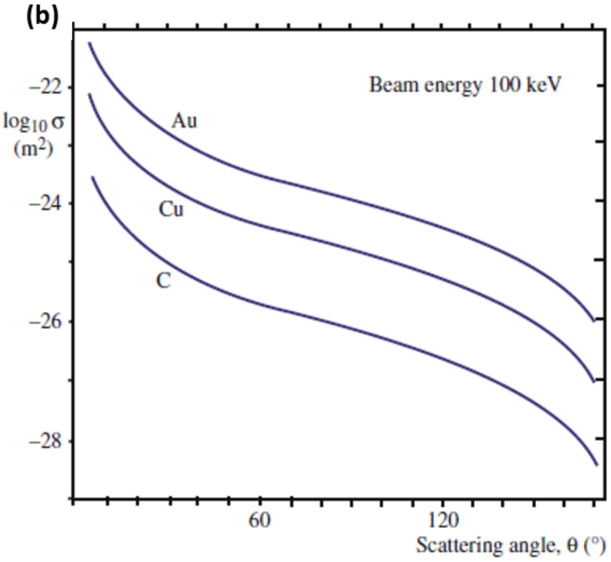

Figure 3.6 The variation of Rutherford cross section for electrons scattered at angles >θ from different elements at 100 keV. From reference [74].

In general, the Z-contrast images acquired in STEM mode are collected by a high-angle annular dark field detector (HAADF) detector, as shown in Figure 3.5. The HAADF detector only gathers the high angle forward scattered electrons with a scattering angle of >50 mrad (~3°), thus can further avoid the Bragg scattered electrons that may be collected by the normal ADF detector. Therefore, the HAADF image is also termed Z-contrast image in which the image contrast is due to the value of Z, not the orientation of the specimen. Therefore, the images are easier to interpret.

HAADF-STEM imaging has been widely used to characterize the crystallographic structure of various electrode materials for lithium-ion batteries. Using the instrument equipped with a spherical aberration corrector (Cs-corrector), which is the case for this thesis, one could obtain sub-Å resolution that enables the direct observation of the atomic arrangement of crystals. Unlike powder X-ray diffraction[67,68] or neutron powder diffraction[69,70] that only probe a macroscopic phase distribution and average crystallographic structure, the atomic arrangement and defects can be observed using this characterization technique. STEM imaging provides high spatial resolution that enables the examination of minor phase generations. As will be shown in the following discussions that some cycling-induced phase transformations only occur within the first few nanometers from the particle surface, and such surface evolutions are not within the detection limit of the bulk techniques.

3.5 Characterization of Layered Lithium-Ion Battery Cathodes

Compared to other characterization techniques, TEM shows its own advantage of superior spatial resolution capable of revealing the structure of studied material down to atomic-scale. In addition of acquiring the crystallographic information of the studied material, an analytical TEM equipped with X-ray energy dispersive spectrometer and electron energy-loss spectrometer provides chemistry information of the constituent atoms, such as chemical composition, bonding and valence state of the atoms. As introduced in the former section, with the application of monochromator, one could even achieve an energy resolution that is comparable to that of X-ray absorption spectroscopy (XAS). Therefore, TEM is a powerful tool that can be applied in the study of cathode materials in lithium-ion batteries.

3.5.1 Charge Compensation in Layered Structure Cathodes

In a lithium-ion battery, the capacity arises from the redox reactions accompanied with Li deintercalation-intercalation between the positive and negative electrodes. Therefore, to the extent that it influences the redox behavior, the chemical evolution of cathode materials during charge-discharge is critical for battery performance. During past years, there has been a growing interest on the layered lithium transition metal (TM) oxide cathode materials, as introduced in the former chapter. Previous studies showed that the Li ion deintercalation during charging process is accompanied with oxidation of TM ions in the layered lithium transition metal oxide cathodes,[18–25] whereas the redox mechanism of some TM species is not fully understood. There are still debates on the role of TMs in Li deintercalation-intercalation process, especially when more than one TMs are added into the material.[60–64]

Most of the previous studies on the charge compensation process of lithium-ion battery cathodes were carried out using XAS. With in-situ XAS experiment, Nakai et al.[60] investigated the charge transfer process in $Li_{1-x}Ni_{0.5}Co_{0.5}O_2$ (LNCO) with TM K-edge spectra during Li deintercalation. Their study suggested that the oxidation of Ni^{3+} to Ni^{4+} occurred in the first half part of the delithiation process, while Co continues to be oxidized slowly until x=0.8. Rosolen et al.[61–63] also observed the positive shift in the Ni K-edge due to Ni^{2+} oxidation, but they disagree with the Co^{3+} oxidation state change. In addition to the TM K-edges, they obtained Co and Ni $L_{2,3}$-edge XAS spectra for further analysis. The TM L_2- and L_3-edges arise from the electronic transition of $2p_{1/2}$ and $2p_{3/2}$ states (split by the spin-orbit coupling of the 2p state) to the unoccupied 3d states. This electric dipole-allowed 2p→3d transition gives rise to relative intense $L_{2,3}$-edge features, which are very sensitive to the oxidation state and spin state of TM ions. From the Co $L_{2,3}$-edge spectra acquired during Li deintercalation process (Figure 3.7), they claimed that the Co ions in LNCO were at trivalent Co^{3+} low-spin state and remain unaffected during Li deintercalation as evident by the consistent features of the Co $L_{2,3}$-edge spectra. They suggested that the Co K-edge shift is attributed to a change in the electrostatic potential of the surrounding ions. Meanwhile, different with the $Ni^{3+}\rightarrow Ni^{4+}$ oxidation that proposed by Nakai et al., they suggested that the charge compensation at Ni sites is made through $Ni^{2+}\rightarrow Ni^{3+}$.

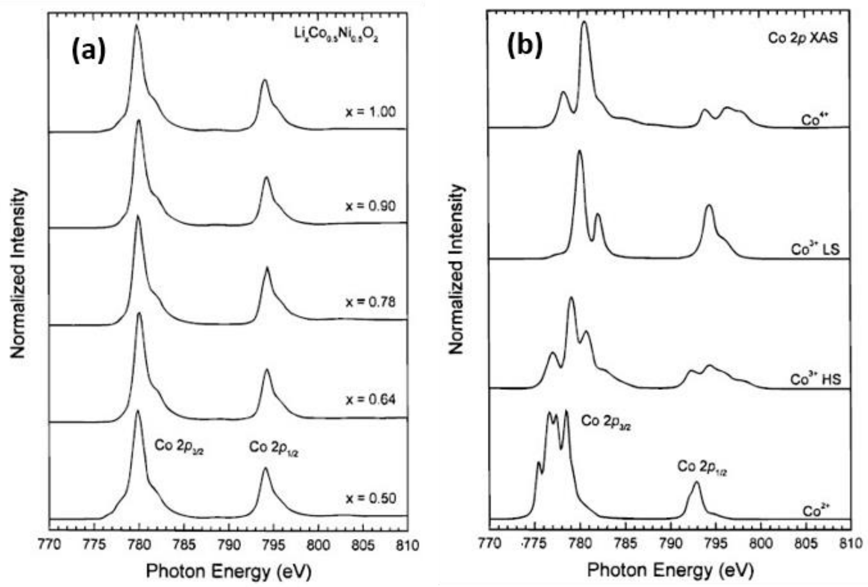

Figure 3.7 (a) Co $L_{2,3}$-edge XAS spectra of delithiated LNCO cathodes. (b) Calculated Co $L_{2,3}$-edge XAS spectra of Co^{2+}, high-spin Co^{3+}, low-spin Co^{3+}, and Co^{4+}. From reference[62].

Furthermore, studies on layered $LiNi_{0.5}Mn_{0.5}O_2$ (LNMO) show some differences between the surface and bulk.[64,77] The density function theory (DFT) calculations on the electronic structure of the LNMO indicates that Ni is the redox-active species and oxidized from Ni^{2+} to Ni^{4+} during Li deintercalation, while Mn^{4+} is stable during the process.[78] This calculation result is consistent with the in-situ XAS study, from which the Ni^{2+} oxidation was observed from Ni K-edge spectra and Mn^{4+} is electrochemically inactive.[77] The $Ni^{2+}\rightarrow Ni^{4+}$ oxidation was also observed by Yoon's group with soft XAS study,[64] whereas their results from the partial electron yield (PEY) mode and fluorescence yield (FY) mode presented different behaviors of Ni. While PEY is a surface sensitive mode (depth of more than 50 Å), the FY mode is more bulk sensitive which probes a depth of more than 1000 Å.[79,80] The Ni $L_{2,3}$-edge XAS spectra collected by the two modes presented different electronic structures between the surface and bulk, as shown in Figure 3.8. The charge compensation at the bulk region was mainly achieved by the oxidation of Ni^{2+} to Ni^{4+} as evident by the peak shift, whereas the oxidation state of Ni at the surface was almost unchanged at Ni^{2+}, as the Ni $L_{2,3}$-edge spectra acquired with PEY mode exhibits no obvious change.

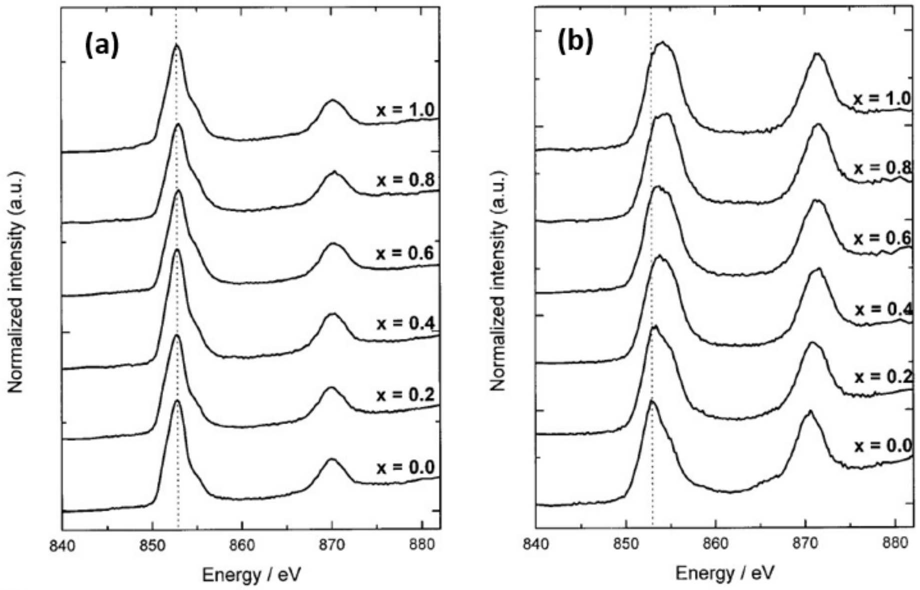

Figure 3.8 Normalized Ni $L_{2,3}$-edge XAS spectra of LNMO cathodes at different *x* values using the (a) PEY method and (b) FY method. From reference [64].

In the case of $LiNi_{1/3}Mn_{1/3}Co_{1/3}O_2$ (NMC), the charge compensation process is more complicated as three TMs co-exist in the cathode material. First principle calculations on NMC electrode during charge predicted that the reaction in the range of $0 \leq x \leq 1/3$, $1/3 \leq x \leq 2/3$, and $2/3 \leq x \leq 1$ in NMC electrode consists of Ni^{2+}/Ni^{3+}, Ni^{3+}/Ni^{4+}, and Co^{3+}/Co^{4+}, respectively.[35] It is shown from TM K-edge XAS experiment during the first-charge that $Ni^{2+} \rightarrow Ni^{4+}$ oxidation is related to the lower plateau around 3.75V while $Co^{3+} \rightarrow Co^{4+}$ occurred over the entire range of delithiation process.[81] By comparing TM K-edge and $L_{2,3}$-edges, Kim et al.[82] reported that the charge compensation was achieved through $Ni^{2+} \rightarrow Ni^{4+}$ and $Co^{3+} \rightarrow Co^{4+}$ by examining the bulk sensitive TM K-edge spectra, while the surface region investigated by the TM $L_{2,3}$-edge spectra only exhibited a change of $Ni^{2+} \rightarrow Ni^{3+}$. However, this work ignored the change in Mn $L_{2,3}$-edges (as shown in Figure 3.9), where the Mn L_3-edge showed a clear increase in the lower energy range. Instead, they concluded that both Co^{3+} and Mn^{4+} were unchanged at the surface.

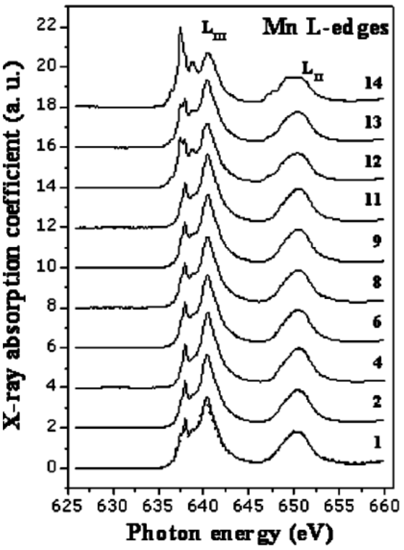

Figure 3.9 Mn $L_{2,3}$-edge XAS spectra of NMC cathode during Li deintercalation-intercalation. From reference [82].

Instead of using TM K-edge and $L_{2,3}$-edge to examine the difference between the bulk and the surface, Yoon et al.[83] also applied PEY and FY modes to investigate the charge compensation of TMs during the first-charge. From their results, the Ni $L_{2,3}$-edge XAS spectra collected in PEY and FY modes are slightly different. They concluded that the Ni^{2+} ions at the surface are less oxidized at surface than the bulk. Meanwhile, their result is in contrast with the Co oxidation reported in previous study. As can be seen from Figure 3.10, the Co $L_{2,3}$-edge spectra show no substantial changes during the delithiation process in both PEY and FY data, indicating Co remain unchanged in the Co^{3+} oxidation state. They suggested that it is not possible to determine the change of oxidation state solely by using K-edge features. The coordination environment, such as ligand-type, coordination number, bond length, etc. would also affect the edge features.

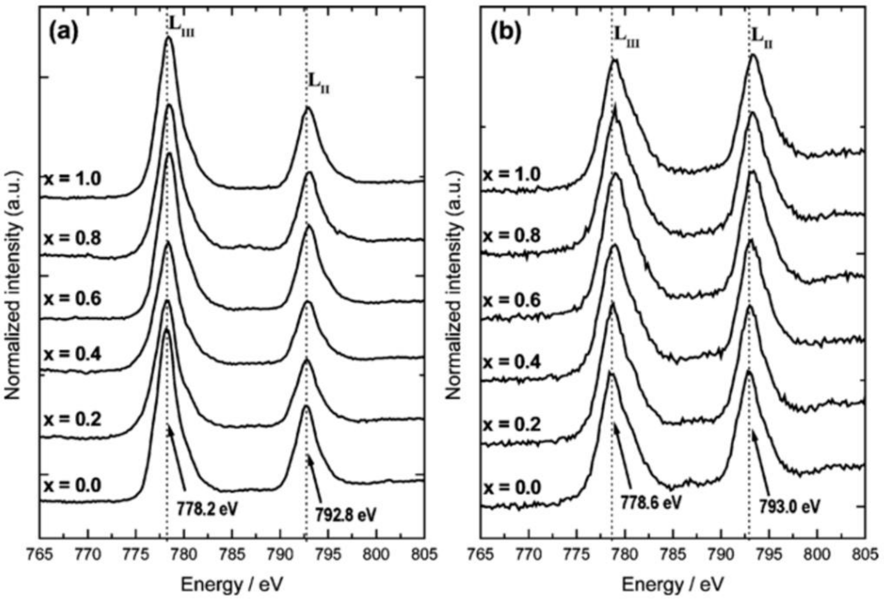

Figure 3.10 Co $L_{2,3}$-edge XAS spectra of $Li_{1-x}Co_{1/3}Ni_{1/3}Mn_{1/3}O_2$ cathode at different x values collected in (a) PEY mode and (b) FY mode. From reference [83].

EELS can also be applied to investigate the electronic structure of the TMs during lithiation-delithiation process in order to understand the charge compensation mechanism. Miao et al.[84] performed an EELS study on the local electronic structure change of NMC cathode material. They proposed in their work that the charge compensation is mainly achieved at oxygen 2p states, while no substantial change in the oxidation state of Co and Ni was observed during Li ions deintercalation process, since the TM $L_{2,3}$-edges remain unchanged (Figure 3.11). In their study, because of the poor energy resolution, it is difficult to infer the TM oxidation state from the TM $L_{2,3}$-edge near edge fine structures and the authors thus deduced the oxidation state only from the energy shift and comparisons with the electronic structure calculation. In addition, this study also ignored the surface and bulk differences. Therefore, an EELS study with improved energy and spatial resolution would provide much more valuable information (and less ambiguous) in studying the TM behavior during the charge transfer process.

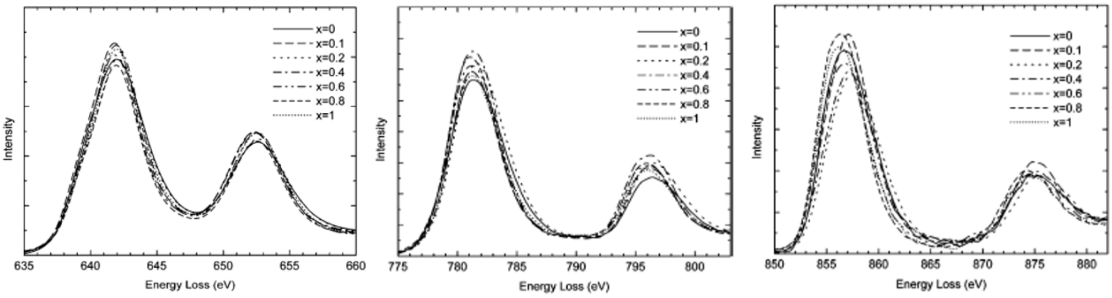

Figure 3.11 Mn, Co, and Ni $L_{2,3}$-edge EELS spectra (from left to right) of $Li_xNi_{1/3}Mn_{1/3}Co_{1/3}O_2$ at different x values. From reference[84].

From all the results above, the role of Ni and Co in the charge compensation process remains ambiguous. In addition, the inhomogeneity of the TM oxidation state discovered from the particle surface to the bulk has not yet been fully understood.[21–24] It is clear that there are knowledge gaps with respect to the charge compensation processes and local changes in the TM oxidation states, thus, detailed studies on the role of TMs during delithiation and lithiation process are needed. So far, most of the studies discussed above were carried out using XAS because of its superior energy resolution, whereas this technique lacks sufficient spatial resolution to provide information at the nanometer length scale for understanding localized phenomena. Considering the complexity of the surface chemistry induced by the inevitable electrode-electrolyte interface reactions, a detailed study on the chemical evolution of the cathode material using spatially-resolved characterization technique, such as STEM-EELS, is hence necessary.

Another class of materials of interest are the layered Li-rich oxides which possess a much higher capacity than the regular layered oxides discussed above.[37,85,86] In contrast to the regular layered oxide cathode materials, it has been reported that the delithiation process for these Li-rich oxides includes two steps, as shown in Figure 3.12.[69] During the initial charging region up to ~4.5 V, the capacity originates from the TM oxidation. For the high voltage plateau above 4.5 V, the anomalous high capacity during first charge arises from the excess Li^+ removal compensated by oxygen loss.[69,86–88]

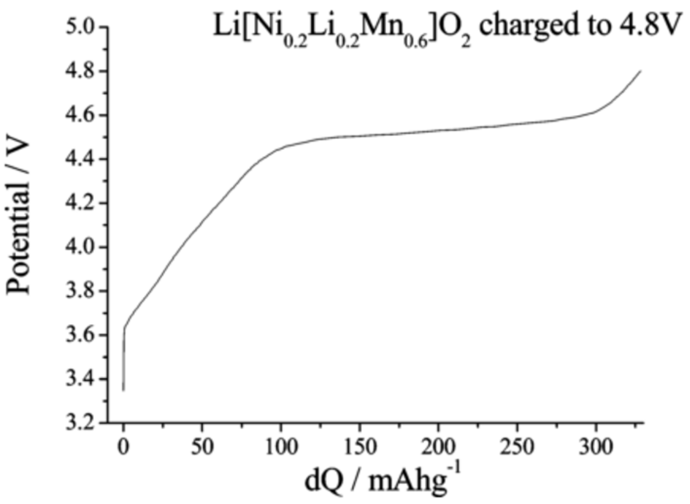

Figure 3.12 Variation of potential (vs Li^+/Li) with state of charge of $Li_{1.2}Ni_{0.2}Mn_{0.6}O_2$ cathode at 10 mA/g rate. From reference [69]

Armstrong et al. have demonstrated the direct oxygen evolution associated with the 4.5V plateau by in situ differential electrochemical mass spectroscopy (DEMS).[69] Jiang et al. have revealed the Li^+ removal in $Li(Li_{1/9}Ni_{1/3}Mn_{5/9})O_2$ cathode from both Li layer and TM layer using solid-state NMR at different states of charge and discharge.[65] The in-situ XAS measurements indicated that partial oxidation of O^{2-} may attributed to the reversible capacity in the Li-rich cathode material $Li(Ni_{0.17}Li_{0.2}Co_{0.07}Mn_{0.56})O_2$.[89] They suggested, from the TM K-edge spectra, that the contribution from Ni^{2+} and Co^{3+} are less than two electrons and one electron, respectively. The oxygen redox participation in Li-rich cathode material was also proposed by Delmas et al..[88] Using ex-situ XRD, they observed a mixture of two phases formed upon cycling. Although their experiment only shows structural data from XRD, they still proposed a mechanism from their observation: oxygen loss occurred at the surface with densification of the host structure; oxygen oxidation happened in the bulk without major structure modification.

A subsequent question is related to the nature of the oxygen redox reaction occurred during lithium deintercalation and intercalation. One suggested form of oxygen oxidation during charge is the formation of peroxo-like species (O_2^{n-}). Using X-ray photoelectron spectroscopy (XPS) and TEM, Tarascon et al.[90] reported the formation of O-O peroxo-like dimers in Li_2IrO_3 during charging. In this work, they observed the O 1s peak in XPS spectra that represents the O_2^{n-} species during cycling. Meanwhile, they revealed the lattice distortion with the formation of shortened (1.56 Å) and lengthened (1.83 Å) projected O-O separations in delithiated $Li_{0.5}IrO_3$, indicating the formation of O_2^{n-} peroxo-like species, as shown in Figure 3.13.

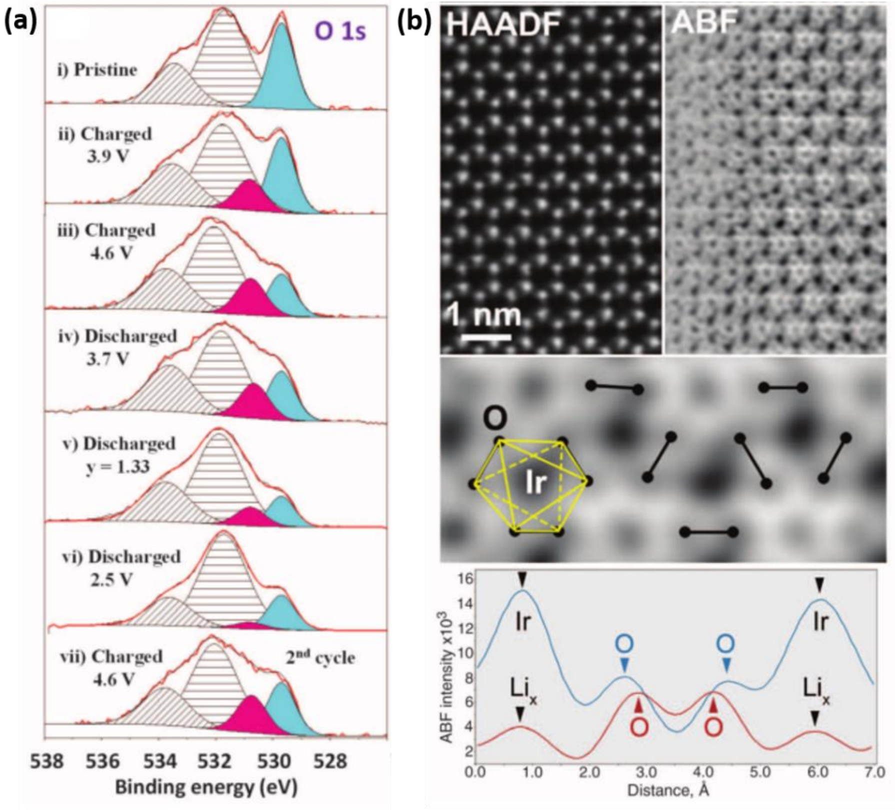

Figure 3.13 (a) Oxygen 1s core XPS peaks of Li_2IrO_3 during cycling. The O^{2-} (blue) and O_2^{n-} (red) peaks are attributed to the cathode material, whereas the two gray shaded peaks are attributed to the surface species and electrolyte decomposition products. (b) HAADF- and ABF-STEM images of the charged $Li_{0.5}IrO_3$ cathode, demonstrating the differences in the projected distance of O-O pairs. From reference[90].

Recently, a detailed work on the charge compensation process of Li-rich cathode was carried out by Bruce et al.,[91] who reported the O evolution of Li-rich oxide during charging. In addition to O release, they proposed that the anionic redox reaction is made through the formation of localized electron holes on oxygen atoms coordinated by Mn^{4+} and Li^+ ions, but not true O_2^{2-} species, for the charge compensation of Li^+ removal. The influence of local Li-excess environment around O atoms on the redox activity of oxygen in the layered Li-rich oxides was further investigated by Ceder et al..[92] They suggested that the Li-O-Li configurations create oxygen states at a higher energy than the hybridized O bonding states (as shown in Figure 3.14), making them more easily oxidized. The oxidation of the oxygen in Li-rich oxides is mainly achieved through the labile electrons in the Li-O-Li states.

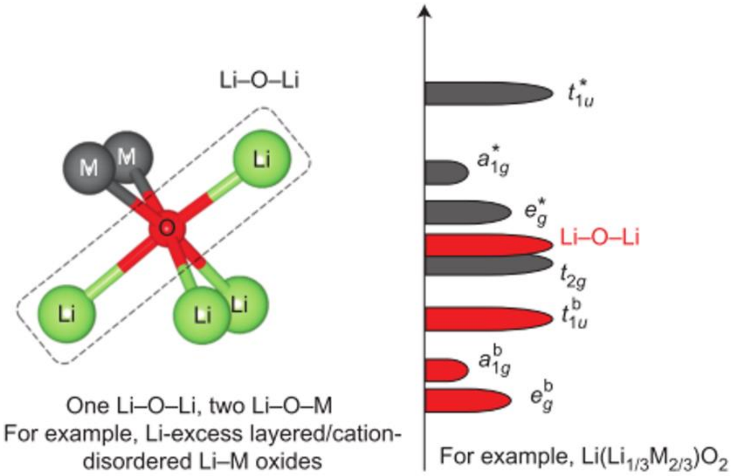

Figure 3.14 Schematic of the band structure of layered Li-rich oxides demonstrating the Li-O-Li states. Atomic model (on the left) shows the local environment around oxygen with one Li-O-Li and two Li-O-M configurations. From reference [92].

Through the continuous efforts of researchers, the origin of the anomalous high capacity of Li-rich cathodes is gradually being understood, although more work is still needed to completely uncover its chemistry. The discovery of anionic oxygen redox reaction in the charge compensation process of layered Li-rich cathodes overcomes the limit of TM-determined theoretical capacity. The oxygen redox mechanism for different compositional Li-rich materials, however, have not yet been fully understood. Detailed investigations on the electronic structure of TM and O during the first irreversible cycle and the subsequent cycles are still of importance for validating the calculations and to better understand the cycling behavior of these high-energy-density cathodes.

3.5.2 Structural Evolution of Layered Structure Cathodes

Sufficient energy density of lithium-ion batteries after extended cycles has not yet been achieved due to capacity fade. This effect is attributed to multiple possible factors, including electrolyte decomposition and SEI formation,[93–104] chemical and structural changes of electrode materials. [72,105–107] The design of lithium-ion batteries that enable improved cycling performance thus relies on an in-depth understanding of the chemical evolution and structural transformation of the electrode materials upon cycling. It has been proposed that the layered lithium transition metal oxide cathodes suffer irreversible phase transformations that contribute to battery degradation. Possible transformation include a transition from layered structure into spinel structure ($Fd\bar{3}m$), [108,109] and/or to rock-salt structure ($Fm\bar{3}m$),[110–115] or from the newly formed spinel phase to other stable phases.[116]

Ikuhara et al.[73] investigated the microstructure of the $LiNi_{0.8}Co_{0.15}Al_{0.05}O_2$ (NCA) cathode material before and after first cycle using STEM and EELS. Their results showed the formation of very thin layers at grain boundaries that contain TM ions (particular Ni) on Li sites. After the first cycle, the layered $R\bar{3}m$ structure at the grain interior gradually changed to a partially ordered structure and then to a disordered rock-salt structure at the grain boundaries. The corresponding EELS data also showed that the Co^{3+} and Ni^{3+} have been reduced to a lower valence at the rock-salt surface layer. Kang et al.[112] observed an irreversible phase transformation at the cathode surface of $LiNi_{0.5}Co_{0.2}Mn_{0.3}O_2$ from rhombohedral structure into a mixture of spinel and rock-salt phases. However, the acquired HRTEM images do not clearly show the atomic-ordering of the surface “cubic region”, as shown in Figure 3.15. Meanwhile, the atomic-ordering displayed from the labelled “spinel region” is not unique to the spinel phase. Therefore, improved spatial resolution measurements and more orientations are necessary for the investigation of the structural evolution.

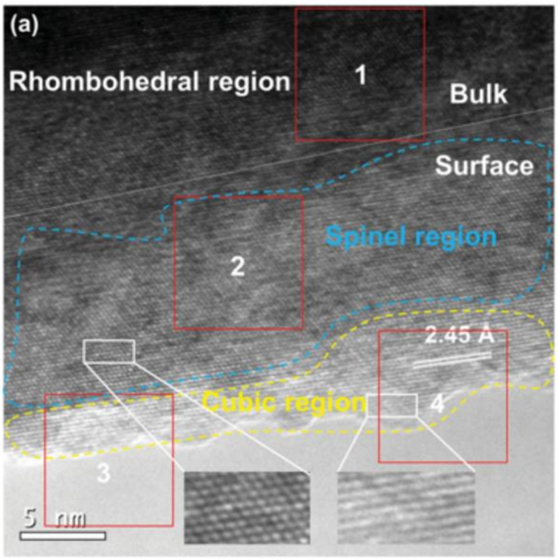

Figure 3.15 HRTEM image of the $LiNi_{0.5}Co_{0.2}Mn_{0.3}O_2$ cathode after 50 cycles under 3.0-4.8 cycling condition. From reference [112].

Abraham et al.[111] reported in their work that a NiO-type rock-salt surface layer exists on the $LiNi_{0.8}Co_{0.2}O_2$ particles from HRTEM imaging and convergent beam electron diffraction (CBED) pattern, while the thickening of this layer during cycling could significantly hinder the Li ion transfer. Combining XAS and EELS data, they suggested that both Co and Ni are in trivalent state in the bulk region but in lower valence at the particle surface, and this phenomenon is more obvious for the aged cell. A relative Ni and Co enrichment was also found on cathode surface. A similar situation was observed on $LiNi_{0.4}Mn_{0.4}Co_{0.18}Ti_{0.02}O_2$ cathode material after cycling.[40] The layered structure undergoes a phase transformation from a layered structure to a rock-salt structure and leading to the formation of a surface reduction layer (SRL) with all the TM ions in divalent states, as shown in Figure 3.16.

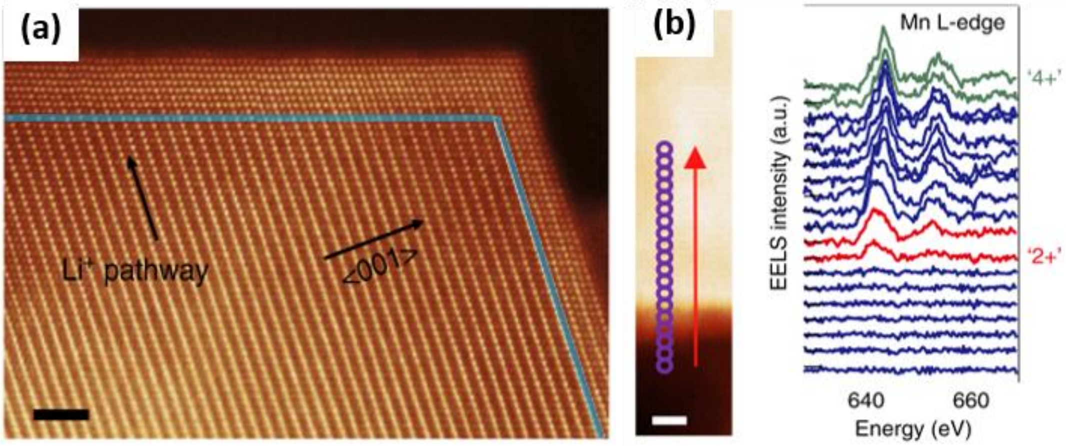

Figure 3.16 (a) Atomic-resolution STEM images of $LiNi_{0.4}Mn_{0.4}Co_{0.18}Ti_{0.02}O_2$ after 1 cycle. (b) EELS spectra of Mn $L_{2,3}$-edges along (001) direction is shown on the right. From reference [40].

The surface structural changes and thermal stability of NCA and NMC cathodes were also reported by Yang et al..[108] From their study, a rock-salt surface and a spinel near-surface region were discovered from the overcharged NCA cathode while these surface phases propagate towards the core during heating. In contrast with Kang et al., they proposed the phase transformation on NMC surfaces is from a layered structure into a LiM_2O_4-type spinel structure and then a further transformation into mixed Co_3O_4-type and LiM_2O_4-type spinel phases after heating up to 300ºC. More detailed investigations on thermal induced evolution of NCA cathode and NMC cathodes with different Ni content (0.4, 0.6, 0.8) were performed using TEM and EELS.[114,115] As a result of thermal decomposition, the electronic structure of the charged (delithiated) cathode materials changes at their surfaces, as shown from the EELS spectra in Figure 3.17. The authors pointed out that the changes in electronic structure were associated with the reduction of the TM ions, oxygen gas release and phase transformation during heating. The results suggest that although the high Ni-content cathode exhibits high capacity, it shows the worst thermal stability than the other two compositions, which may arising from the large amount of unstable Ni^{4+} at the charged state. Based on previous studies, it is clear that the chemical and structural evolution of layered lithium transition metal oxide cathodes with different compositions and under different cycling conditions remain controversial. The elucidation of the cycling-induced changes of layered cathode materials is therefore important and would provide a more complete understanding of the cathode degradation mechanisms.

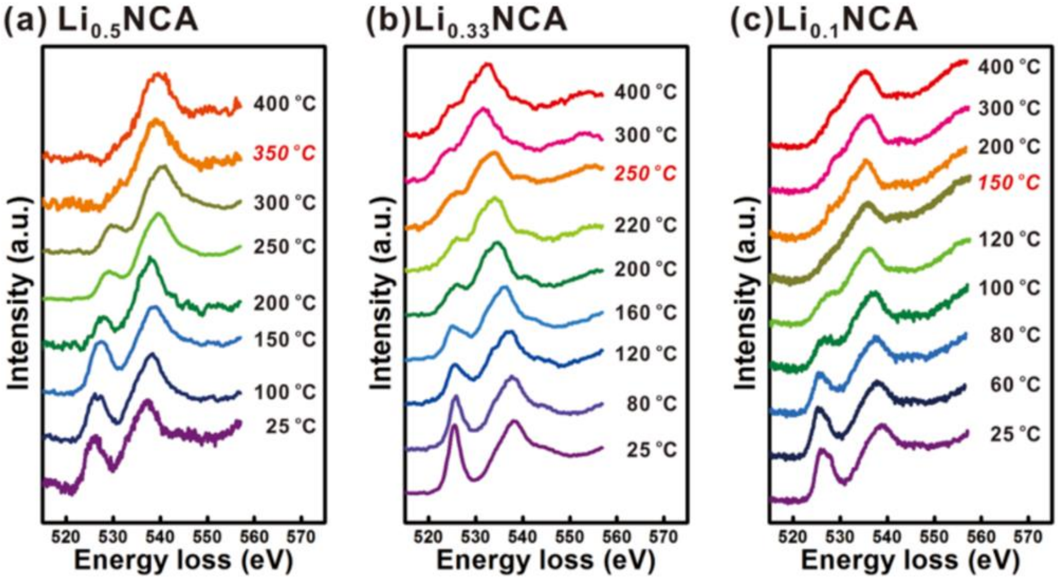

Figure 3.17 Oxygen K-edge EELS spectra from $Li_xNi_{0.8}Co_{0.15}Al_{0.05}O_2$ (x=0.5, 0.33, 0.1) at different temperatures. From reference [114].

As discussed in Chapter 2, Li-rich layered oxides have become some of the most promising cathode candidates for the next generation lithium-ion batteries due to their exceptional high capacity.[117–121] The local ordering of excess Li with TM atoms has been confirmed by XRD and neutron diffraction (ND) from the observation of superstructure diffraction peaks at lower angles, indicating the presence of Li_2MnO_3-type monoclinic ordering.[122–124] So far, the debate on the structure of pristine Li-rich layered oxides is mainly focused on whether the material is a two-phase composite or a single-phase solid solution. Thackeray et al.,[125–127] have proposed that these Li-rich oxides are two-component composites that are composed of x(Li_2MnO_3) monoclinic phase and (1-x)$LiMO_2$ trigonal phase, while similar results have also been reported by other research groups.[122,128–132] Using atomic-resolved HAADF-STEM imaging, Yang et al.[128] demonstrated that the pristine $Li_{1.2}Ni_{0.15}Co_{0.1}Mn_{0.55}O_2$ material contains layered components of both the monoclinic Li_2MnO_3 phase and the rhombohedral $LiMO_2$ phase. As shown in Figure 3.18, they described the continuous dots contrast observed from the HAADF image (area I and III) to be $LiMO_2$ component, and the discontinuous dots contrast areas (II and IV) to be Li_2MnO_3-like component.

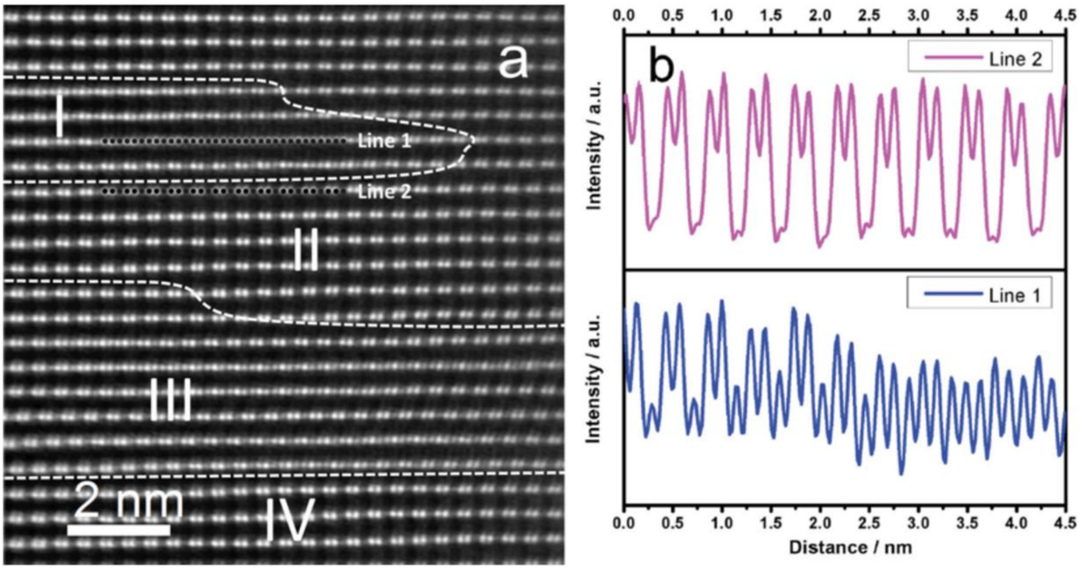

Figure 3.18 Characterization of pristine $Li_{1.2}Ni_{0.15}Co_{0.1}Mn_{0.55}O_2$ cathode material. (a) HAADF-STEM image of pristine $Li_{1.2}Ni_{0.15}Co_{0.1}Mn_{0.55}O_2$. (b) Intensity profiles of the atomic planes labelled in (a).From reference [128].

Meanwhile, Yu et al.[129] reported the coexistence of rhombohedral $LiMO_2$ and monoclinic Li_2MnO_3-like structures in lithium-rich $Li_{1.2}Mn_{0.567}Ni_{0.166}Co_{0.067}O_2$ cathode material by combining selected area diffraction (SAED), annular bright-field (ABF) and HAADF-STEM imaging, as shown in Figure 3.19. However, no chemical data of the two claimed phases was presented in this work.

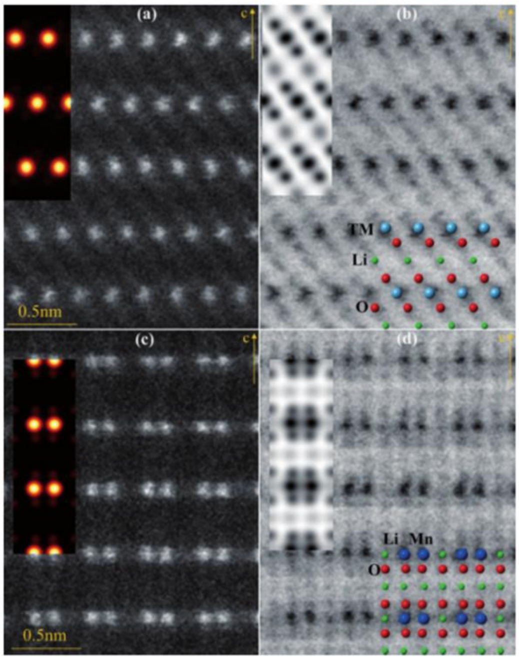

Figure 3.19 HAADF- and ABF-STEM images of different regions in $Li_{1.2}Mn_{0.567}Ni_{0.166}Co_{0.067}O_2$. (a, b) Images taken from $LiMO_2$ phase along [110] direction. (c, d) Images taken from Li_2MnO_3-like monoclinic phase along [100] direction. From reference [129].

In contrast, using XRD, STEM, and electron diffraction (ED), Jarvis et al. proposed that the structure of Li-rich layered oxide is a solid solution in *C2/m* monoclinic symmetry with planar defects.[133,134] Shukla et al. also reported the Li-rich cathode materials with different morphologies are made up of monoclinic single phase.[135] They concluded that the bulk material contains domains with different variants of the *C2/m* monoclinic phase, i.e. [100], [110] and [1-10], as shown in Figure 3.20. It is also pointed out that some viewing orientations, such as [010] of monoclinic phase is indistinguishable from the [010] or [110] direction of trigonal $R\bar{3}m$ phase. This information indicates that one cannot confirm the structure of Li-rich oxides, i.e. monoclinic or trigonal, only by judging the atomic-arrangement of the images when viewing along a limited number of directions. Due to the complexity of these Li-rich compounds, the structure of pristine Li-rich cathode materials thus remains elusive and needs further clarification.

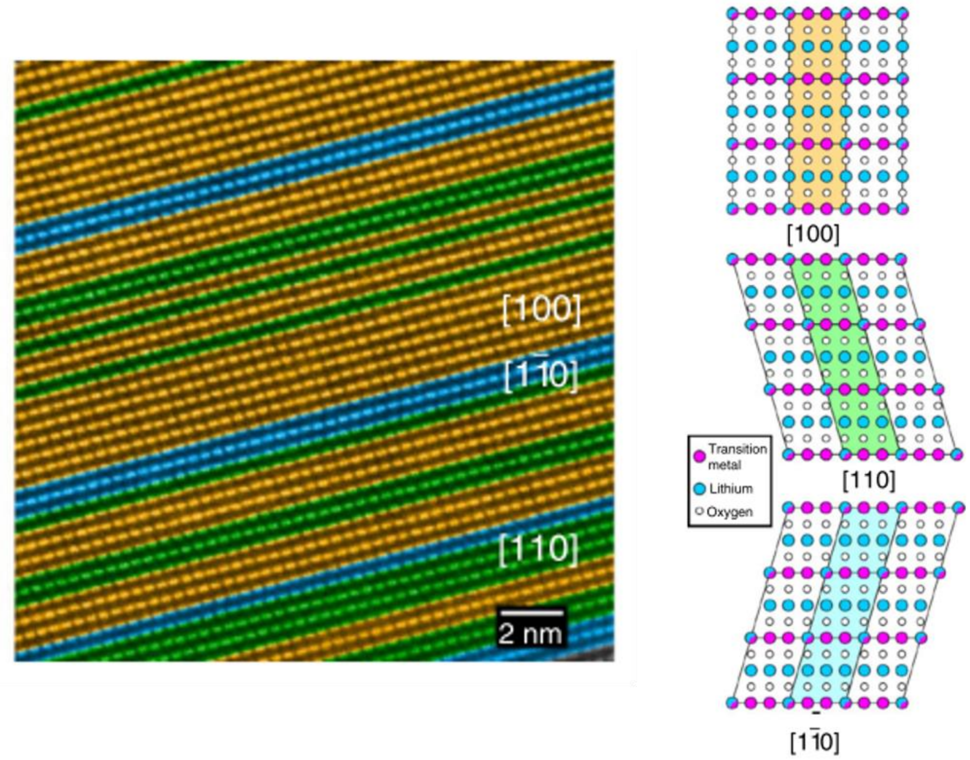

Figure 3.20 HAADF-STEM image showing the structure and three variants of $Li_{1.2}Mn_{0.54}Ni_{0.13}Co_{0.13}O_2$. The atomic model of the three variant directions are shown on the right. From reference [135].

Although the Li-rich oxides possess high initial capacity, these cathode materials bear major drawbacks in terms of voltage decay and capacity fade. Firstly, the Li-rich cathode materials exhibit an anomalous irreversible voltage plateau at about 4.5 V (vs Li+/Li) during the first charge, which leads to a poor first-cycle coulombic efficiency of the cell.[136] The large irreversible capacity after the first cycle has been proposed to result from simultaneous removal of Li and O from the cathode material, and is associated with structural modification.[37,136–138] It has been proposed from previous studies that that the oxygen evolution from the surface is accompanied by TM ion diffusion from the surface into the bulk (whereupon they enter Li vacancies generated by Li deintercalation), leading to material densification.[69,139] Boulineau et al. also reported the presence of a defect spinel phase at the particle surface after the first electrochemical cycle by using STEM imaging, as shown in Figure 3.21.[140,141]

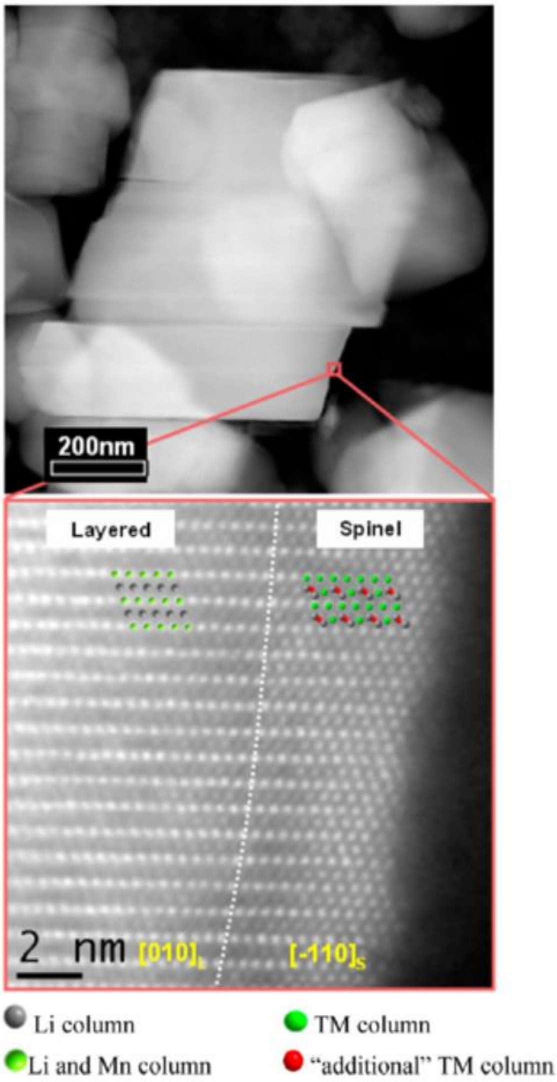

Figure 3.21 HAADF-STEM images showing the surface evolution of a $Li_{1.2}Mn_{0.61}Ni_{0.18}Mg_{0.01}O_2$ particle after the first cycle. From reference [141].

In addition, both voltage and capacity fade have been observed during the subsequent electrochemical cycles of Li-rich cathodes.[42,142–144] The "layered-to-spinel" transformation is commonly considered to play a vital role in the performance deterioration, and extensive studies using ex-/in-situ XRD, ND, TEM , SAED, etc. have been carried out to explore and validate the structural transformation of Li-rich oxides during cycling.[65,106,124,141,145–149] On one hand, there are some studies that have focused on detailing the structural transformation occurring at the material surface, but have paid less attention to the bulk material evolution.[106,141,146] On the other hand, although XRD and ND analysis could demonstrate the structural changes in the bulk material, they do not provide direct evidence of the spinel formation.[65,147,150] Structural changes such as unit-cell expansion, crystal defects or strain effects could all lead to peak shifts or broadening in the diffraction patterns, resulting in greater difficulties in identifying the spinel phase.

Daniel et al.[150] performed Rietveld refinement to the experimental ND data to examine the presence of spinel phase. They found that a better fit would be achieved when 15% $LiMn_2O_4$ spinel is included into the model. Although the results suggest the presence of a spinel phase, it is an indirect way to prove the phase existence and result in unanswered questions: (i) Whether TM cations occupy the tetrahedral sites in the spinel phase or not? Although their refinement shows better agreement when Li atoms are in tetrahedral sites and Mn atoms are in octahedral sites, they also pointed out that the possibility of Mn in tetrahedral site should not be ruled out. (ii) What is the composition of the spinel phase? There have been studies proposing the cycling-induced spinel phase to be $LiMn_2O_4$,[145,150] whereas the actual composition of the newly formed spinel phase is still unclear. For example, Sun et al.[145] reported that a β-MnO_2 phase would form during the first charge plateau and eventually transform into a $LiMn_2O_4$-type spinel phase, whereas no direct proof of the new phase composition is provided. (iii) How does the spinel phase distribute inside the active particles? XRD or ND results could only indicate the presence of the phases but not their spatial distribution. In previous TEM work, not all the studies investigated the bulk evolution, some of the work were only focused on detailing the structural changes at the surface region.[106,146,151]

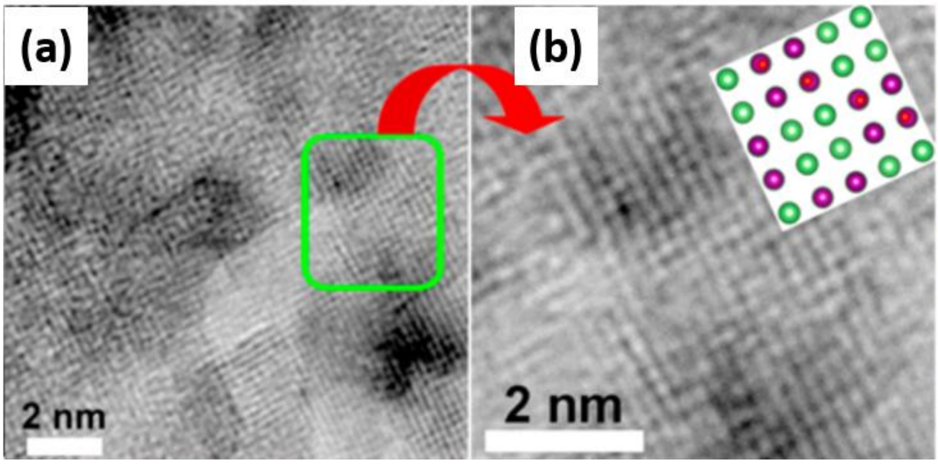

Figure 3.22 TEM images showing the nanoscale spinel phase formation in $Li_{1.2}Ni_{0.15}Co_{0.10}Mn_{0.55}O_2$ cathode after 100 cycles. Inset is the atomic model of [001] zone projection of cubic spinel phase (green: Li atoms; purple: TM atoms; red: O atoms).From reference [152].

Although there have been TEM observations showing the presence of disordered nanoscale domains in the bulk material,[128,148,149,152,153] some images are lacking of sufficient resolution to show the clear atomic structure. For example, from the HRTEM images shown in Figure 3.22, the author reported the formation of spinel-like $Fd\overline{3}m$ phase in cycled Li-rich cathode, whereas the images are lacking of sufficient resolution to clearly identify the structure.[152] In addition, some of the nanoscale domains with structural degradation might be more precisely interpreted as lattice defects rather than a well-defined spinel phase, such as the TEM image shown in Figure 3.23, from which the severe distorted lattice fringes are revealed in the image.[149] Moreover, the spinel and the layered phases could exhibit similar atomic-arrangement when observing the materials in specific orientations. For example, the $[001]_S$ orientation is a major zone axis of the $Fd\overline{3}m$ spinel structure and the cubic-like ordering projected in this orientation (Figure 3.24a) is often used for spinel phase identification, such as the image shown in Figure 3.22. However, we need to be cautious when differentiating between the spinel phase and the $R\overline{3}m$ layered phase by using images taken from such orientation, since the $[841]_R$ zone projection of the rhombohedral phase can also display a cubic-like atomic ordering similar to that, as can be seen from the atomic model in Figure 3.24b. Thus, it is not correct to index the phase from such orientations when no other evidence is provided. All these limitations make the new phase identification difficult. Based on previous studies, there are clearly still open questions regarding the evolution experienced by the lithium-rich cathodes during electrochemical cycling.

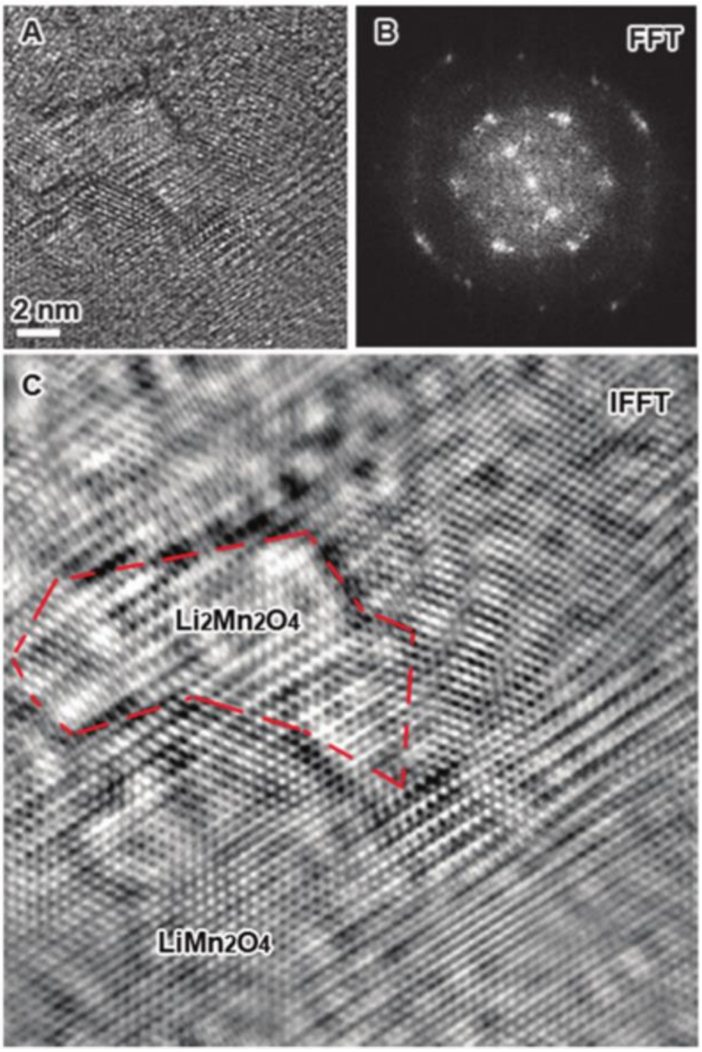

Figure 3.23 (a) TEM image of long-term cycled Li-rich cathode. (b) Fast Fourier Transform of the image shown in (a). (c) Fourier filtered image of (a). From reference[149].

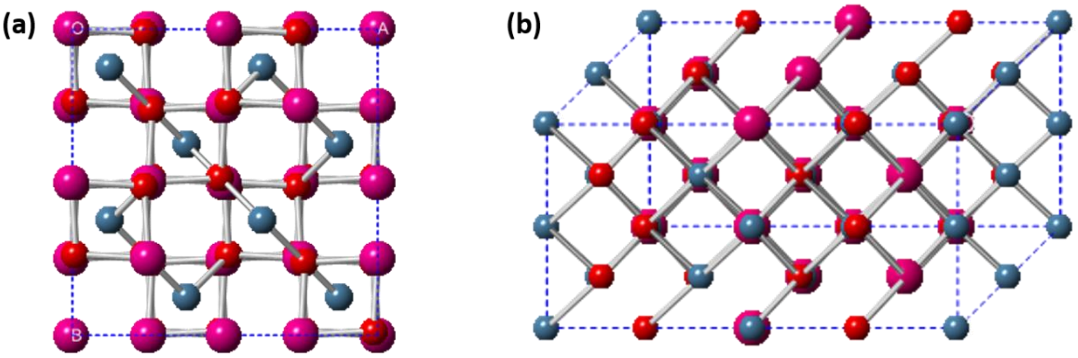

Figure 3.24 Atomic model of $LiMn_2O_4$-type $Fd\overline{3}m$ spinel structure and NMC-type $R\overline{3}m$ layered structure: (a) viewing along $[001]_S$ zone axis of spinel structure; (b) viewing along $[841]_R$ zone axis of layered structure. In the atomic model, Li atoms are shown in blue, O atoms are shown in red, TM atoms are shown in pink. Note that only TM atoms are visible from HAADF-STEM image.

In addition to these structural changes, the complex surface chemistry, including electrode-electrolyte interface reactions and possible TM cation dissolution into the electrolyte, can also lead to capacity fade and contribute to the overall cell impedance increase.[98,102,103,154,155] The electrolyte decomposition and reactivity of active material with electrolyte are important when cycling beyond the electrochemical stability window for the standard electrolytes, which is thus more prominent for Li-rich cathodes since the required upper cutoff voltage is usually above 4.6 V in order to achieve the high capacity. Dudney et al.[103] reported the surface film formation on a Li-rich cathode due to the oxidation of the electrolyte during electrochemical cycling between 2.5 V-4.9 V. Using XPS and micro-Raman analysis, they studied the composition of the surface film formed on the cathode surface during cycling, including surface fluorides (LiF), salt-based products such as Li_xPF_y and $Li_xPO_yF_z$, and polycarbonate from EC polymerization, which can cause an increase in the cell impedance as evidenced by the electrochemical impedance spectroscopy (EIS) data.

Up to now, researchers have attempted to use different modification methods to improve the structural stability and energy retention of lithium-rich cathodes, including inorganic or solid-electrolyte coating, such as AlF_3, Al_2O_3, LiPON;[152,156,157] spinel encapsulation and/or with additional surface coating;[158,159] other surface modification methods, such as surface treatment followed by post annealing;[160–162] doping;[120,163]

and the design of integrated layered-spinel structures.[164,165] Nevertheless, a better design of high-energy-density cathodes with improved cycling performance still relies on a complete understanding of the failure mechanism of the cathode materials during cycling. A detailed work on the chemical and structural changes of the lithium-rich cathodes is hence necessary.

In summary, the previous studies on the charge compensation mechanism and cycling-induced evolutions of a variety of layered cathode materials have been reviewed in this chapter. From the discussion, the remaining questions on the role of some TM species during charge-discharge and the structural and chemical evolutions at both the cathode surface and internal regions during electrochemical cycling are clearly stated. In this thesis, a detailed study on the chemical evolution and structural transformation of two kinds of layered cathodes has been performed using multiple electron microscopy techniques combined with other measurements at complementary length-scales, in order to unravel the mechanisms at the source of performance deterioration of lithium-ion batteries. The corresponding results will be presented and discussed in the next few chapters.

Chapter 4

Structural and Chemical Analysis of $LiNi_{1/3}Mn_{1/3}Co_{1/3}O_2$ Cathode Material

Lithium transition metal oxides are some of the most important types of cathode materials for lithium-ion batteries, which possess high capacity and relatively low cost. Nevertheless, as discussed in Chapter 3, these layered cathode materials suffer irreversible structural changes during electrochemical cycling that adversely impact the battery performance. Clear explanation of the cathode degradation process and its initiation, however, are still under debate and not yet fully understood. In this chapter, the chemical evolution and structural transformation of $LiNi_{1/3}Mn_{1/3}Co_{1/3}O_2$ (NMC) cathode material will be discussed. High-resolution electron energy loss spectroscopy (HR-EELS) is used to clarify the role of transition metals (TMs) in the charge compensation process. The local ordering of TM and Li layers in the bulk material upon cycling are revealed by the bulk sensitive ^{7}Li nuclear magnetic resonance (NMR) measurements.[†] In complement to the bulk measurements, we locally probe the surface structure and valence state distribution of cations in NMC cathode material using EELS and scanning transmission electron microscopy (STEM). The study depicts the charge compensation and degradation process of NMC using a combination of diagnostic tools at different length scales, which is of great importance in understanding the battery performance deterioration driven by the cathode degradation upon cycling.

[†] The NMR measurements and analysis were carried out by *Mark Dunham*, *Matteo Tessaro*, and *Kristopher Harris* from Gillian Goward's group at McMaster University.

4.1 Sample Preparation and Characterization Techniques

4.1.1 Electrochemical Test

The positive electrode consisted of $LiNi_{1/3}Mn_{1/3}Co_{1/3}O_2$ (NMC, Toda America Inc.), acetylene black and polyvinylidene fluoride (PVDF) in an 80:10:10 weight % ratio. NMC and CB were ground together for 30 minutes and dried, then a solution of 3% PVDF (by weight) in N-methyl-2-pyrrolidene (NMP) was added and the resultant slurry was stirred for 2-3 hours. The slurry was cast onto aluminum foil and the NMP was evaporated in an evacuated drying oven at 110 ^{o}C for 12 hours. Discs, 1.27 cm in diameter, were punched and coin cells were assembled in an argon atmosphere glove box. The average mass of NMC in each cell was 8 mg. The anode used was lithium metal and the electrolyte was $LiPF_6$ in ethylene carbonate/dimethyl carbonate. Coin cells were cycled with a Arbin battery testing equipment and MITS Pro software at room temperature. The cells were cycled galvanostatically between 2.5-4.6 V at rates of C/10 and were held potentiostatically at various voltages until the measured current was less than 5 μA (i.e. the rate was approximately C/200). The cyclic curve for the long-term cycled cells are shown in Figure 4.1.

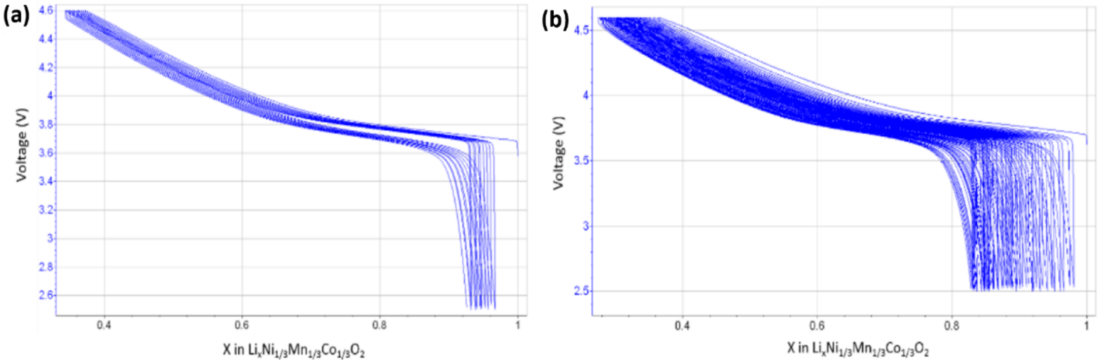

Figure 4.1 Galvanostatic charge-discharge curves of NMC electrodes of (a) 20 cycles, (b) 50 cycles.

4.1.2 Transmission Electron Microscopy Characterization

For charge compensation analysis, EELS data of NMC cathode during the first cycle were acquired using a FEI Titan 80-300 kV microscope equipped with a spherical aberration corrector of the imaging lens, a monochromator, and a high-resolution spectrometer (Gatan Image Filter Tridiem 965). An energy resolution of ~0.08 eV was achieved using the monochromator, as given by the full width at half maximum of the zero-loss peak (ZLP). The microscope was operated at 80 kV and the spectra were recorded in STEM mode, using the spectrum imaging technique, with 0.1 eV/channel dispersion of the spectrometer. Multiple particles were examined at each state of charge (SOC) to estimate the average valence of the TMs in NMC. The structural analysis of the long-term cycled NMC cathodes were carried out on an aberration corrected (probe and image-forming lenses) FEI Titan Cubed 80-300 kV microscope operated at 80 kV in STEM mode. The STEM images were acquired using a high-angle annular dark-field (HAADF) detector with collection angle range of 64 to 200 mrad. The HAADF-STEM image acquired with a HAADF detector is also called a “Z-contrast” image, where the image intensity is proportional to the atomic number of the elements present.[166] EELS spectra for the long-term cycled samples were collected with 0.25 eV/channel dispersion of the spectrometer. The nano-beam electron diffraction patterns were acquired by reducing the convergence angle to ~1.2 mrad, leading to an electron probe size of a few nanometers.

To prepare the specimen for TEM analysis, the cycled cells were dissembled in an argon-filled glovebox and the NMC cathodes were washed and dried. Then the cathode particles were scraped from the current collector and suspended on a copper grid with holey carbon in the glovebox. The specimen for EELS analysis was sealed in the argon atmosphere using a vacuum transfer holder (Gatan Model 648) during the sample transfer process to the microscope. The specimens of long-term cycled NMC cathodes (20 and 50 cycles) were prepared using a Zeiss NVision 40 dual beam, focused ion beam-scanning electron microscope (FIB-SEM), for further structural analysis.

4.1.3 NMR Spectroscopy

All ^{6}Li and ^{7}Li magic-angle spinning MAS NMR spectra were acquired under a 4.7 T applied magnetic field using a Bruker DRX console. The sample, isotopically enriched with ^{6}Li, was prepared from ^{6}LiCO$_3$, as described previously.[167] Spectra are referenced to 1M LiCl$_{(aq)}$ at 0 ppm. The ^{6}Li Hahn-echo NMR spectrum was collected with 46 kHz sample spinning in a specially built probe supporting 1.8 mm rotors, and employed 1.7 μs 90° pulses and 0.5 s recycle delays. All ^{7}Li NMR spectra were collected using 1.3 mm rotors at a 60 kHz sample-spinning rate using a Bruker high speed MAS probe. ^{7}Li Hahn-echo spectra were collected using 1 μs 90° pulses and 50 ms recycle delays. ^{7}Li spectra containing only isotropic shifts were generated using the projection magic-angle-turning phase-alternating spinning-sideband, pj-MATPASS,[168] method of separating sidebands into different slices of a 2D spectrum, which were then aligned and summed to yield the presented spectra. ^{7}Li pj-MATPASS spectra were collected using slightly more conservative rf power and recycle delay settings (1.5 μs $\pi/2$ pulses and 100 ms delays) than the Hahn-echo spectra.

4.2 Characterization of Pristine NMC

The morphology of pristine NMC powder is shown in Figure 4.2a, demonstrating that the NMC cathode material consists of large secondary particles with diameters in the range of 5-20 μm.[36] These large NMC secondary particles are composed of numerous primary particles which are hundreds of nanometers in diameter, as shown in Figure 4.2b. The pristine NMC cathode material has a layered structure ($R\bar{3}m$ space group), where lithium and transition metal ions occupy the alternating octahedral sites between the oxygen layers, as shown in the atomic model in Figure 4.2c. Figure 4.2d shows an atomic-resolution HAADF-STEM image of NMC particle. The corresponding Fourier transform (FT) diffractogram is shown in the inset at bottom left in Figure 4.2d, which can be indexed to $[11\bar{2}0]_R$ zone axis. Note that the bright atomic columns and related atomic planes in the HAADF-STEM image shown in Figure 4.2d are the TM layers, while the lighter elements, lithium and oxygen (shown in the corresponding atomic model), are not visible in the image due to their low atomic number.

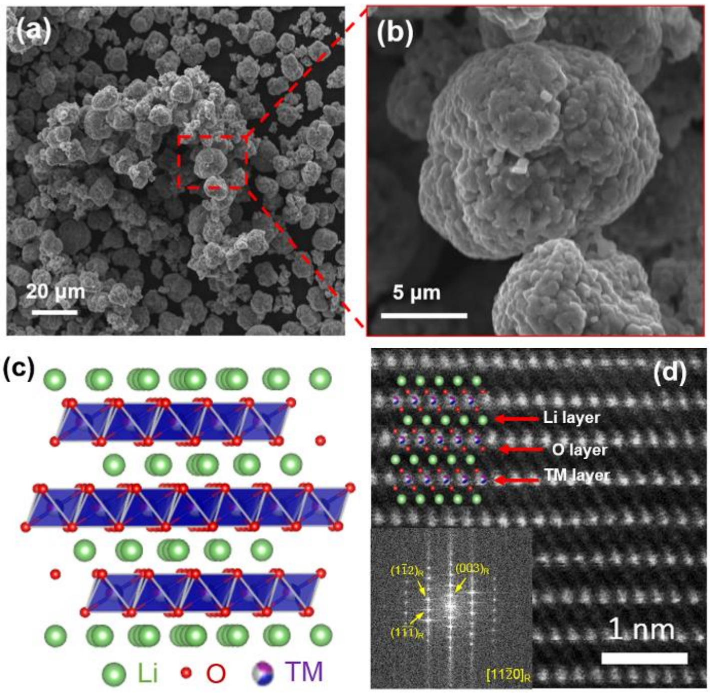

Figure 4.2 Electron microscopy characterization of pristine NMC cathode material. (a-b) SEM images of pristine NMC. (c) Atomic model of NMC showing the layered $R\bar{3}m$ structure. (d) An atomic-resolution STEM image of a pristine NMC particle along $[11\bar{2}0]_R$ zone axis, the corresponding Fourier transform diffractogram is shown in the inset. The subscript R denotes $R\bar{3}m$ structure.

4.3 Charge Compensation of NMC at Different SOCs

As discussed in Chapter 3, there are still remaining questions on the role of TMs in charge compensation process. Herein, the electronic structure of NMC cathode material during charge-discharge process along with delithiation-lithiation was studied using high-resolution EELS in order to elucidate the evolution of oxidation state of the transition metal cations. EELS spectra of Mn, Co and Ni $L_{2,3}$-edges were collected from a series of *ex-situ* cathode samples at different SOCs during the first cycle, as shown in Figure 4.3. The $L_{2,3}$-edges of transition metals are attributed to the electronic transition of electrons from $2p_{3/2}$ and $2p_{1/2}$ core states to the unoccupied $3d$ states. The dipole-allowed $2p \rightarrow 3d$ transition in Mn, Co, and Ni leads to sharp features in fine structures of the $L_{2,3}$-edge which are very sensitive to the oxidation and spin state, therefore, bringing qualitative information on the electronic structure of the transition metal ions. Extensive EELS analysis was performed at each SOC in this study, spectra shown in Figure 4.3b-d represent the general trend observed from all the samples. The $L_{2,3}$-edge spectra with label "1" (Figure 4.3b-d) were acquired from the pristine NMC sample. The oxidation state of Mn, Ni and Co are determined to be Mn^{4+}, Co^{3+} and Ni^{2+} based on the near-edge fine structures of the $L_{2,3}$-edges.[82] Interestingly, we noticed that the electronic structure of TM cations are not constant from the particle surface to the bulk during cycling, indicating an inhomogeneous valence distribution of TMs. Therefore, the electronic structure of Ni, Mn and Co cations in the surface and bulk will be discussed separately in the following content.

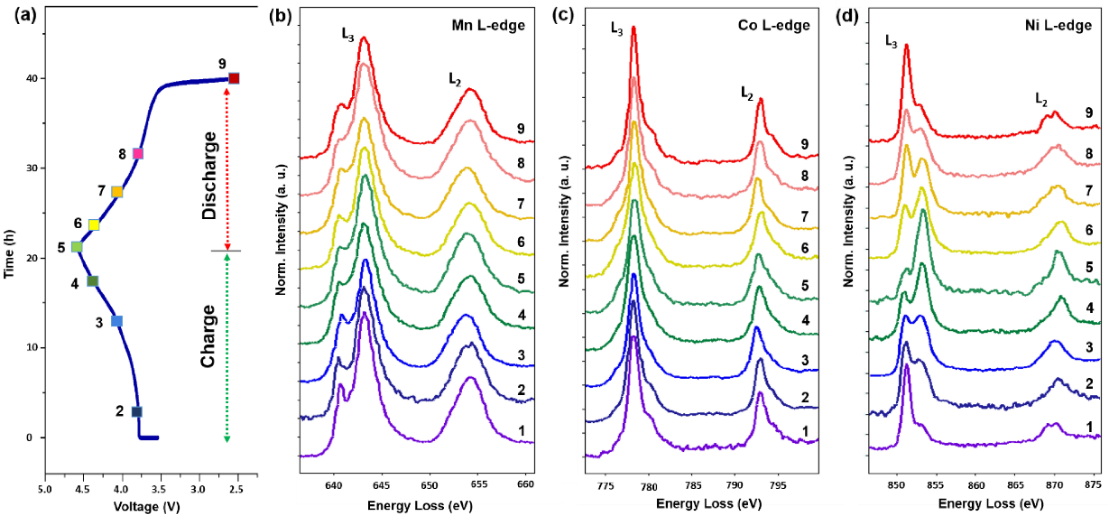

Figure 4.3 Voltage profile (a) and normalized EELS spectra (b) Mn, (c) Co and (d) Ni $L_{2,3}$-edges of the NMC cathode with respect to different SOCs during first cycle at the corresponding conditions identified in (a).

The $L_{2,3}$-edge EELS spectra labeled "2" to "9" in Figure 4.3 were obtained from the bulk region of the NMC particles at different SOCs. As illustrated in Figure 4.3b and c, both Mn and Co $L_{2,3}$-edges present very little change in the peak features at different SOCs with respect to the electrochemical untreated sample (spectra “1”). The results indicate that there is no obvious change in the oxidation state of these two TMs during delithiation and lithiation processes. Both Mn and Co remain at their tetravalent and trivalent oxidation states respectively, suggesting that these two TM cations are relatively unaffected with Li ion removal. In contrast, significant changes are observed in the Ni $L_{2,3}$-edges during the charge-discharge process (Figure 4.3d). A splitting in the Ni L_3-edge with a double-peak feature including a strong lower-energy peak (~852.2 eV) and a weak higher-energy peak (~854.2 eV) is observed in the high-resolution EELS spectrum of the pristine sample (spectrum “1”) due to the multiplet and crystal field effect in octahedral symmetry.[169,170] The variation of the intensity ratio between these two peaks fingerprints the oxidation state of Ni cations. Upon charging (spectra “2” to “5”), the intensity ratio of high-energy peak over the low-energy peak of the Ni L_3-edge increases dramatically and the overall L_3-edge shifts toward higher energy, indicating an oxidation of Ni^{2+} to Ni^{4+} during Li extraction.[170,171] The chemical shift of Ni L_3-edge towards higher energy is indicative of a change in the valence of TM cations to higher oxidation states, although we cannot exclude that few Ni cations at lower oxidation state may still exist. Furthermore, since EELS results reveal that both Mn and Co remain unchanged during the charge, Ni cations would be oxidized to their tetravalent state to compensate the Li removal at top of charge. This is also consistent with the NMR result that will be discussed below. During discharge (spectra “6” to “9”), when Li ions are inserted back into the cathode material, the oxidized Ni cations are gradually reduced back to the divalent state at 2.5V discharge, evident by the Ni L_3-edge fine structure change associated with the peak shifting back towards lower energy loss. The dominant variations in Ni $L_{2,3}$-edges clearly show that the redox reaction of $Ni^{2+} \leftrightarrow Ni^{4+}$ primarily compensates the charge transfer due to delithiation-lithiation process, whereas both Mn^{4+} and Co^{3+} are inactive during the process. The HR-EELS study elucidates the debate on the role of TMs (particularly Ni and Co) in the charge transfer process, which provides useful guidance for the design of high energy density cathode materials.

Lithium NMR spectroscopy was also used to study NMC at different SOCs because the spectrum is uniquely sensitive to the electronic state of the paramagnetic metals surrounding each lithium ion.[172,173] As discussed in our work from Ref 36, and summarized here, Figure 4.4a shows the ^{7}Li MATPASS NMR spectra of NMC at different SOCs during the first cycle. For pristine NMC, the Li ions in the Li layer give rise to the broad peak centered at 500 ppm. The broad peak feature is attributed to a variety of coordination environments of TMs in the coordination spheres of Li ions that give rise to different chemical shifts. Meanwhile, the cation mixing of Ni^{2+} and Li^+ leads to the presence of Li ions in the TM layers, which gives rise to a weak peak located at ~1300 ppm. As shown in Figure 4.4a, the Li ions are deintercalated from NMC during charging, evident by the decreased intensity in the peaks from the ^{7}Li NMR spectra. There are remaining Li ions in NMC at 4.6V charged state as the two peaks at 360 ppm and 100 ppm are clearly observed from the NMR spectrum. Meanwhile, the constant shift of ^{7}Li NMR peaks towards lower frequency and the appearance of the two distinct peaks reveal the existence of Mn^{4+} and Ni^{2+} local ordering in the TM layer of NMC cathode material. After discharged to 2.5 V, the ^{7}Li NMR spectrum shows identical features with the pristine NMC spectrum, indicates that the Li deintercalation-intercalation process is reversible, where the Li ions are mostly intercalated back into the NMC cathode during discharge. The results thus suggest that there is no obvious change in the structure of the bulk material after charge-discharge. In addition, the ^{7}Li NMR spectra acquired at 4.6 V charged state from the NMC cathode after the first and tenth cycle exhibit similar line shape and chemical shifts, as shown in Figure 4.4b. This indicates that the local ordering of the TM layers in the bulk material is maintained after multiple electrochemical cycles.†

---

† For more detailed analysis of NMR spectra, please refer to our work in Ref 36.

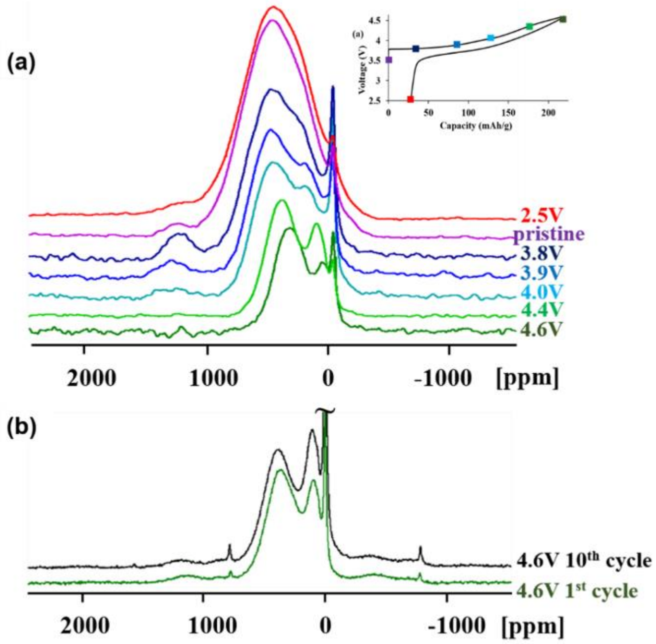

Figure 4.4 (a) ^{7}Li MATPASS NMR spectra of NMC cathode at different SOCs on the first cycle. The inset shows the galvanostatic cycling curve, where the colored boxes indicate the SOC at which the cathodes were extracted from coin cells and analyzed by NMR. (b) ^{7}Li 60 kHz Hahn Echo MAS NMR spectra of NMC cathode stopped at 4.6V at the first and the tenth cycle.

4.4 Structural Evolution of NMC during Cycling

It should be noted that the NMR spectra above provide a bulk measurement of NMC particles. Details of the surface behavior of charged particle, as observed by STEM-EELS, reflect notable differences which are not detected by NMR. Interestingly, it is noticed that when Li ions are extracted from NMC during charging, the TM cations are in lower oxidation states at the surface comparing to the bulk region, and this surface reduction effect was still observed until the end of discharge. The valence maps of TMs from charged NMC are provided to illustrate this surface reduction phenomenon, as shown in Figure 4.5. An EELS spectrum image (SI) was acquired from a region of interest (ROI), marked in the STEM image shown in Figure 4.5a, where each pixel of the ROI contains an EELS spectrum. The valence maps of Mn, Co and Ni were obtained using the multiple linear least square (MLLS) method from EELS SI with reference spectra shown in Figure 4.6 (details of the MLLS method is shown in Appendix I).

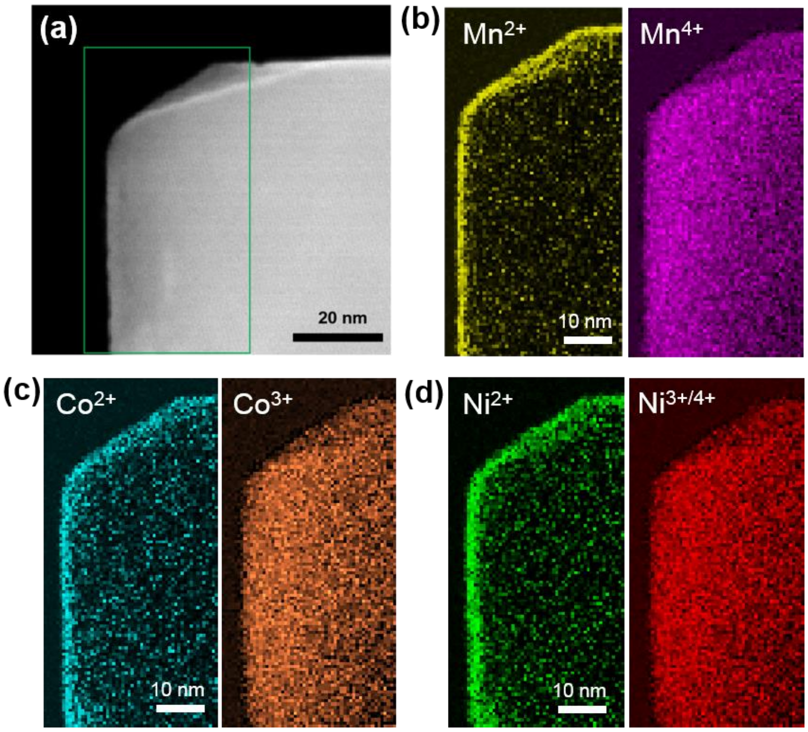

Figure 4.5 Valence maps for a 4.1V charged NMC particle. (a) HAADF-STEM image of a 4.1V charged NMC particle. (b) Mn, (c) Co and (d) Ni valence maps of the NMC particle shown in (a). The valence maps of Ni, Mn and Co are represented by the fitting coefficient maps of the corresponding reference spectra deduced from the MLLS analysis, which can be interpreted as the weights of the corresponding references at each pixel. More details are included in Appendix I.

The Mn valence maps shown in Figure 4.5b clearly demonstrate that the Mn cations in lower oxidation state were mainly located at the edge of the particle, whereas the Mn in the bulk remains in tetravalent state, indicating that the Mn^{4+} cations have been reduced at the surface region with a thickness of about 2 nm. The corresponding reference spectra of the Mn $L_{2,3}$-edges are shown in Figure 4.6a, where the surface Mn L_3-edge spectrum (in yellow) shows a chemical shift of about 3 eV towards lower energy compared with the bulk Mn^{4+} spectrum (in purple) indicating a reduction of the Mn cations.[174] Although the thickness of this layer shows some variations among different particles, the majority of charged particles exhibit this surface reduction effect. Similar surface valence reduction is also observed in the case of Co and Ni. The Co cations are reduced at the particle surface comparing to the bulk Co^{3+} as shown in Figure 4.5c. The corresponding reference spectra are shown in Figure 4.6b, the Co $L_{2,3}$-edge spectrum (in red) shows consistent features with Co^{3+}, while the Co $L_{2,3}$-edge shown in blue exhibits a clear shift towards lower energy comparing to the Co^{3+} spectrum suggesting a reduction to the divalent state.[175,176] The surface reduction effect is also present in the Ni valence maps shown in Figure 4.5d. Because the cathode is in delithiated state, Ni ions in the bulk were oxidized to higher valence which are labelled as "$Ni^{3+/4+}$" in this case. The corresponding Ni $L_{2,3}$-edge reference spectrum (in red) exhibits a positive shift towards higher energy comparing to the Ni^{2+} (in green) obtained near the surface indicating a higher oxidation state, as shown in Figure 4.6c. In contrast to the bulk, Ni cations in the surface layer were reduced to divalent state as shown in Figure 4.5d.

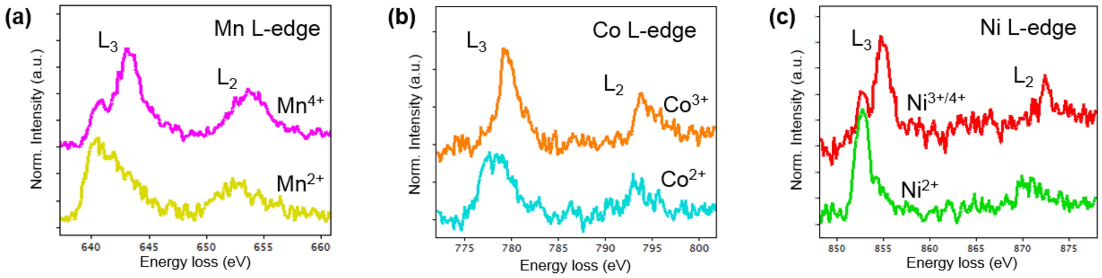

Figure 4.6 Reference spectra of (a) Mn, (b) Co and (c) Ni $L_{2,3}$-edges used for MLLS analysis. All the reference spectra were obtained from the experimental data at the surface region and bulk region.

The homogeneity of TM valence state in pristine NMC was evaluated before electrochemical tests by STEM-EELS, as shown in Figure 4.7. As can be seen from Figure 4.7b that both the O K-edge and Mn $L_{2,3}$-edges have similar peak features from the surface to bulk, there is almost no change observed in the Mn $L_{2,3}$-edges. The result, therefore, indicates there is no oxidation state gradient from the surface to bulk in pristine NMC.

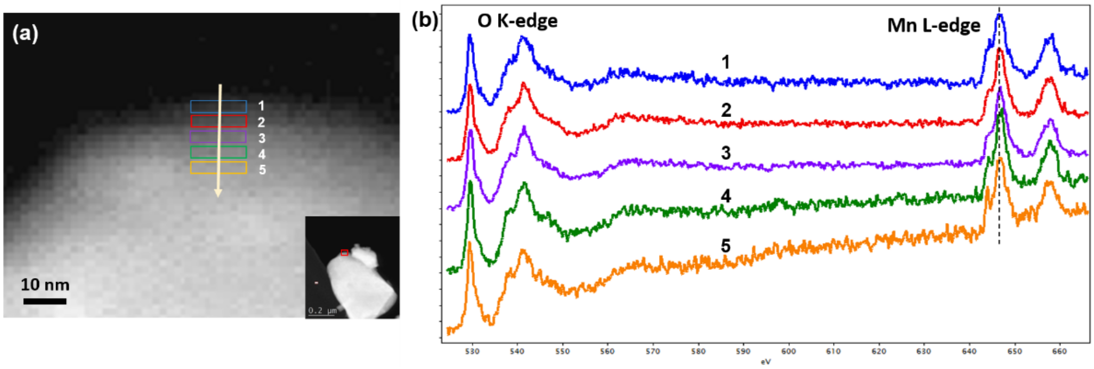

Figure 4.7 EELS spectra profile of pristine NMC. The O K-edge and Mn $L_{2,3}$-edge are shown here to demonstrate the consistency of the electronic structure of NMC.

The reduction of Ni cations at the surface is in apparent conflict with the expected oxidation reaction of the TM at surface, since Li ions tend to be primarily extracted from the particle surface and resulting in an oxidation of the Ni^{2+} cations. In contrast, the three TMs are reduced to lower oxidation state at the particle surface as comparing to the bulk, indicating that the change of the oxidation state of TMs is not simply based on the degree of Li ion removal. The valence gradient of Ni has also been observed from a previous study, where Ni cations were in lower oxidation states at the surface (Ni^{3+}) compared to bulk (Ni^{4+}),[82] and it was suggested by the authors that the oxygen *2p* hole state may play a role in compensating the charge transfer at the surface. However, this explanation is insufficient to explain the surface reduction observed in the present study, where not only Ni is in a lower valence state at the surface, but both Mn and Co are reduced to lower oxidation state. The significant change in the electronic structure of TM cations must be associated with local structure distortion and/or rearrangement of the surrounding atomic environment. Hwang et al. proposed that the kinetic effects induced by Li ion removal could play an important role in the phase transition of layered cathode material.[177] They suggested that the great number of Li vacancies would facilitate the phase transition resulting from the increased cation migration. Considering the kinetics of lithium diffusion, more Li ions are primarily extracted from the surface, resulting in excess Li vacancies located near the surface region and promote the phase transition. Besides, it has been reported by Alva et al. that the oxidized Ni ions (Ni^{4+}) are prone to facilitate the electrolyte decomposition reaction at the electrode surface,[178] which may also influence the surface chemistry of the cathode. Therefore, the surface reduction observed in the first charge may due to combination effects including the significant Li vacancies generated at the surface and the parasitic side reactions with electrolyte during delithiation. Our study on the long-term cycled NMC cathodes herein provides direct evidence of the relationship between the surface reduction and the crystallographic structure evolution, as will be discussed below.

The surface reduction effect is further observed in the NMC cathode after 20 electrochemical cycles at fully discharged state, evident by the EELS spectra acquired from the particle surface region and bulk region (Figure 4.8). Figure 4.8b illustrates the O K-edge acquired at the particle surface and in the bulk. The pre-peak of O K-edge located at ~ 529 eV, marked with a red arrow, is attributed to the transition of O *1s* core state to *2p* states which are highly hybridized with the TM *3d* states. Therefore, the intensity change of the O K-edge pre-peak reflects the variation of the oxidation states and coordination of the transition metal ions. This pre-peak drops significantly at the surface region compared to the bulk region, indicating that the valence of the TM cations and the coordination environment of the oxygen atoms drastically change. In particular, the drop of sharp peak at around 528eV could be indicative of a lower number of hybridized O *2p*-TM *3d* holes at the oxygen sites, fully consistent with a lower valence of the cations shown from the TM L_{23}-edges on the same location. Such detailed information regarding the TM valence change can be obtained from the transition metal L_{23}-edges, as shown in Figure 4.8c-4.8e. The Mn L_3-edge acquired in the bulk region (Figure 4.8c) shows features consistent with Mn^{4+} whereas a clear chemical shift (about 3eV) of Mn L_3-edge towards lower energy is observed near the surface as compared to the bulk, hence demonstrating that Mn ions have been reduced to the divalent oxidation state near the surface.[174] A similar change is observed at the Co L_3-edge (Figure 4.8d), where a chemical shift towards lower energy is observed in the surface layer as compared to the bulk, indicating the trivalent Co ions have been reduced to Co^{2+} at the surface.[175,176] In contrast, the Ni L_{23}-edges show no obvious change from the cycled bulk to surface, indicating that nickel is mostly at Ni^{2+}.

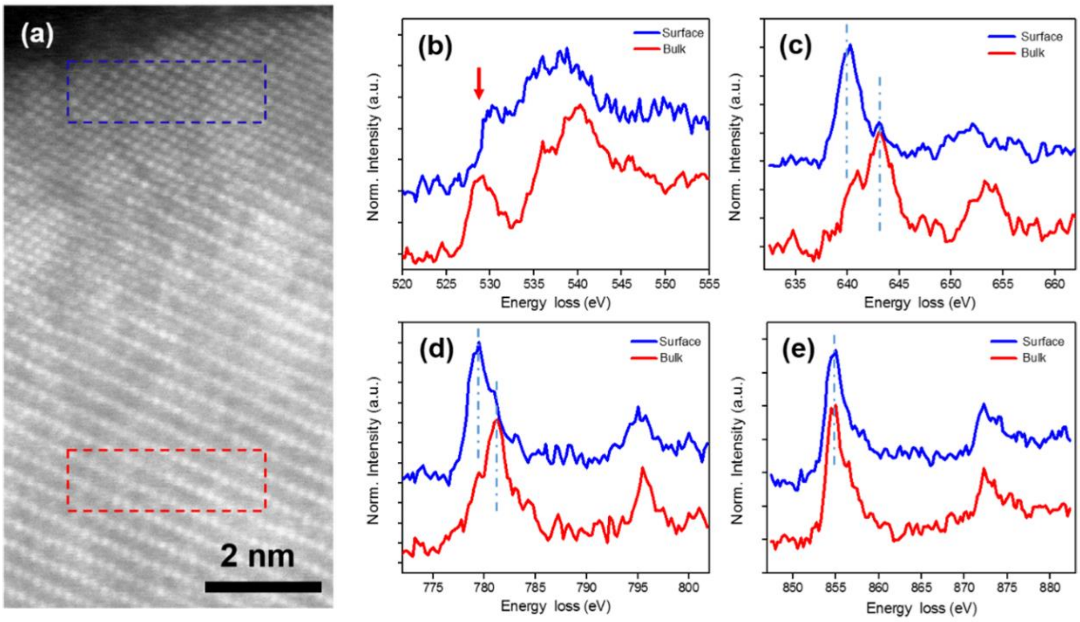

Figure 4.8 (a) Atomic-resolution HAADF-STEM image of NMC cathode after 20 cycles. (b) O K-edge, (c) Mn, (d) Co and (e) Ni $L_{2,3}$-edges EELS spectra from the surface layer (blue spectra) and bulk (red spectra), respectively.

From the results presented above, EELS analysis provides direct evidence of the surface cation reduction by examining the local electronic structure changes. Moreover, this chemical evolution is revealed to be associated with structural change from direct visualization of the local atomic arrangement. The structural change is clearly observed from the cycled surface to the bulk, as shown in Figure 4.8a. The bulk region of NMC particles maintain the well-defined $R\overline{3}m$ layered structure, consistent with the NMR results showing overall stability of the structure. In contrast, the layered structure with alternating bright and dark atomic planes is no longer visible near the particle surface, while the bright atomic columns appear in the initial Li layers, forming a surface reconstruction layer with the thickness of about 3-5 nm. This is indicative of migration of TM cations into the Li layer. As previously stated, Li atoms are not visible from the HAADF-STEM image due to their low atomic number, therefore, the prominent change in the contrast of the Li layer suggests that a significant amount of TM cations are occupying the lithium 3a sites. In contrast, the bulk region of NMC particles maintains the well-defined $R\bar{3}m$ layered structure, consistent with the NMR results showing overall stability of the structure. Therefore, the reduction of TMs is associated with the structural transformation at the surface.

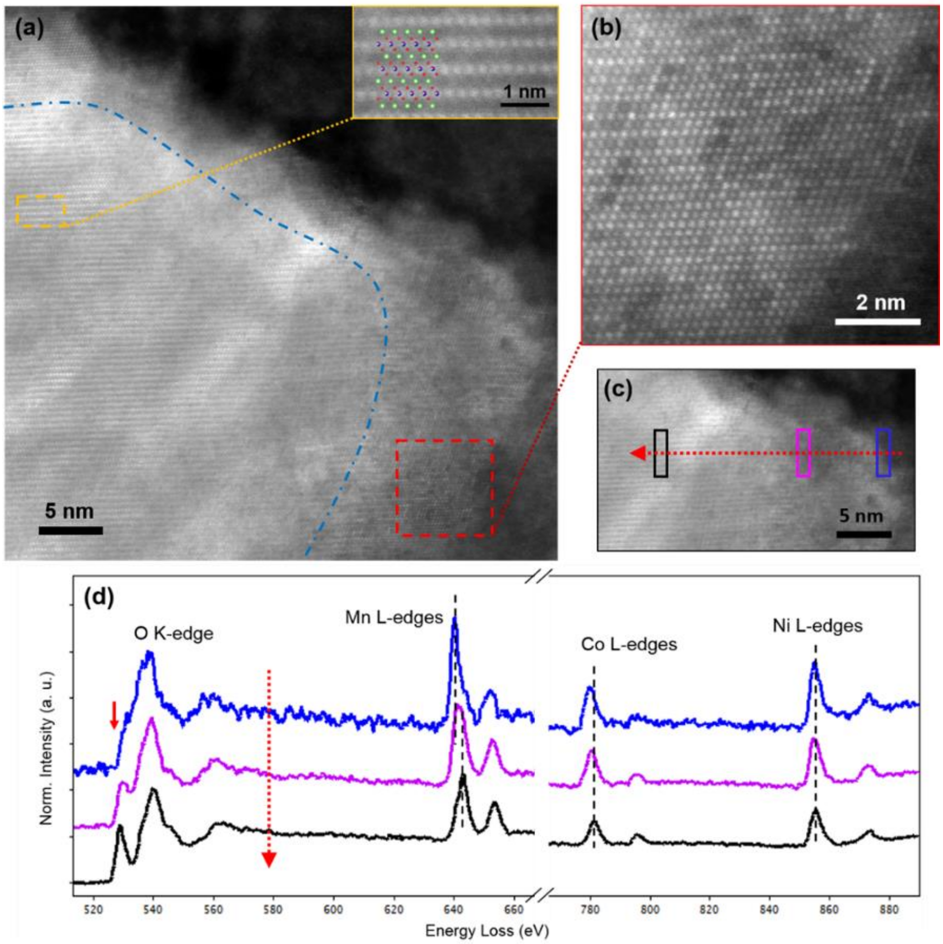

Figure 4.9 (a) HAADF-STEM image of NMC cathode after 50 cycles. (b) Atomic-resolution STEM image showing the surface transition layer of the highlighted region in (a). (c,d) EELS spectra of 50-cycle NMC acquired from the particle surface into bulk, the corresponding locations are marked in the STEM image (c).

The thickness of the surface reduction layer increases significantly to about 15 nm in some regions of the NMC cathode material after 50 cycles, as shown in Figure 4.9a and 4.9b. The bulk region of the 50-cycle sample maintains the $R\bar{3}m$ layered structure (a higher-magnification STEM image showing the bulk structure detail is inserted at the upper right corner in Figure 4.9a). The series of EELS spectra obtained from the particle surface into the bulk show that the Ni $L_{2,3}$-edge have consistent features and the corresponding L_3/L_2 peak ratio shows minor variation (Figure 4.10), indicating there is no valence change in the divalent Ni ions (Figure 4.9d). In contrast, significant chemical shift towards lower energy of the energy onset of Mn and Co L_3-edges and the obvious L_3/L_2 ratio decrease (Figure 4.10) highlight that Mn^{4+} and Co^{3+} ions are gradually reduced to Mn^{2+} and Co^{2+} at the surface layer, respectively. This valence change is similar to the one observed from the 20-cycle NMC cathode discussed above. Furthermore, it is noticed that the Mn^{4+} and Co^{3+} do not undergo abrupt chemical changes. The TM cations are gradually reduced to divalent states via a transition zone, indicating by the gradual shift of Mn and Co L_3-edges (Figure 4.9d) and the intermediate L_3/L_2 value of the transition zone (Figure 4.10). This transition zone will be discussed in more details below. In addition, the O K-edge also shows a decrease in the pre-peak intensity from bulk to surface which is consistent with the observed TM valence reduction.

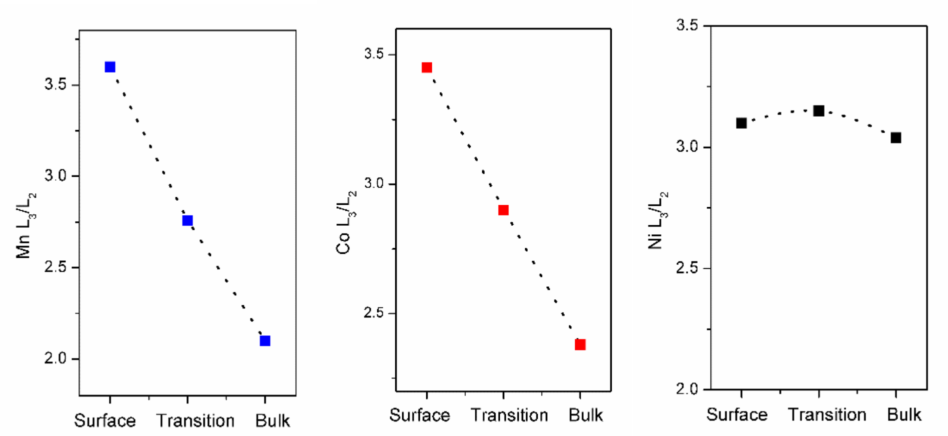

Figure 4.10 L_3/L_2 ratio of Mn, Co and Ni for NMC after 50 cycles. The three ratios were calculated from the corresponding EELS spectra (Figure 4.10) acquired from the surface layer (Surface), transition zone (Transition) and bulk region (Bulk).

Phase transformation of the cycled NMC particle is further validated by the nano-beam electron diffraction (NBED) patterns acquired from the particle surface into the bulk, as shown in Figure 4.11. The NBED illustrates that there are three type of phases located from the surface to the bulk. The NBED pattern obtained in the bulk region of the 50-cycle NMC particle (Figure 4.11e) shows identical layered structure symmetry and can be indexed to $[2\bar{1}\bar{1}0]_R$ zone axis of the $R\bar{3}m$ space group. The result thus indicates that the bulk of NMC particle maintains the layered structure after electrochemical cycling, which is consistent with the previous HAADF-STEM images and the valence of TMs (Mn^{4+}, Co^{3+}, Ni^{2+}). In contrast, when probing into the outer-most layer, the diffraction spots corresponding to the alternating arrangement of Li and TM layers (some are marked with arrows) disappears and the corresponding NBED can be indexed to a $Fm\bar{3}m$ rock-salt (RS) structure viewed along $[110]_F$ zone axis, as shown in Figure 4.11c. This suggests a structural transformation from the ordered layered structure to a disordered RS phase where Li-TM layered ordering no longer exists. Figure 4.11b shows the simulated HAADF image and atomic model corresponding to the rock-salt $[110]_F$ orientation, which are in good agreement with the experimental image.

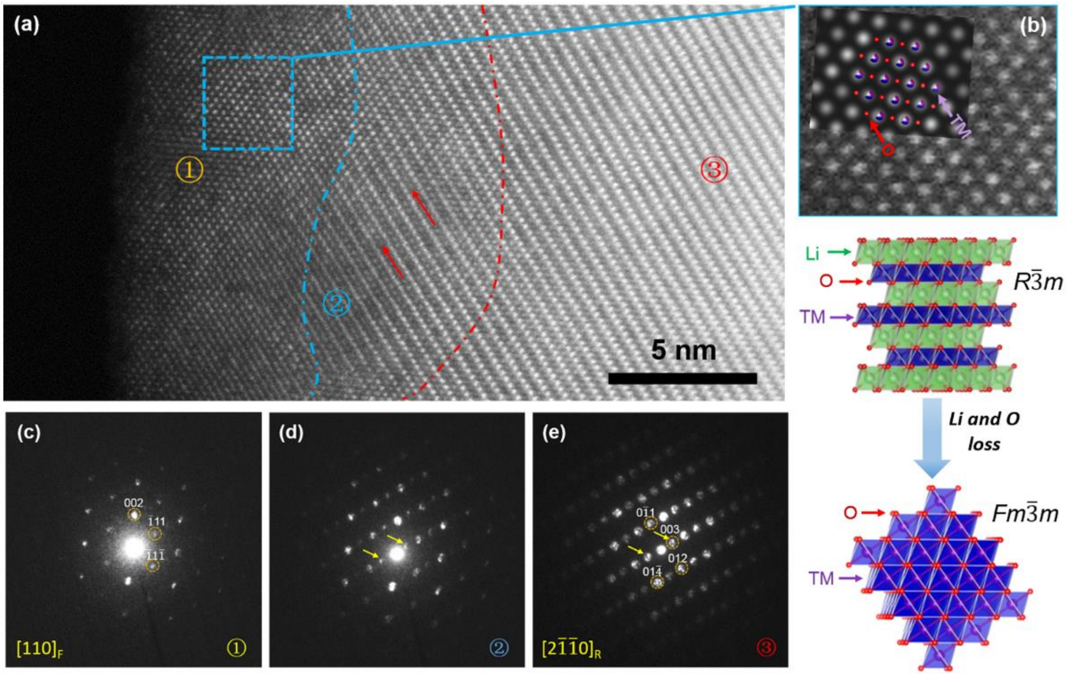

Figure 4.11 Structural evolution of NMC cathode material after 50 cycles. (a) Atomic-resolution HAADF-STEM image of 50-cycle NMC particle. (b) Details of the surface RS structure. The corresponding simulated HAADF image is shown in the inset on the top left corner, the atomic model below illustrates the structural transformation of NMC. (c-e) Nano-beam electron diffraction patterns acquired from the particle surface to bulk. The corresponding regions are labelled in (a). The subscript F and R denote $Fm\bar{3}m$ and $R\bar{3}m$ structures.

EELS quantification shows that the O to TM ratio within this RS layer decreases significantly as compared to the bulk layered structure (LS) region (1.95(RS)→1.15(LS)), indicating that the new phase formed on the surface is oxygen deficient. Meanwhile, almost no Li can be detected in the surface RS layer compared to the bulk region, as highlighted by the significant intensity drop of the Li K-edge from bulk to surface (Figure 4.12). The results suggest that the cycled NMC particle surface layer consists primarily of a transition metal oxide (TMO)-type RS phase with $Fm\bar{3}m$ structure, in good agreement with the valence reduction of TM cations (reduced to Mn^{2+}, Co^{2+}, and Ni^{2+}) and the O K-edge feature at the surface. It is also observed that the O to TM ratio obtained from the surface layer is slightly higher than 1:1 expected for a pure TMO phase, indicating that there may be a very small amount of residual Li ions or vacancies at the cation site of the surface RS structure. This hypothesis is supported by the important atomic-column to atomic-column contrast variation at some TM sites as seen in Figure 4.9b and Figure 4.11a. The features in Figure 4.9b may also suggest that there is some correlation between the residual dark columns (possibly either Li atoms or vacancies) appear to be close to each other.

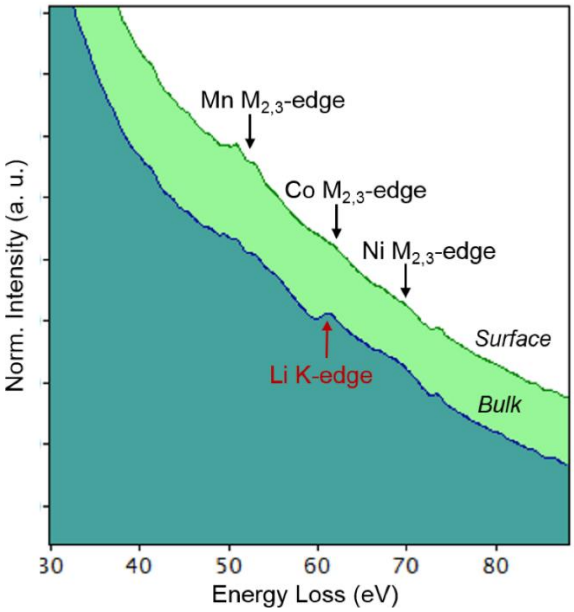

Figure 4.12 Li K-edge spectra acquired at the surface reduction layer and the bulk region from the NMC cathode after 50 cycles. The background subtraction is not applied to the Li K-edge due to the complexity of spectrum arising from the existence of the adjacent Mn $M_{2,3}$-edge and Co $M_{2,3}$-edge, as labelled in the spectrum.

In addition, an intermediate region is observed between the outermost RS layer and the bulk LS region. From the high-resolution HAADF-STEM image shown in Figure 4.11a, the intensity within the Li layers increases gradually from the particle interior to the surface RS region, indicating that the Li sites were partially occupied by the TM atoms at this transition zone. Any ambiguity from the imaging contrast in this transition zone is further removed by the corresponding NBED pattern obtained from the transition region ②, as shown in Figure 4.11d. The diffraction spots corresponding to the alternating arrangement of TM and Li layers (marked with yellow arrows) become weaker as compared to the bulk phase DP, indicating that the structure has lost some of the alternate ordering between the TM and Li layers to a certain extent due to the partial occupancy of the Li sites by TM ions. This observation is again in agreement with the gradual reduction of TM valence mentioned before (Figure 4.9d).

As discussed above, the surface reduction is associated with a phase transition of the layered structure ($R\bar{3}m$) to the TMO rock-salt structure ($Fm\bar{3}m$) accompanied by lithium and oxygen loss. Based on our results, the surface reduction initiates as early as the first-charge process, the formation of the surface layer may impede Li insertion during discharge, resulting in first-cycle coulombic inefficiency. Besides, the surface undergoes more severe phase transformation when the cell is under longer term cycling. It is apparent that the formation and thickening of the TMO rock-salt phase, which has poor electronic and ionic conductivity, could block the lithium pathway and restrict the charge transfer characteristics of the active particles. This may result in an impedance rise at the electrode/electrolyte interface and contribute to the capacity fade.

It is important to note that the thickness of the RS layer varies significantly even within the same grain, as show in Figure 4.13. It was suggested from a previous study that the thickness of the surface reconstruction layer is orientation-dependent,[40] the reconstruction layer is thicker along the Li diffusion channels (i.e. parallel to Li layers) than other orientations. However, this proposed mechanism is insufficient to explain our results. Figure 4.13b and 4.13c show two HAADF-STEM images acquired at different locations from a single grain marked in Figure 4.13a. The phase shown in medium gray is the binder phase that contains conducting carbon. As can be seen from the images that the RS layer in Figure 4.13b is much thinner than the RS layer in Figure 4.13c. The surface RS layer with very different thickness is observed in the same orientation along the Li diffusion channels. Therefore, the crystallographic orientation is not the dominant factor in this case. Instead, we note that the two regions are under different levels of electrolyte exposure. As can be seen in Figure 4.13a, region 1 is tightly bound with the binder matrix while region 2 lacks binder contact and is more likely to be fully exposed to the electrolyte (the pore space in the cathode would presumably be filled with electrolyte during cycling).

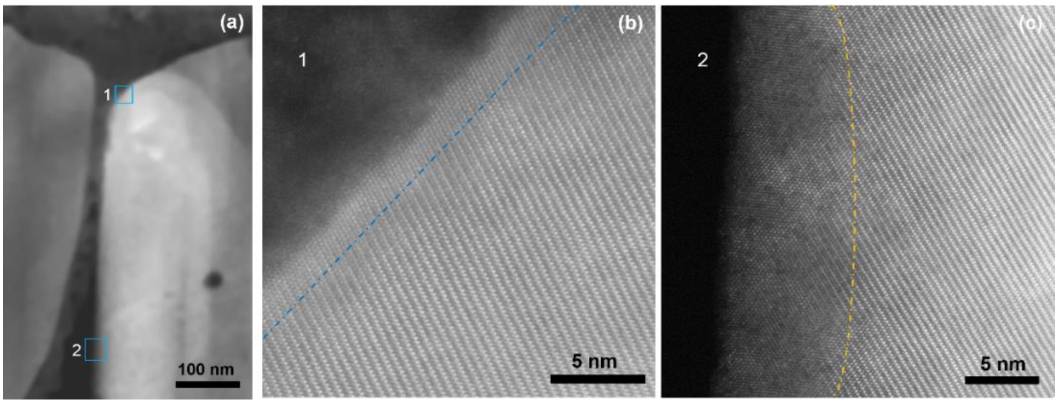

Figure 4.13 HAADF-STEM images of NMC cathode after 50 cycles. (b, c) Atomic-resolution HAADF-STEM images showing the surface reconstruction layer taken at different locations from the same grain, the corresponding locations are marked in (a).

On one hand, the electrode/electrolyte interface reactions, i.e. electrolyte oxidation and decomposition, during electrochemical cycling will highly influence the NMC particle surface. On the other hand, our results show that a thin reconstruction layer is readily formed on the surface of an NMC particle just after pure electrolyte exposure (Figure 4.14). This observation illustrates that the influence of the electrolyte exposure on the active material is not negligible, and can lead to a structural change of the particle surface even without electrochemical cycling. Therefore, the active material/electrolyte contact may also play a role in the surface structural transformation during cycling. The results suggest that a better binder/particle contact could help limiting the structural degradation of the cathode material.

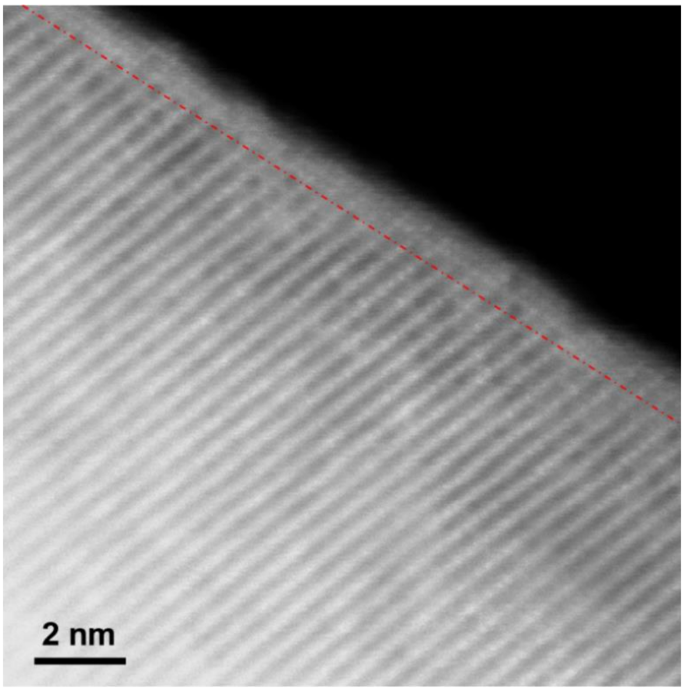

Figure 4.14 Atomic-resolution HAADF-STEM image of a NMC particle after one week electrolyte exposure. The TM migration into Li layer is readily observed near the particle surface.

4.5 Conclusion

A detailed investigation of chemical evolution and structural transformation of stoichiometric NMC cathode material has been carried out upon electrochemical cycling. EELS analysis demonstrates that the charge compensation at TM sites during delithiation is mainly achieved by oxidation of $Ni^{2+}\rightarrow Ni^{4+}$, whereas $Co^{3+}$and Mn^{4+} remain essentially unchanged. The ^{7}Li NMR study of NMC at high voltage resolves distinct environments, definitively proving local ordering of Mn^{4+} and Ni^{2+} in the TM layer. The relithiated spectrum of 2.5 V NMC is almost identical to that of pristine NMC, which demonstrates the reversible nature of Li extraction-insertion in bulk NMC. The structure, including the local Mn^{4+}/Ni^{2+} ordering, is stable, as reflected by unchanged ^{7}Li spectra collected at 4.6 V after the first and tenth electrochemical cycles.

In contrast to the bulk measurement of NMR, spatially resolved STEM-EELS results show that the electronic structure of TM cations are inhomogeneous from the particle surface to the bulk upon first-charge. A surface reduction layer is formed at the surface, where the TMs are in lower oxidation state near the particle surface compared to the bulk. Our results indicate that the surface evolution of NMC originates in the first cycle. It is shown that the surface region of NMC has transformed to a TMO-type rock-salt (RS) phase (transition from $R\bar{3}m$ to $Fm\bar{3}m$) accompanied by lithium and oxygen loss during cycling, while a partially disordered layered structure is located between the bulk and the surface RS layer as a transition zone. The formation of this poor electronic and ionic conductive TMO layer would limit the charge transfer of the cathode and adversely impact the cell capacity. It is also worth noting that electrolyte exposure has influence on the surface structural change whereas a better binder/particle contact may help limiting the structural degradation of the cathode. This work clarifies the role of TM cations in the charge compensation process and unravels the initiation and development of cathode degradation process, providing valuable insights into the origins of battery performance deterioration.

Chapter 5

Structural and Chemical Analysis of $Li_{1.2}Ni_{0.13}Mn_{0.54}Co_{0.13}O_2$ Cathode Material

Compared to the commercial layered NMC cathode material that has been discussed in the previous chapter, lithium-rich layered oxides are promising cathode candidates for the next generation lithium-ion batteries which possess higher specific energy density. The Li-rich cathodes can provide high capacity of above 250 mAh/g under high operation voltage, whereas they suffer severe capacity loss and voltage decay during cycling that hinder their commercial applications. Although different modification methods have been developed to improve the cycling performance of Li-rich cathodes, the premise for the improvement is an in-depth understanding of the reasons behind the performance deterioration. Under such circumstances, the exploration of the origin for the rapid performance decay of Li-rich cathodes is of paramount importance for the future application of these high-energy cathode materials. In this chapter, we implement aberration-corrected Scanning Transmission Electron Microscopy (STEM), Electron Energy Loss Spectroscopy (EELS), ^{7}Li Nuclear Magnetic Resonance (pj-MATPASS, NMR)† and X-Ray Diffraction (XRD) to thoroughly investigate the structural and chemical evolution of high-energy $Li_{1.2}Ni_{0.13}Mn_{0.54}Co_{0.13}O_2$ (HENMC) layered cathode material, aiming to unravel the origins for the rapid performance decay of Li-rich cathode material.

---

† The NMR measurements and analysis were carried out by *Matteo Z. Tessaro*, and *Kristopher J. Harris* from Gillian Goward's group at McMaster University

5.1 Sample Preparation and Characterization Techniques

5.1.1 Electrochemical Test

The lab-scale $Li_{1.2}Ni_{0.13}Mn_{0.56}Co_{0.13}O_2$ (HENMC) cathode material was synthesized using the co-precipitation method.† The transition metal acetates: $Ni(CH_3CO_2)_2 \cdot xH_2O$ (99+%, Alfa Aesar), $Mn(CH_3CO_2)_2 \cdot xH_2O$ (99+%, Arcros Organics), and $Co(CH_3CO_2)_2 \cdot xH_2O$ (99+%, Alfa Aesar) were dissolved in de-ionized water and added to a solution of KOH (0.1M) to form the mixed transition metal hydroxide precipitate. The precipitate was filtered and washed with de-ionized water to remove the residual KOH and then dried overnight at 100°C. The dried product was mixed with a 3% excess lithium hydroxide and heated for 24 hours in air at 900 ˚C. The cathode was prepared with HENMC powder, acetylene black and polyvinylidene fluoride (PVDF) at a weight % ratio of 80:10:10. The cathodes were then constructed into half-cell configurations with Li metal as counter electrode and 1M $LiPF_6$ EC/DMC (1:2-v/v) as electrolyte. The coin cells were cycled galvanostatically between 2.0-4.6 V at rates of C/10 using a Maccor cycler. The cyclic curves are shown in Figure 5.1.

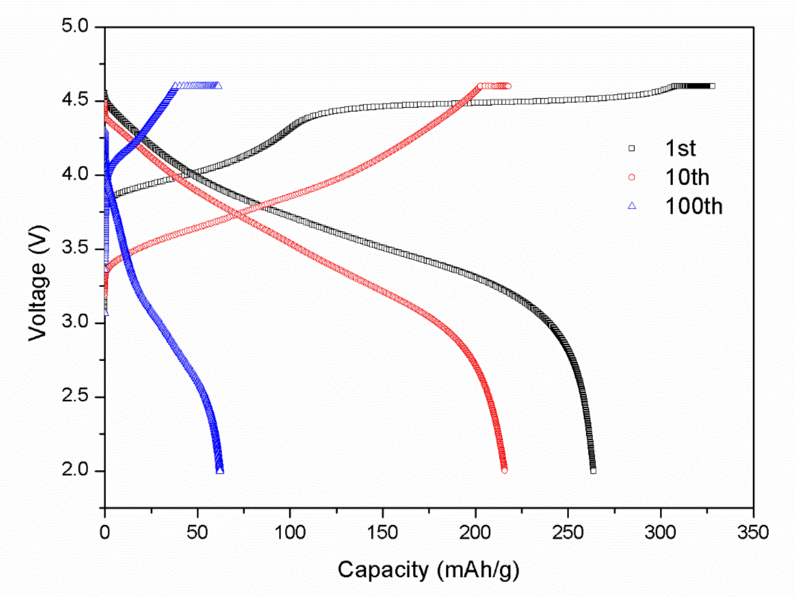

Figure 5.1 Charge and discharge profiles of HENMC after 1, 10 and 100 cycles.

---

† The HENMC was synthesized and provided by *Yan Wu* and *Meng Jiang* from General Motors.

5.1.2 Transmission Electron Microscopy Characterization

The pristine and cycled HENMC samples were studied using an aberration-corrected (probe and image-forming lenses) FEI Titan Cubed 80-300 kV microscope operated at 200 kV. For structural analysis, STEM images were acquired using a high-angle annular dark-field (HAADF) detector with collection angle range of 64-200 mrad. The HAADF-STEM image provides “Z-contrast” imaging, where the image intensity is proportional to the atomic number of the elements present in the material. For chemical analysis, EELS data were recorded using a Gatan Image Filter (GIF) Quantum-965 with 0.25 eV/channel dispersion of the spectrometer. To prepare the TEM specimen for pristine HENMC, the powder was dispersed in ethanol and drop casting to a copper grid. The TEM specimens for cycled cathodes were prepared using a dual beam focused ion beam-scanning electron microscope (FIB-SEM, Zeiss NVision 40). The cells were discharged to 2.0 V, disassembled and dried in a glove box before TEM specimen preparation.

5.1.3 XRD and NMR Spectroscopy

The XRD data was collected by a Bruker Smart6000 CCD area detector with a Rigaku Cu Kα (λ=1.5418 Å) rotating anode source operating at 50 kV voltage and 90 mA current. ^{7}Li NMR spectra were acquired under a 4.7 T applied magnetic field using a Bruker DRX console and are referenced to 1M $LiCl_{(aq)}$ at 0 ppm. In all cases, 1.5 μs $\pi/2$ pulses and 100 ms delays were employed. ^{7}Li NMR spectra influenced only by the isotropic chemical shifts were recorded using either the MAT (magic-angle-turning) or pj-MATPASS (projection magic-angle-turning phase-alternating spinning-sideband) methods.[168] The MAT spectrum of the 50-cycle sample used a 34 kHz sample spinning rate and a home-built probe employing 1.8 mm rotors, while all other experiments used pj-MATPASS experiments under a 60 kHz sample-spinning rate with a Bruker high speed MAS probe and 1.3 mm rotors.

5.2 Characterization of Pristine HENMC

The pristine HENMC cathode material was examined using multiple techniques in order to clarify the structure and composition of the material, and to enable a better understanding of the material's behavior during the subsequent electrochemical cycling. Figure 5.2a shows the powder XRD pattern of pristine HENMC. The majority of diffraction peaks can be indexed to the trigonal ($R\bar{3}m$) structure, except the weak peaks at lower 2Θ angles (between 20° and 25°). The appearance of the superstructure reflections at lower angles is attributed to the "honeycomb" cation ordering of Li-TM (transition metal) atoms in the TM layer, which is characteristic of the monoclinic (*C2/m*) phase. An obvious broadening of the (020) and (110) superstructure peaks is observed in Figure 5.2a. According to previous studies, this broadening may be due to stacking faults of the cationic layers along the monoclinic c-axis.[179,180] Daniel et al.[124] reported that the structure of the Li-rich cathode material can be refined with both (i) a monoclinic (*C2/m* space group) only model, where Mn, Co and Ni are all allowed to occupy both the 2b (Li in the TM layer) and 4g (Mn in the TM layer) sites; and (ii) a monoclinic (*C2/m*) Li_2MnO_3 + trigonal ($R\bar{3}m$) two-phase mixture model, where only Mn is allowed in the 4g site of the monoclinic phase. They show that both models fit well with the neutron diffraction results. In such case, the diffraction data is inconclusive to determine whether the material is a solid solution or a two-phase composite.

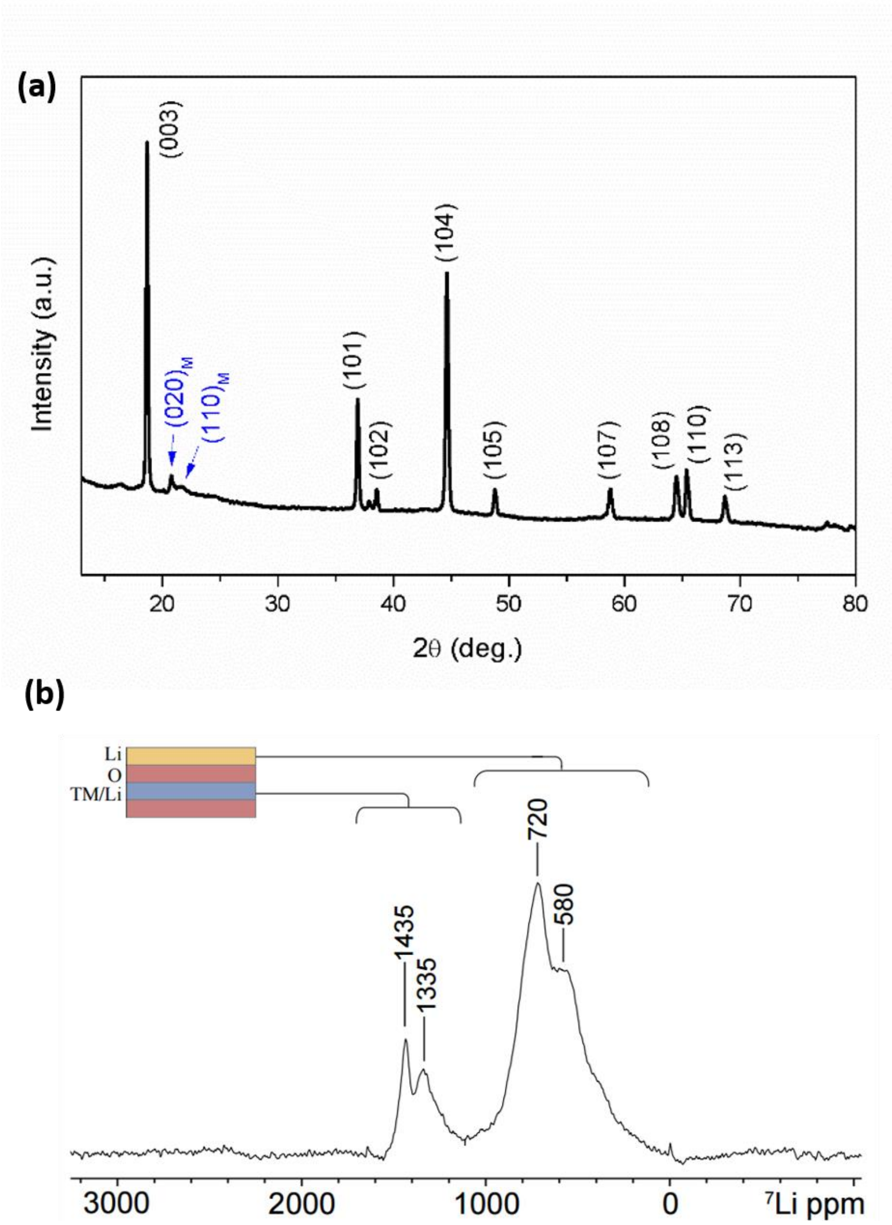

Figure 5.2 Characterization of pristine HENMC cathode material. (a) XRD pattern.(b) ^{7}Li MATPASS NMR spectrum. Inset: layered structure of the material showing peak assignments by layer type.

Solid-state NMR spectroscopy is well known for its ability to report on local structures within fully or partially disordered materials, and ^{7}Li NMR analysis is relatively well established in this class of material.[36,65,173,181–183] As discussed in our submitted manuscript and summarized here, the ^{7}Li NMR spectrum of pristine HENMC (Figure 5.2b) displays two distinct groupings of resonances: Li in the Li layer at 0 to ~1100 ppm, and Li in the nominally TM layer at ~1100 to 1600 ppm.[65,173] Of particular note is that the frequencies of the two largest peaks (1435 ppm and 720 ppm) correspond essentially exactly to those observed from the pure monoclinic-phase Li_2MnO_3. This suggests that much of the structure is not too different from this parent phase.

The ^{7}Li NMR peaks at 1435 ppm and 1335 ppm arise from the Li in the TM layers. As mentioned before, the 1435 ppm peak corresponds to the $LiMn_6$ local ordering in the TM layer from the Li_2MnO_3 phase. While the nearest-neighbor Mn contributes a positive frequency shift, Ni contributes a negative shift, and Co and Ni produce no effect, the other peak located at 1335 ppm is most probably due to the $LiMn_5Co$ or $LiMn_5Ni$ local ordering in pristine HENMC. The peaks below 1100 ppm originate from Li in the Li layer, the different configurations of TM atoms lying in layers on either side of each Li give rise to a series of peaks. The largest peak in the HENMC spectrum at 720 ppm is a measure of the large amount of Li environments that are between TM-sheet sections that are nominally similar to the Li layer in Li_2MnO_3. Since Mn contributes the largest positive frequency shift, it is likely that the signal intensity at frequencies below 720 ppm is from environments in which some of the Mn positions in the $LiMn_6$ local ordering are swapped for Co or Ni.†

More spatially-resolved structural and chemical information of the HENMC cathode material were obtained by aberration-corrected STEM and EELS characterization. Figure 5.3a shows a HAADF-STEM image of pristine HENMC, the bright atomic columns correspond to the TM atoms, while the lighter elements Li and O are not visible from the image due to their low atomic weights. As can be seen from the image, projections of $[110]_M$, $[1\text{-}10]_M$, and $[100]_M$ zone axes of the *C2/m* monoclinic phase are co-existing in the bulk region due to stacking faults along the c-axis, as labelled in the image with different colored frames. The corresponding atomic models of these three orientations are presented in Figure 5.3b. The observation of stacking fault in the pristine material is in accordance with the broadening of superstructure

---

† More detailed analysis of NMR spectrum is discussed in the submitted manuscript.

peaks in the XRD pattern in Figure 5.2b. The HAADF-STEM intensity plot of the TM layer is shown in Figure 5.3c, in which the two adjacent bright TM atomic columns are separated by 0.14 nm spacing, forming a TM-TM dumbbell, and the dark Li atomic columns reside between these TM dumbbells. Crucially, this Li-TM ordering in the TM layer is unique to the monoclinic phase and is not present in any orientations of the trigonal phase.

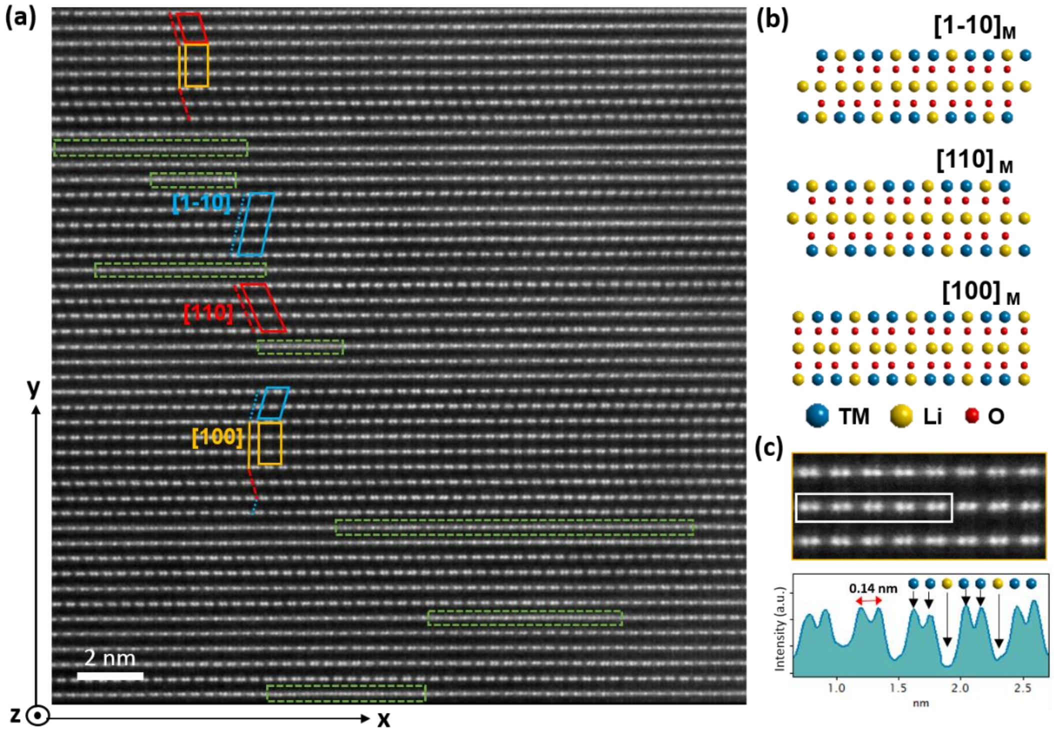

Figure 5.3 HAADF-STEM image taken from pristine HENMC sample. (a) The HAADF image shows the monoclinic domains of HENMC. The Z direction comes out of the page. (b) Atomic models of the monoclinic structure in $[1\bar{1}0]$, [110], [100] orientations. (c) Intensity plot from the region highlighted with the white rectangle in the HAADF image. The subscript M denotes the monoclinic *C2/m* structure.

It can be seen from the image that there are some lattice planes exhibiting continuous contrast instead of the TM dumbbell ordering (marked with green dotted rectangles). This effect has also been observed in a previous study, where it was suggested to be due to the presence of a LiMO$_2$ trigonal phase.[128] Through detailed analysis on the intensity of the continuous planes, we notice that there is no significant change in the contrast of the continuous plane when compared with the adjacent planes containing the dumbbells as illustrated in the intensity plot shown in Figure 5.4a. However, the expected intensity of a $LiMO_2$ type plane should be about twice as that of a Li_2MnO_3-like monoclinic phase, because the larger number of heavier TM atoms in the $LiMO_2$ lattice plane would lead to a higher contrast in the HAADF image. Thus, it is believed that such effects are due to the presence of stacking faults within the projected particle thickness (as illustrated in Figure 5.4b), similar to the ones seen in the X,Y plane of Figure 5.3a. Therefore, the presence of these partial planes with continuous contrast could be due to the stacking faults in the Z direction of the sample, as illustrated in Figure 5.4b.

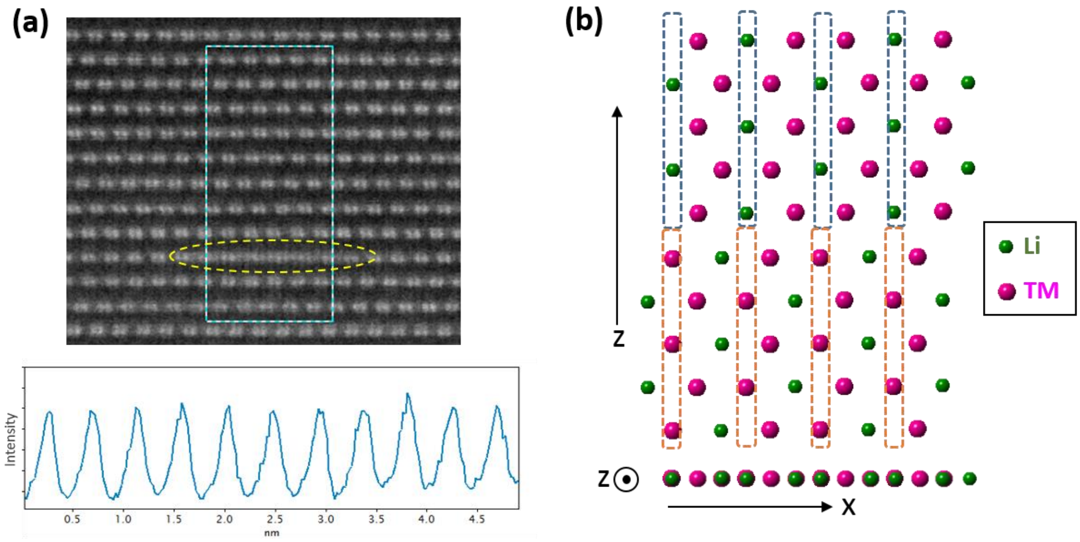

Figure 5.4 (a) Intensity plot of the lattice planes from the highlighted region in the STEM image of pristine HENMC. The continuous plane is marked with a yellow dotted circle. (b) Atomic model illustrating the continuous contrast leading by the stacking faults in the depth (z) direction. The point within a circle next to the “Z” letter indicates that the Z direction comes out of the page.

The EELS spectra taken from the monoclinic domains confirms the presence of the three TM elements. Figure 5.5 shows an EELS spectrum taken from the monoclinic region where the “dumbbell” structure is visible. Mn, Co and Ni $L_{2,3}$-edges are clearly observed from the spectrum with the oxidation state of 4+, 3+ and 2+ respectively, indicating the monoclinic domains are not Li_2MnO_3 phase since the three TM cations are co-existing. It is possible, however, that small amounts of Ni are in the TM-layer

Li sites (shown as the dark atomic column between the TM dumbbells), because the intensity variation could be negligible or minor when replacing the Li by Ni with less than 20%, as demonstrated from STEM image simulation by Gu et al.[184].

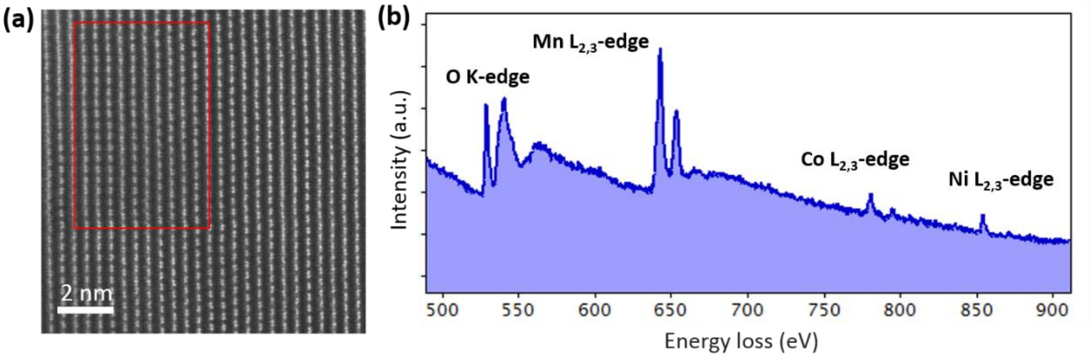

Figure 5.5 (a) HAADF-STEM image acquired from the region exhibiting the TM dumbbell structures in pristine HENMC. (b) EELS spectrum acquired from the region marked in (a).

By examining multiple particles, the three TMs always co-exist throughout the bulk material with no abrupt changes in the concentration between different grains. Figure 5.6a shows the HAADF-STEM image across two grains from pristine HENMC. The top grain shows the honeycomb ordering that is characteristic of the monoclinic ordering, while the bottom grain shows the well-defined layers. The crystallographic structure of the two grains are confirmed by the corresponding Fourier Transform (FT) diffractograms shown in Figure 5.6b and c. The diffractogram acquired from the top grain shows the super-lattice diffraction spots that can only be indexed to the *C2/m* monoclinic phase rather than the $R\overline{3}m$ trigonal phase. Meanwhile, the diffractogram acquired from the bottom grain can be indexed to both phases, as shown in Figure 5.6c. Therefore, if the bottom layered ordering grain belongs to the $LiMO_2$ trigonal phase, and the material is a two-phase composite, a change in the composition of the two grains would be expected. EELS spectra were obtained across the two grains in order to further examine if there is any chemical variation, as shown in Figure 5.6d. As can be seen from the EELS spectra, there is no discernible change in the composition across the two grains.

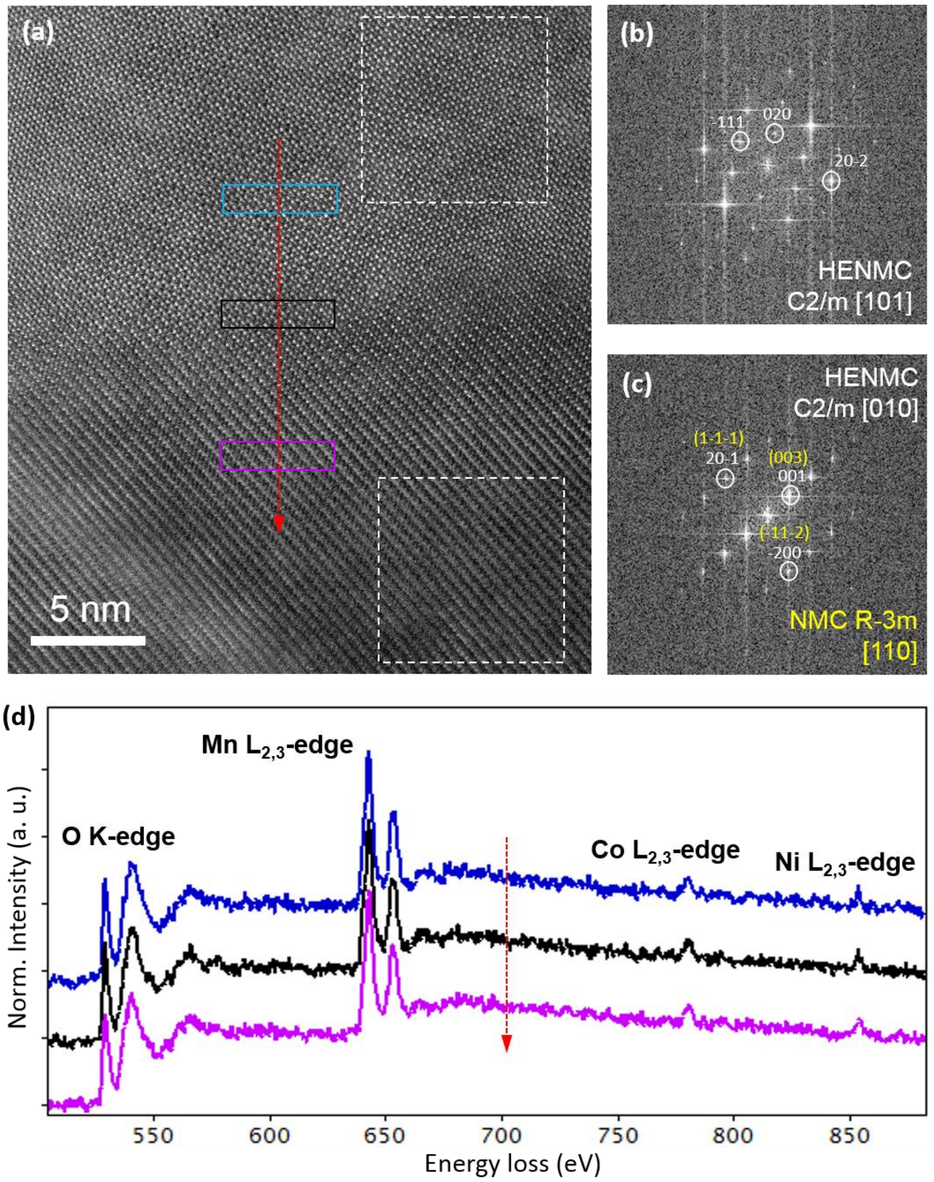

Figure 5.6 (a) HAADF-STEM image acquired from two adjacent grains of pristine HENMC. (b, c) Fourier Transform (FT) diffractograms of the areas marked in (a). (d) Series of EELS spectra acquired across the two grains shown in (a).

These findings are in apparent contradiction with the two-phase composite (Li_2MnO_3 + $LiMO_2$) model, in which Mn segregation would be expected in the monoclinic domains. The result, therefore, suggests that the structure of HENMC cathode material is most accurately described as a solid-solution based on monoclinic symmetry.

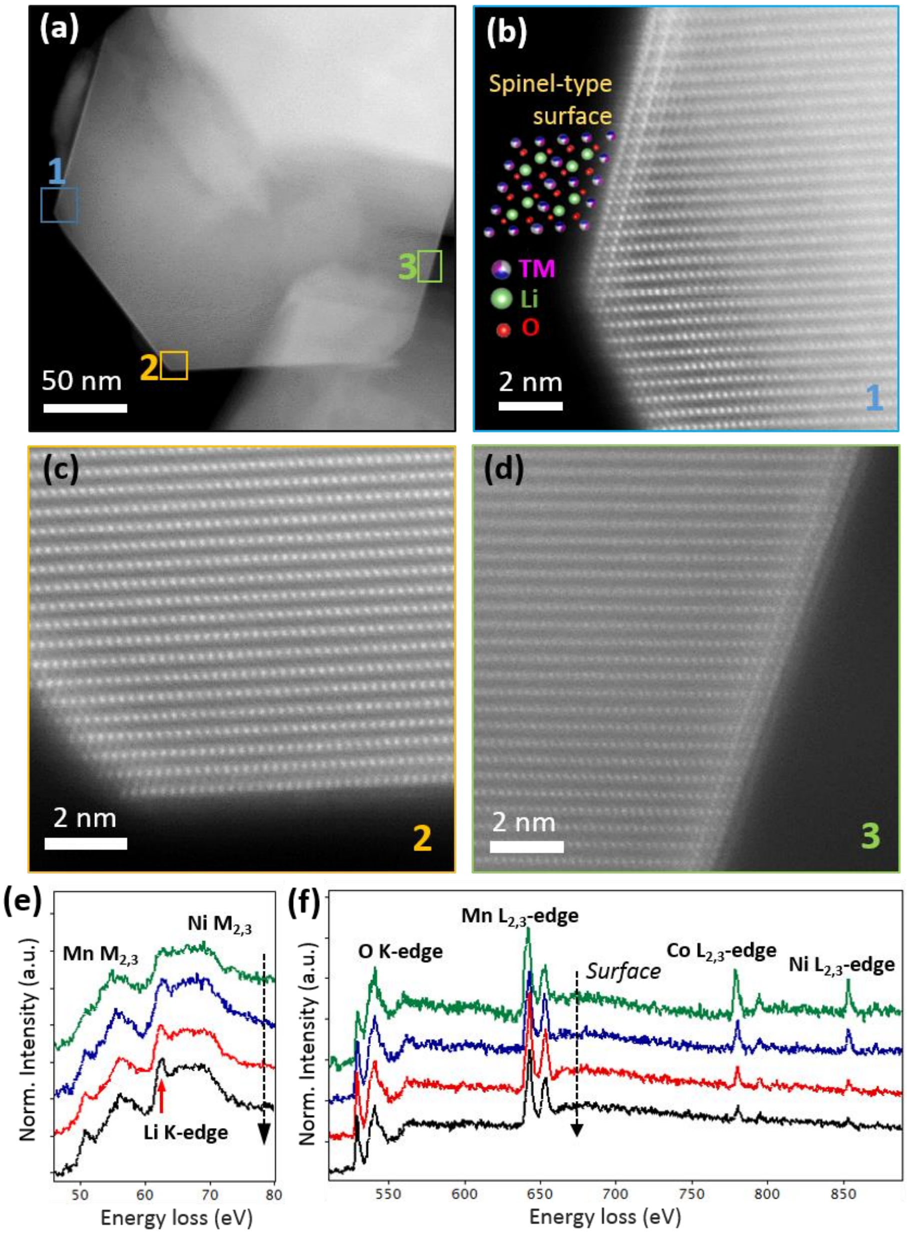

Figure 5.7 (a) A lower magnification HAADF-STEM image of pristine HENMC. (b-d) Atomic-resolution HAADF-STEM images acquired from different facets of a HENMC particle as indicated in (a). (e, f) Series of EELS spectra showing the spinel-type surface and bulk corresponding to the image in (b). Note that the Co $M_{2,3}$-edge is not labelled in the spectra since the edge onset of Co $M_{2,3}$-edge is close to Li K-edge at a slightly higher energy loss. The Co $M_{2,3}$-edge has a very broad peak feature, which is usually hidden under the sharp Li K-edge features.

Structural differences between the bulk region of the particles and their surfaces are observed in pristine HENMC. Figure 5.7 shows the atomic-resolution HAADF-STEM images taken from different regions of a pristine HENMC particle, as indicated in the lower magnification image shown in Figure 5.7a. The particle surface has a distinct atomic ordering that is different from the bulk structure (Figure 5.7b). This surface layer is about 2 unit cell thick and can be indexed to the $[110]_S$ zone axis of an $Fd\bar{3}m$ spinel phase, and the corresponding atomic model is shown on the left inset of Figure 5.7b. This spinel-type surface termination is also present in other surface regions of the particle with the thickness around 1-2 unit cells (Figure 5.7d). It is also noticed that these spinel surface layers are mostly present on (100) facets of the particles, which are formed along the Li-O-TM layers. EELS spectra demonstrate that the intensity of Li K-edge is reduced in the surface spinel layer (Figure 5.7e), while the relative intensities of Co and Ni $L_{2,3}$-edges to Mn $L_{2,3}$-edges increase dramatically from the particle bulk to the surface (Figure 5.7f), indicating that there is Co and Ni segregation at the spinel surface. Moreover, the spinel-type surface is usually present on a single facet and does not continue onto neighboring ones (Figure 5.7b). It is important to note that the spinel phase is not detected from the powder XRD pattern, which may because the small size of the spinel layer will lead to very broad diffraction peaks according to Scherrer equation and the spinel phase in the pristine material is a very small portion of the overall cathode materials, so that any resulting features in the patterns are below the detection limit.

There are also some spinel-like regions observed at grain boundaries in the bulk material, as shown in Figure 5.8a. However, EELS analysis across this grain boundary presents no discernible change in the intensity of Li K-edge (Figure 5.8c), which indicates that the Li concentration at the grain boundary and the two adjacent grains is quite uniform. Meanwhile, the relative intensity between O K-edge and Mn, Co, Ni $L_{2,3}$-edges exhibits no significant change across grain boundary (Figure 5.8d), suggesting there is no TM segregation at the grain boundary. As discussed above, some degree of TM segregation would be expected from the spinel phase considering the O:TM ratio varies between HENMC phase (2.5) and spinel phase (2.0). The absence of a compositional change at the boundary suggests that instead of the spinel phase, we observed the overlap of the two adjacent layered grains, as illustrated in Figure 5.8b, which can exhibit this misleading atomic-arrangement when the edge of the two grains overlapped with each other.

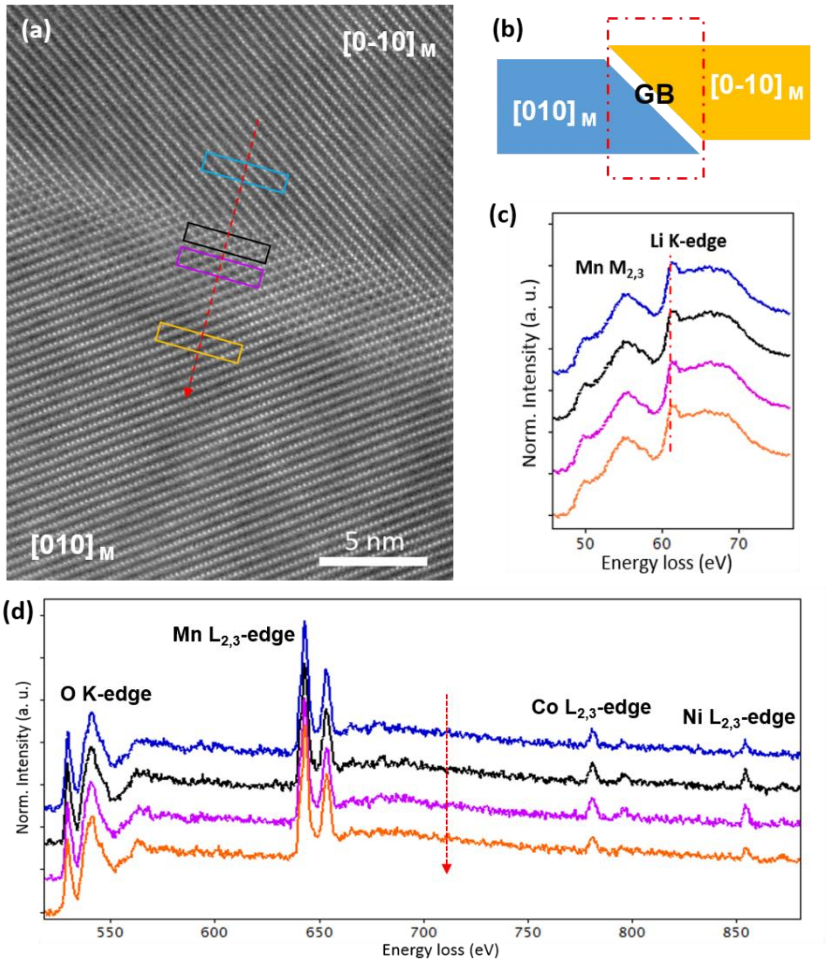

Figure 5.8 (a) HAADF-STEM image showing the spinel-like region at the grain boundary of HENMC. (b) Schematic of the two overlapped grains. GB denotes for grain boundary. (c, d) Series of EELS spectra obtained across the grain boundary shown in (a).

Besides the regions with a spinel surface layer, the majority of surface areas maintain the layered structure as the bulk region. As shown in Figure 5.7c, the particle surface maintains the layered structure as the bulk region in both facets. Although no structural variation is observed from these facets, EELS spectra acquired from these surfaces show interesting differences with the bulk in some areas. The compositional variation from the layered particle surface to the bulk is clearly illustrated in Figure 5.9. The EELS maps (Figure 5.9b and 5.9c) show that the particle surface exhibits significant Co segregation even though the surface has an apparent identical layered structure with bulk. The EELS spectra (Figure 5.9d) clearly show that the relative intensity of Co $L_{2,3}$- to Mn $L_{2,3}$-edges increases dramatically from bulk to the outer surface atomic planes, suggesting the increased concentration of Co at surface. We also note that the O K edge does not present any fine changes, indicating that this Co enhancement does not lead to significant structural changes or oxygen loss.

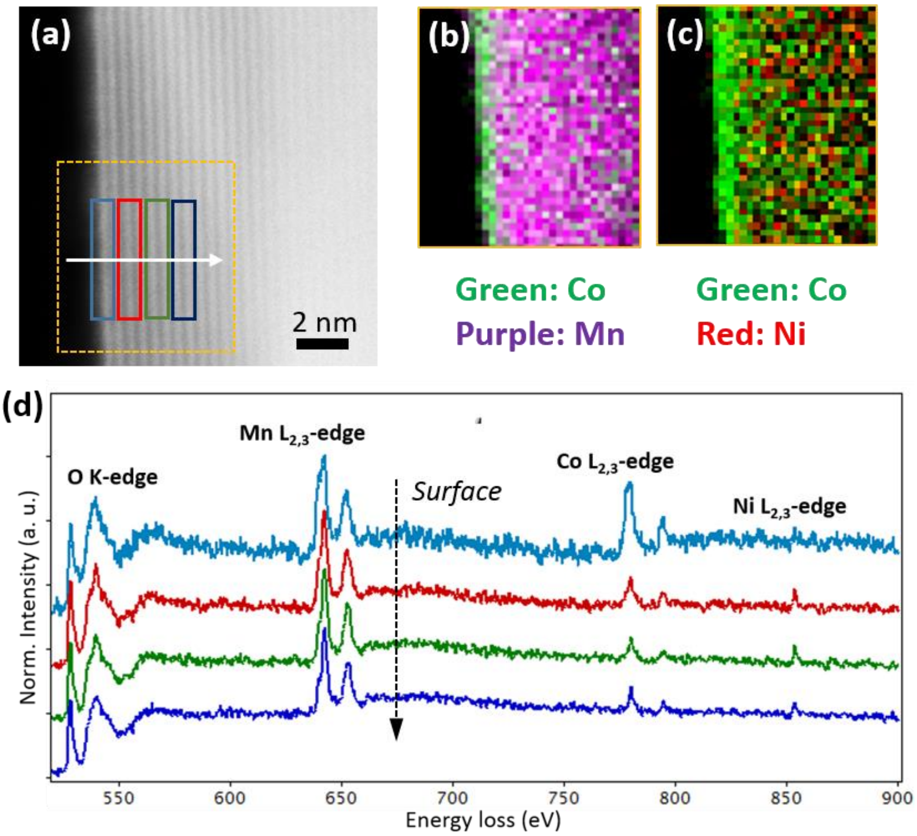

Figure 5.9 (a) HAADF-STEM image of pristine HENMC. (b) Elemental map of Co and Mn. (c) Elemental map of Co and Ni. (d) A series of EELS spectra acquired form the particle surface to bulk indicated in (a).

5.3 Structural and Chemical Evolution at HENMC Surface

5.3.1 Formation of Surface Reconstruction Layer

The surface evolution of HENMC cathode during cycling was investigated using electron microscopy (EM). Figure 5.10 shows the edges of differently cycled HENMC particles. The HAADF-STEM images of HENMC after 1 cycle are shown in Figure 5.10a-5.10c. The bulk regions of the 1-cycle particles maintain the layered structure, whereas the first few atomic planes near the surface exhibit obvious difference as compared to the bulk (Figure 5.10a-5.10c). Most surface areas suffer TM migration into Li octahedral sites, forming a rock-salt like structure within a thickness of about 1.5-2.5 nm, indicating that the HENMC particles have undergone surface structural evolution during the first cycle. Meanwhile, a surface layer with spinel structure is also observed from a few surface areas as shown in Figure 5.10b. We cannot conclude that the spinel phase detected on the surface of 1-cycle HENMC must be formed during cycling, since the pristine HENMC already contains spinel surface layers on certain facets (shown in Figure 5.7), it is possible that those spinel layers are stable during cycling and still present after the first cycle.

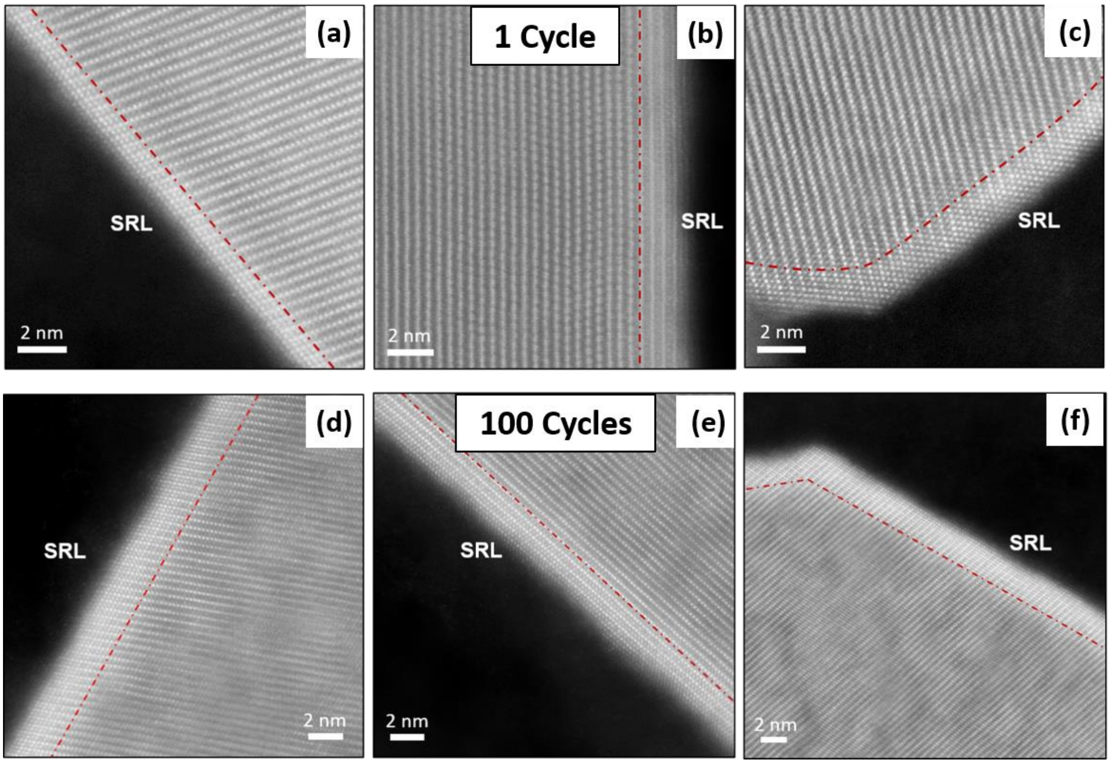

Figure 5.10 HAADF-STEM images of cycled HENMC particles after: (a-c) 1 cycle; (d-e) 100 cycles.

Furthermore, the formation of the surface reconstruction layer (SRL) during electrochemical cycling is accompanied with irreversible Li loss as illustrated in the Li

K-edge spectra shown in Figure 5.11a, where the sharp Li K-edge feature almost disappears at the surface layer with only the broad Co $M_{2,3}$-edge visible in the spectra. The TMs are also reduced to lower oxidation states as indicated by the chemical shift of Mn and Co $L_{2,3}$-edges towards lower energy and the increase in the intensity ratio of L_3/L_2 peaks (Figure 5.11b).The O K-edge at SRL is dramatically different with the bulk region, indicating a change of oxygen environment at SRL, consistent with the rock-salt formation that has been observed in previous studies on the layered lithium transition metal oxide cathode materials.[36,152,185] The formation of the SRL in Li-rich cathode material could be related to oxygen removal associated with Li extraction at the 4.5 V plateau during the first charge[69,136,139]. In fact, the EELS spectra also reveals that the O to TM ratio is significantly decreased at SRL as compared to the bulk region.

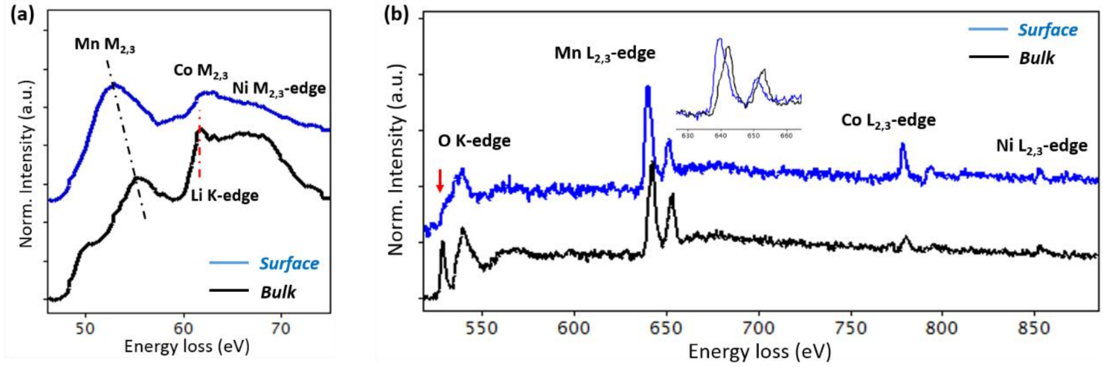

Figure 5.11 EELS spectra acquired from the SRL and bulk region of 1-cycle HENMC. (a) Low-loss spectra. (b) Core-loss spectra.

Figure 5.10d-5.10f present HAADF-STEM images of HENMC after 100 electrochemical cycles. The thickness of the SRLs from 100-cycles particles is around 2-4 nm, i.e. not significantly increased compared to the 1-cycle sample. The formation of SRLs on layered structure cathode materials is often correlated with the first-cycle irreversible capacity loss and the performance decay of the battery.[40,106,146] Although the SRL could be thicker (~10 nm) in some surface regions, the structural change at HENMC particle surfaces is only a small portion of the whole cathode material; this surface effect cannot fully explain the significant voltage decay and capacity loss of the HENMC cell (shown from the charge/discharge curves in Figure 5.1).

5.3.2 Formation of Cathode-Electrolyte Interface Layer

A further observation related to the formation of surface passivation layer on the cathode/electrolyte interface demonstrated in Figure 5.12a and 5.12b. An amorphous layer, with non-uniform distribution is detected on the 100-cycle HENMC particle surface. The thickness of this amorphous layer, not observed in the pristine material, is up to about 20-30 nm in some regions of the HENMC particles. It has been reported that the undesired side reactions can take place near the surface of a cathode particle, where electrolyte solvent and salt can participate in electrochemical reactions, and form a SEI-type layer on the cathode/electrolyte interface (CEI).[97] The composition of this CEI layer has been investigated using EELS. Figure 5.12d shows a series of EELS spectra obtained from regions at the surface layer and then moving into the particle bulk.

First of all, a significant amount of oxygen is detected in the CEI layer as evidenced by the intense O K-edge in the EELS spectra acquired from the surface layer. The shape of the O K-edge fine structure is also very different with respect to the bulk. The O K-edge acquired from bulk region has a pre-peak located at ~ 530 eV which is attributed to the transition of O *1s* core state to O *2p* unoccupied states. Because the O *2p* states are highly hybridized with TM *3d* states, the intensity change of the O K-edge pre-peak will reflect the variation of TM oxidation states. The intensity of the O K-edge pre-peak drops significantly when approaching the particle surface, indicating that the TM cations are in lower oxidation states near the particle surface. Moreover, the O K-edge fine structure is fully changed when probing into the CEI layer, indicating the coordination environment of the oxygen atoms has drastically changed at the surface layer.

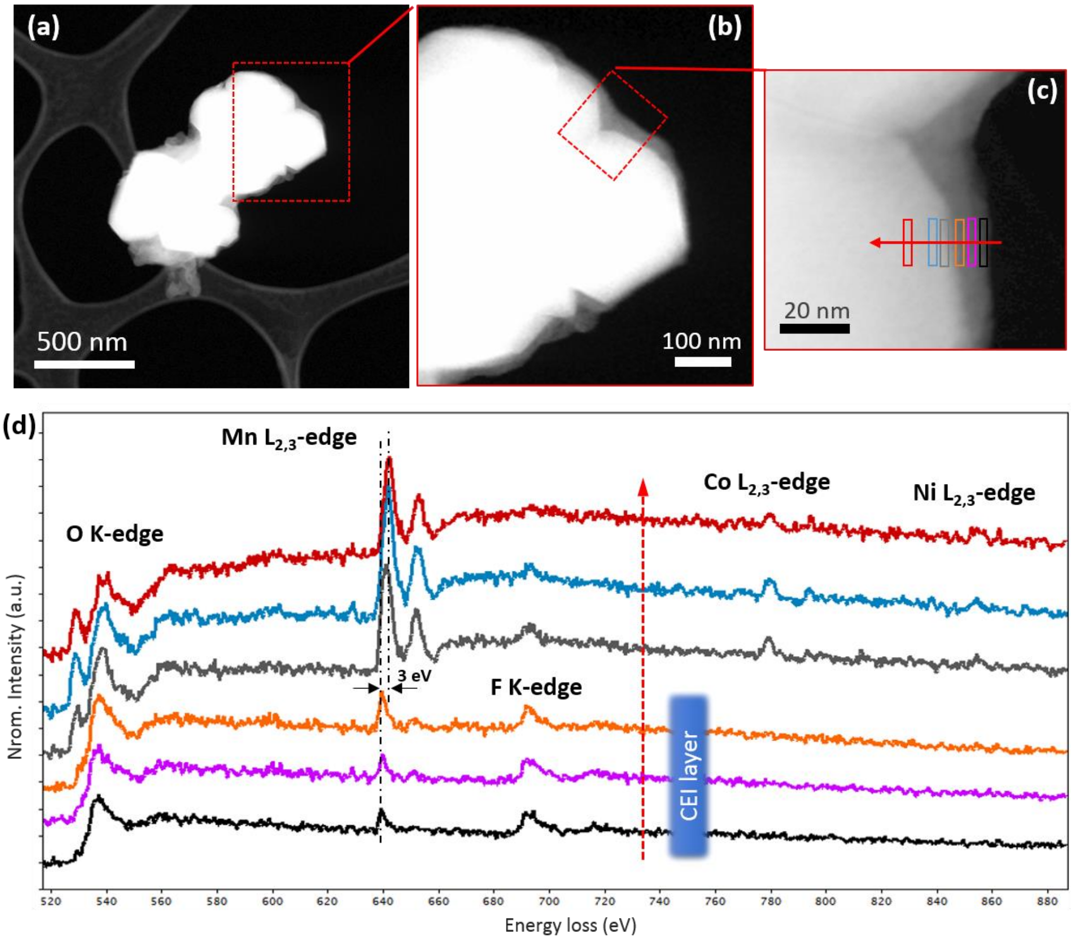

Figure 5.12 (a, b) HAADF-STEM images of the HENMC particle after 100 cycles. (c, d) A series of EELS spectra acquired from the CEI layer to the bulk. The spectra were collected from the color coded regions of interest (ROI) marked in (c).

In addition, EELS spectra show that the Mn, Co and Ni are co-existing in the cycled particle, and both Mn and Co have been reduced to lower oxidation states near the particle surface compared to the bulk region, as evidenced by the chemical shift of the $L_{2,3}$-edges towards lower energy. This effect is consistent with the SRL formation discussed above. When probing into the CEI surface layer, however, both Co and Ni $L_{2,3}$-edges disappear whereas Mn $L_{2,3}$-edges are still present. The Mn L_3-edge from the surface layer exhibits about 3 eV chemical shift towards lower energy compared to the bulk spectrum (shown in red), indicating a reduction of Mn^{4+} to Mn^{2+}.[174] The presence of Mn^{2+} in the CEI layer is indicative of Mn dissolution from the HENMC cathode into the electrolyte during electrochemical cycling.

Furthermore, a fluorine K-edge is observed in the EELS spectra collected from the surface (Figure 5.12d), which confirms the presence of F in the CEI layer. Meanwhile, C and Li were also detected from the surface layer, as shown in Figure 5.13. It is worth noting that the peak features of Li K-edge acquired from the CEI layer is quite different from that of the bulk layered phase, which may be due to the overlap of Li K-edge from different possible electrolyte decomposition products, such as LiF, Li_xPF_y, Li_2CO_3, etc.[98] This CEI layer buildup is likely to influence the charge transfer characteristics between cathode and electrolyte and result in impedance rise of the cell.

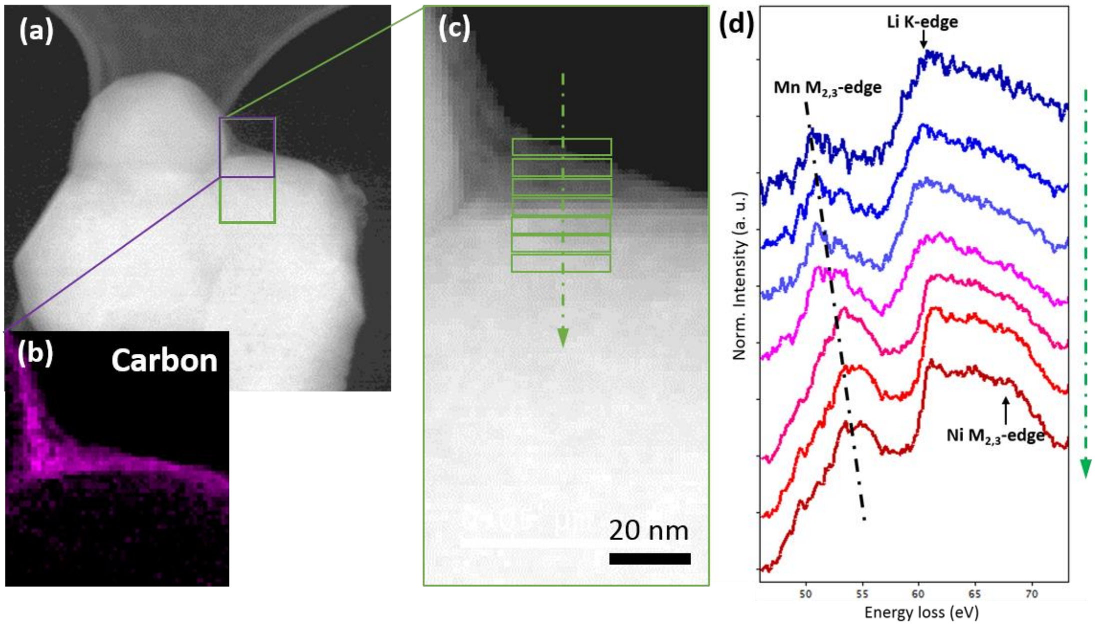

Figure 5.13 (a) HAADF-STEM images of a HENMC particles after 100 cycles. (b) Carbon map from the region marked in (a). (c, d) A series of EELS spectra acquired from the CEI layer to the bulk, as indicated in (c).

5.4 Structural and Chemical Evolution in Bulk Material

5.4.1 Irreversible Li loss and Structural Transformation

While TEM is perfectly suited to study changes in very specific regions on an incredibly small scale, such as the surface reconstruction shown above, solid-state NMR reports on the short range atomic configuration but averaged over the entire material, allowing changes in the bulk properties to be measured. Notably, the small fractional volume of the surface reconstruction layers studied above prevents them from contributing visible signal to the NMR measurements. Studying the spectrum after electrochemical cycling therefore yields averaged information on changes in the local environments around each Li atom.

As discussed in our submitted manuscript and summarized here, the post-cycling NMR spectra demonstrate clearly that the first few cycles yield little change in the local structure; e.g. Figure 5.14a, where the shape of the spectrum changes by little more than an increased line broadening after two cycles. This is perhaps somewhat surprising given the very different electrochemical response of the material during the first cycle versus the subsequent electrochemical cycles. By comparing the intensity ratio of the TM-layer Li resonances with the Li-layer Li resonances from pristine HENMC and 2-cycle HENMC, a decrease in the intensity ratio of the TM-layer Li is detected from HENMC after 2 cycles (from 1:1.209 to 1:1.140), indicating there is Li loss from the TM-layers in the initial few cycles. More drastic changes are observed from the NMR spectrum of HENMC cathode after 50 cycles. Firstly, the NMR peaks representing the Li in TM-layers (located at 1435 ppm and 1335 ppm) are no longer visible, suggesting the excess Li in the TM-layers are fully lost after prolonged electrochemical cycling. In addition, the Li-layer Li peaks become less defined, indicating a loss of order in the long-term cycled material. The ^{7}Li NMR spectrum of 50-cycle HENMC is similar to that of the NMC-based cathode materials,[173,183] as the one we show in the previous chapter.

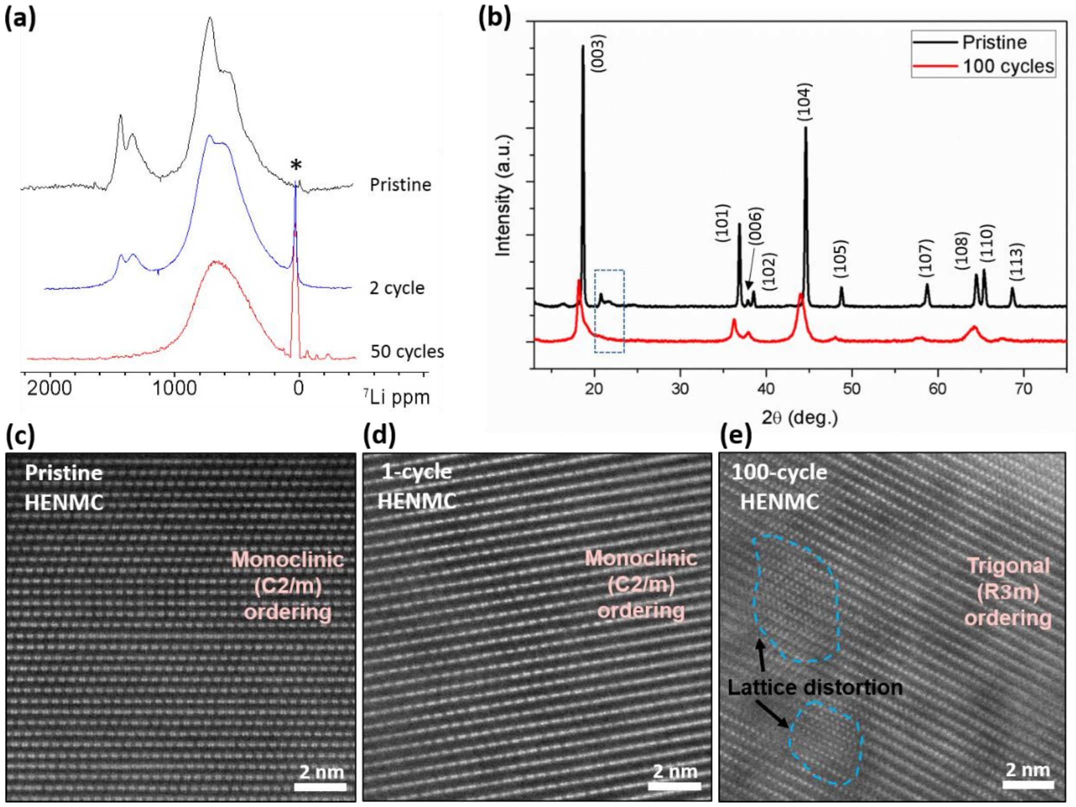

Figure 5.14 (a) ^{7}Li NMR spectra of pristine, 2-cycle and 50-cycle HENMC. The asterisk marks the location of dried electrolyte remaining in the two electrochemical samples. (b) XRD patterns of pristine and 100-cycle HENMC. (c-e) HAADF-STEM images acquired from the bulk grain of pristine, 1-cycle and 100-cycle HENMC.

The XRD pattern of HEMNC cathode after 100 cycles shows dramatic differences as compared to that of the pristine sample (Figure 5.14b). The irreversible Li loss in TM layers is further confirmed since the superstructure reflection peaks between 20° and 25° are not visible in the 100-cycle sample (Figure 5.14b). Meanwhile, significant peak broadening and peak shift are observed for the HENMC cathode after 100 cycles. Such effects have also been observed in previous studies on Li-rich materials.[145,150,186,187] The peak broadening could result from strain generation and local structure disorder (or crystal defects) in the cathode material after long-term cycling. The peak shift towards lower angle indicates a unit-cell expansion of the cycled material, in particular, expansion of the interlayer spacing based on the peak shift of (003) planes to lower 2Θ value. Furthermore, a shoulder on the higher 2Θ side of the (003) peak, not visible on the pristine material, is observed in the cycled material.

The shoulder next to the (003) reflection may be due to structural distortion or phase transformation during cycling as suggested by Jiang et al.[65] On the other hand, the (108) and (110) peaks are merged into a single broad peak, which may correspond to the reflection from the cubic unit cell.[188] It is worth noting that the reflection peaks of AB_2O_4 type spinel phase are very close to those of the trigonal phase, but are at slightly lower angles. The peak shift and broadening may therefore be indicative of the formation of spinel phase in the cycled bulk material but the XRD results alone cannot be unambiguously identified.

Consistent with the NMR results discussed above, the Li_2MnO_3-like monoclinic domains with TM dumbbell features are observed from both pristine and 1-cycle HENMC samples, as shown in Figure 5.14c and d, suggesting the existence of Li in the TM layers. Although the quantification is practically impossible due to the severe peak overlap, the Li concentration in the 1-cycle HENMC material shows obvious nonuniformities within the particle interiors, an effect that is not observed in the pristine material, as revealed by the EELS spectra acquired from different regions of HENMC particles after 1 cycle (Figure 5.15). Li depletion is observed from some regions as evidenced by the lower Li K-edge intensity, suggesting the loss of Li from the cathode material in the first cycle, which is consistent with the loss of Li from the TM layer that was revealed by NMR data.

STEM imaging of HENMC cathode subjected to 100 electrochemical cycles also demonstrates consistent result with NMR and XRD results, where no Li_2MO_3-like monoclinic ordering with TM dumbbells can be detected (Figure 5.14e). EELS quantification also reveals that the O to TM ratio decreases from the pristine material to the 100-cycle sample. The results, therefore, suggest that the Li vacancies generated by the irreversible TM-layer Li loss are eliminated by a densification process accompanied with oxygen loss, the material has transformed into a $LiMO_2$-type trigonal phase with no Li in the TM layer. The densification process could disable the excess Li ions re-intercalated back into the TM-layer, resulting in loss of lithium. Accroding to Ceder et al.,[189] the oxygen redox activity originates from the Li-O-Li configurations in Li-rich layered material which create oxygen states positioned near the energies of the TM e_g^* and t_{2g} states that compete with the transition metal states for oxidation. Therefore, the loss of Li in the TM-layers in cycled HENMC will lead to the loss of Li-O-Li configurations, and therefore ultimately resulting a loss of electrochemical capacity arising from oxygen redox reaction.

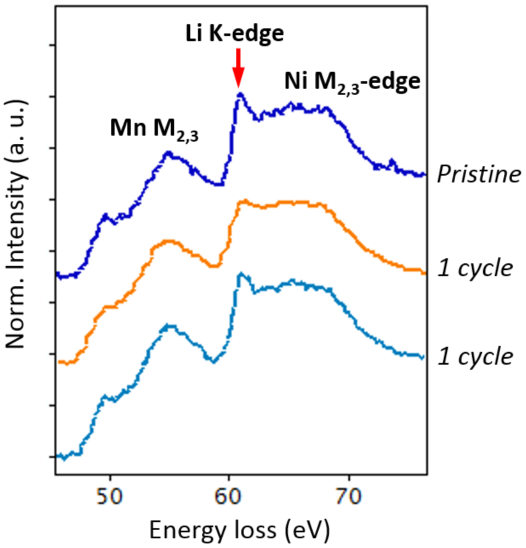

Figure 5.15 Low-loss EELS spectra acquired from different bulk regions of pristine and 1-cycle HENMC.

Furthermore, HAADF-STEM images of the 100-cycle sample shows nanoscale “defect domains” with highly distorted lattice fringes on a nanometer lengthscale that are randomly distributed within the particle interior (Figure 5.14e). The nanoscale lattice distortions are also observed from different particles, as shown in Figure 5.16. As can be seen from the images shown in Figure 5.14e and 5.16, the distinct TM-O-Li layered ordering are lost, i.e. lattice defect or mismatch of (003) lattice planes, in the nanoscale domains associated with TM migration. These nanoscale lattice distortions are more precisely ascribed as structural defects rather than the formation of spinel phase, in light of the cycling-induced spinel grains discussed in the next section.The appearance of these lattice distortions could be the reason for the peak broadening observed in the XRD pattern discussed above. These severe lattice lattice defects in the bulk material could result from the oxygen evolution and Li loss during cycling. The distortion of the regular lattice planes disrupts the well-defined layered structure and will likely block the Li ion diffusion pathway during charge/discharge, and ultimately leading to reduced Li deintercalation/intercalation and thus capacity fade.

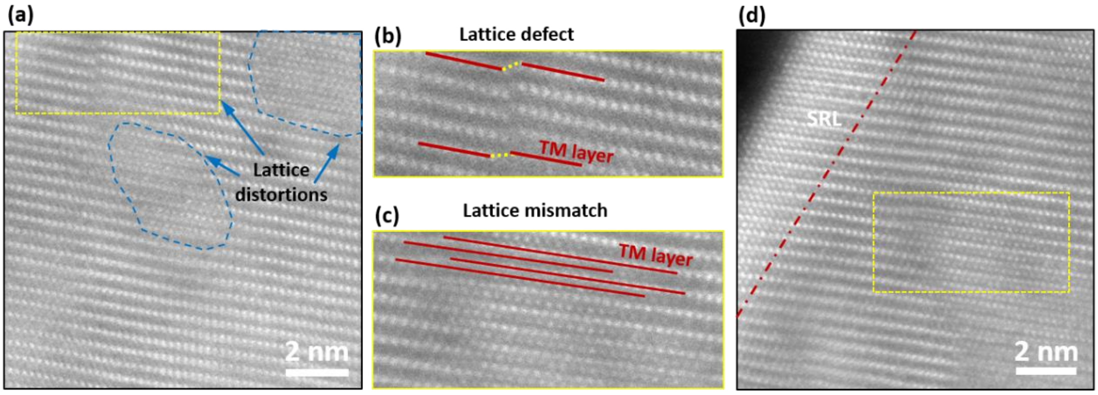

Figure 5.16 (a, b) HAADF-STEM images of 100-cycle HENMC. (c, d) STEM images demonstrating the lattice distortion from the regions marked with yellow rectangles in (a, b)

5.4.2 Formation of Cycling-Induced Spinel Grains

Following extensive analysis of the 100-cycle HENMC cathode, we also observed that some grains having a completely different structure than the layered ($R\bar{3}m$) phase. As pointed out in Chapter 3 there are still many unclear questions regarding the "layered to spinel" transformation in Li-rich cathode materials. Here, the presence of large-scale spinel grains and their spatial distribution are clearly resolved using atomic-resolution STEM imaging for the first time. Figure 5.17a shows a HAADF-STEM image acquired from a 100-cycle HENMC particle, the grain exhibits an entirely different atomic arrangement with the layered phase. The size of this newly-formed grain is about a few hundred nanometers in width, as indicated in the lower magnification image shown in the insert of Figure 5.17a highlighted in yellow. The atomic ordering of this cycling-induced new phase grain is clearly revealed from the higher magnification image shown in Figure 5.17b, with the corresponding FT diffractogram displayed in Figure 5.17c. The FT diffractogram of this cycling-induced grain can be indexed to the $[110]_S$ zone axis of $Fd\bar{3}m$ spinel phase. To further support the identification of this phase, a simulated STEM image of the spinel phase in the $[110]_S$ projection is shown in the upper right inset of Figure 5.17b, showing good agreement with the experimental result based on the atomic model (Figure 5.17e). There are, however, occasional lattice defects distributed in the newly-formed spinel grain, (identified with a red arrow in Figure 5.17a).

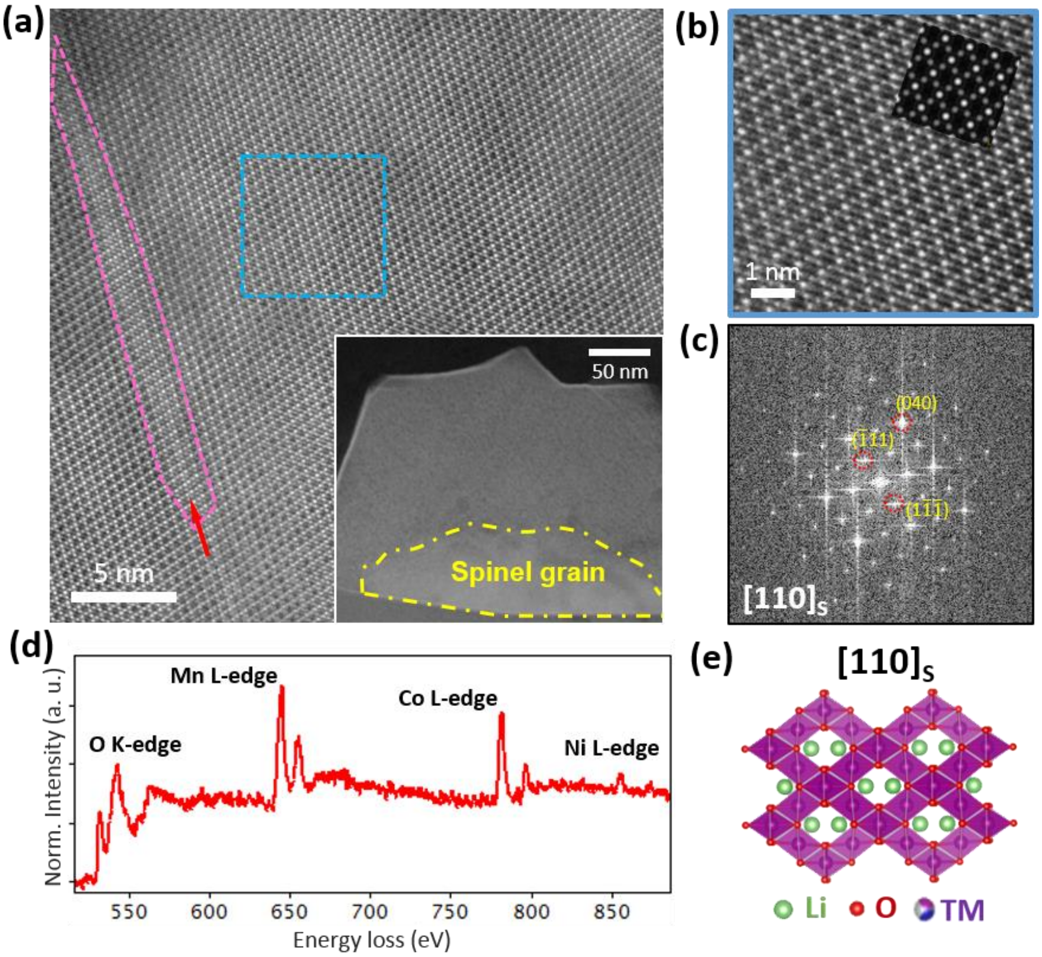

Figure 5.17 (a) HAADF-STEM image acquired from the spinel grain of HENMC after 100 cycles. The grain is marked in a lower magnification image at the bottom right inset of (a). (b, c) A higher magnification HAADF-STEM image and the corresponding Fourier transform diffractogram showing the spinel structure; a simulated HAADF image of the corresponding orientation is shown in the inset of (b). (d) EELS spectrum from the spinel grain shown in (a). (e) Atomic model of the LiM_2O_4 spinel phase in the [110] orientation. The subscript S denotes spinel ($Fm\bar{3}m$) structure.

The composition of the cycling-induced spinel grain is also investigated using EELS. Figure 5.17d shows the EELS spectrum acquired from the spinel grain in Figure

5.17a. Mn is still present as a major component in the spinel phase as anticipated, since the overall material is Mn-rich at beginning. Interestingly, an intense Co L-edge is detected from the new phase, indicating that the spinel grain is with a high Co content. A tiny amount of Ni is also present in the spinel phase as evidenced by the weak Ni L-edge in the spectrum. The L_3/L_2 peak intensity ratio of Mn $L_{2,3}$-edges is close to that of Mn^{4+},[174] indicating the majority of Mn ions are in the tetravalent state. Given the fact that Mn^{4+} ions are electrochemically inert and Co^{3+} ions are also electrochemically inert up to the 4.6 V potentials applied for charging,[188] the transformation of layered phase to this form represents a mechanism for performance decay. Furthermore, the formation of spinel grains could increase the Li^+ diffusion energy barrier at the spinel-layered interface, thus, influencing the kinetic behavior of HENMC cathode.

As discussed above, STEM characterization provides concrete evidence of spinel grain formation in the bulk HENMC material after cycling. These large spinel grains can be found either in the middle of a particle (Figure 5.17) or near the surface (Figure 5.18), and these newly formed spinel grains are usually hundreds of nanometers in size. Therefore, our results clearly reveal that the cycling-induced spinel phase is in the form of large grains rather than small nano domains. It can be seen from the low-magnification image (inset of Figure 5.17a) that a sharp grain boundary is located between the cycling-induced spinel grain and the adjacent layered grain underneath, whereas the top part of the spinel grain does not have a clear boundary and the spinel phase smudges into the surrounding grains. Therefore, it is likely that the layered-to-spinel phase transformation is initiated from the grain boundary and grew during cycling.

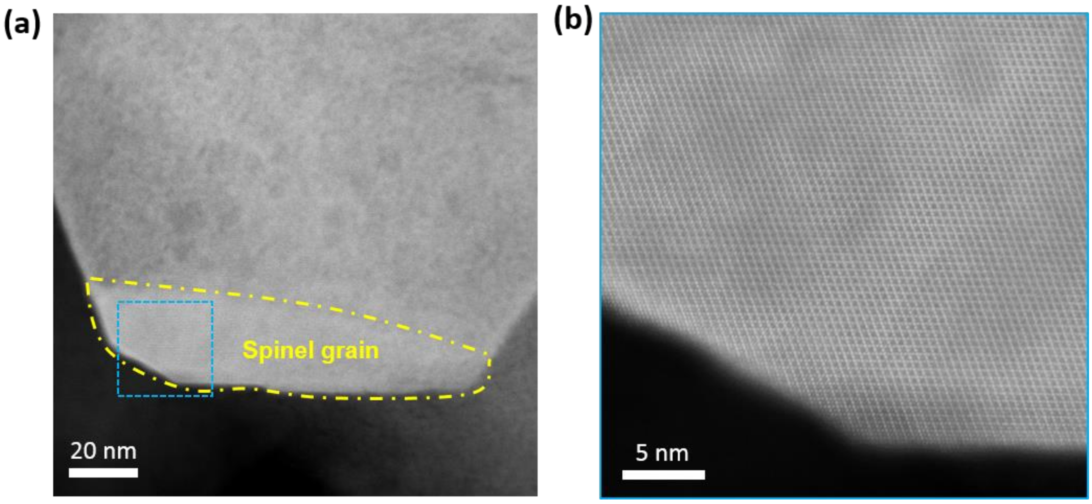

Figure 5.18 HAADF-STEM images showing the spinel grain in 100-cycle HENMC.

In fact, a thin layer of spinel phase is readily observed at the grain boundary in the 1-cycle HENMC cathode, as shown in Figure 5.19, which may be the nucleation site of the cycling-induced spinel grain. Since we also observed spinel grains formed near the particle surface (Figure 5.18), it is also possible that the spinel grain might grow from the particle surface to the interior. Based on the observations, the growth of spinel grains appear to be initiated at boundaries, either a grain boundary or the particle surface.

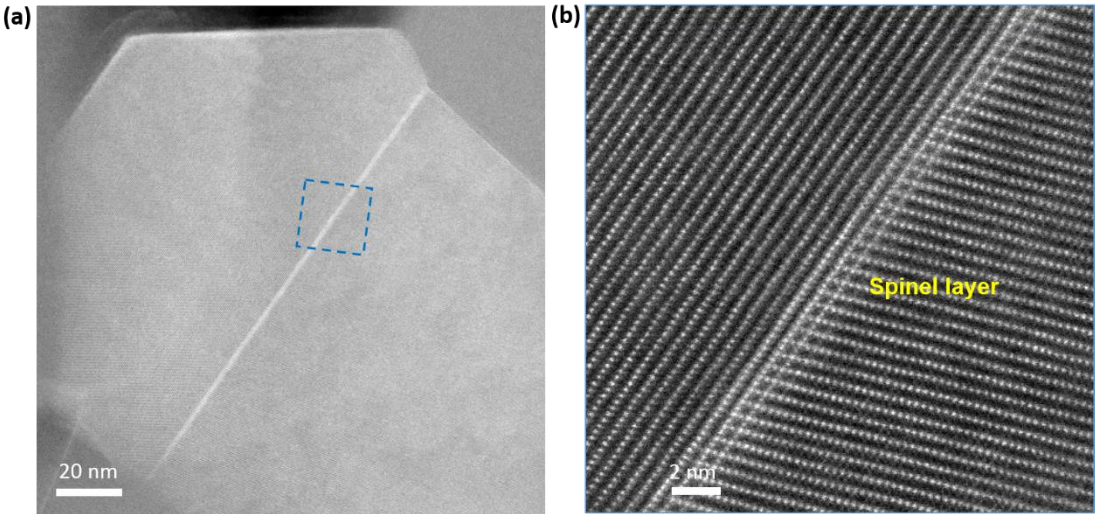

Figure 5.19 HAADF-STEM image showing the grain boundary of 1-cycle HENMC. (a) Low-magnification image. (b) High-magnification image from the region marked in (a).

The overall structural evolution of HENMC is illustrated in the schematic diagram shown in Figure 5.20. The SRL formation on HENMC particle surfaces originate in the first cycle. Although the thickness of SRLs show some variations among different locations, the SRLs do not exhibit prominent growth during the subsequent cycles. Therefore, they are not the main reason for the drastic performance decay. More severe changes take place in the particle interior. The material suffers slight Li loss in the first few cycles, followed by more dramatic losses during extended cycling, leading eventually to a complete loss of Li in the TM-layers. The significant Li loss in the bulk and the formation of nanoscale lattice distortions will lead to the loss of oxygen redox activity and hinder the Li diffusion from bulk to surface (and into the electrolyte), respectively, which both drastically reduce the cell capacity. In parallel, the layered-to-spinel phase transformation leads to the formation of large-scale spinel grains which also contributes to the performance degradation. The results suggest that coating or surface modification methods could be beneficial for inhibiting the surface degradation but will likely be insufficient for preventing the severe capacity decay, since the nanoscale lattice distortion and spinel grain formation could proceed from the particle interior. Therefore, modification of the bulk structure should be considered in order to stabilize the structure of Li-rich cathode material for better capacity retention.

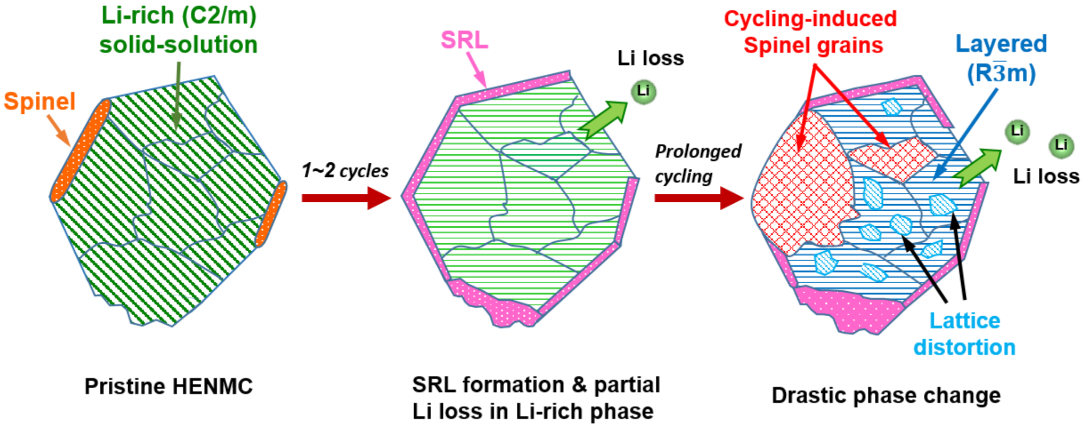

Figure 5.20 Schematic diagram showing the surface and bulk evolutions of HENMC cathode material during electrochemical cycling.

5.5 Conclusion

In conclusion, we have shown that the structure of the HENMC cathode material appears to be a solid solution based on *C2/m* symmetry with thin spinel layers present on certain facets. The structural and chemical evolution of cycled HENMC were systematically investigated from surface to interior. The HENMC particles undergo structural transformation after 1 cycle, where SRLs are formed on the particle surface with ~2 nm in thickness. The SRLs are Li-depleted and show no significant growth after extended cycling. In addition, an amorphous CEI layer is observed from the cycled particle surface that contains Li, C, O, F and Mn with about 20-30 nm thickness in some region. The presence of Mn^{2+} species in the CEI layer indicates Mn dissolution from the HENMC cathode into electrolyte during cycling.

More drastic changes were observed in the bulk material. The HENMC cathode suffers irreversible Li loss after long-term cycling. The Li ions in the TM-layers are fully lost, and the bulk material undergoes a densification process such that the bulk material has transformed into a $LiMO_2$-type layered phase. Meanwhile, the particle interior forms nanoscale defect domains with severe nanoscale lattice distortions and defects randomly distributed in the layered grains. More significantly, some of the layered grains has completely transformed in to a LiM_2O_4 (M=Mn, Co, Ni) spinel phase from either particle interior or near the surface. The observation of these large cycling-induced spinel grains with hundreds of nanometers in size clarifies the longstanding ambiguities on the “layered-to-spinel” transformation in Li-rich cathodes. Our findings reveal that, although the irreversible surface reconstruction could contribute to the cell performance decay, the more prominent bulk structural and chemical changes would be the main reasons for the severe performance deterioration of the Li-rich cells. The results thus suggest the importance of bulk modification techniques in order to stabilize the structure of Li-rich cathode material.

Chapter 6

3D Reconstruction of Lithium-Ion Battery Cathodes

Although two dimensional (2D) TEM imaging has shown some evidence of electrode degradation associated with structural change at the nanometer scale, it is clear that three dimensional (3D) imaging over larger volumes is necessary in achieving a complete picture of the geometric evolution of the cathode microstructure upon electrochemical cycling. Dual beam focused ion beam-scanning electron microscopy (FIB-SEM) is a promising technique that can be applied in serial sectioning and imaging for 3D reconstruction. In this chapter, the effect of electrochemical cycling on lithium-ion battery cathodes will be analyzed from 3D perspective. The microstructure of both pristine and cycled $LiNi_xMn_yCo_{1-x-y}O_2$ (NMC) and $Li_{1.2}Ni_{0.13}Mn_{0.54}Co_{0.13}O_2$ (HENMC) cathodes were successfully reconstructed using state-of-the-art FIB-SEM 3D reconstruction. The cycling-induced structural evolution of different cathodes were semi-quantitatively analyzed in order to determine the influence of electrochemical cycling on lithium-ion battery cathodes.

6.1 FIB-SEM 3D Reconstruction: Motivation and Issues

During the past decades, there has been a rapid development in the methodology for 3D reconstruction. X-ray tomography, appears as the prime technique for 3D characterization, is a nondestructive method which allows for time-dependent study.[190–194] Using X-ray tomography, a serial of transmission (absorption) images taken at different projections are collected and used for 3D reconstruction. However, the voxel resolution of X-ray tomography is relatively large, usually in micron or sub-micron scale, which is sometimes insufficient for capturing nanoscale features. Although the appearance of TEM tomography technique overcomes the limitation of X-ray tomography, which can provide a much higher spatial resolution and enable the observation of fine features, this method can only be used to reconstruct small volume sizes.

An alternative method to X-ray and TEM tomography is serial sectioning.[195–197] The procedure for serial sectioning is mainly composed of two steps, which are then repeated until the sample sectioning is finished. The first step is sample sectioning, which can be achieved by various methods, such as cutting, polishing, and sputtering. In this step, a constant depth of sectioning is required between each slice to ensure the accuracy of reconstruction. The second step is the collection of 2D imaging data from each slice, sometimes this data could be collected simultaneously during sample sectioning, depending on the method being used.

Among various serial sectioning techniques, FIB-SEM has shown its own potential in 3D reconstruction. Using FIB, a high energy focused ion beam with a small spot size is generated and the localized material will be removed by the interaction of the high-energetic ions with the target sample. Initially, FIB-SEM is not specially designed for 3D serial sectioning, it has been used in site-specific analysis and nanofabrication in different research areas.[198] However, this technique is quite suitable for serial sectioning with ion beam milling. Using dual beam FIB-SEM, one could obtain the slice spacing less than 20nm,[199,200] comparable to the pixel resolution of the

2D image. Meanwhile, the dual beam FIB-SEM system enables the synchronous milling and imaging, which is impossible to achieve by using other conventional polishing techniques.

Both FIB-SEM and X-ray tomography techniques have been widely used in 3D reconstruction of energy materials and enable quantitative assessment on their complex microstructures. The 3D structure of electrodes in lithium-ion batteries have been successfully reconstructed and a number of geometric parameters—volume fraction, surface area, particle size distribution and tortuosity have been extensively analyzed.[201–215] With X-ray tomography, the 3D microstructure of graphite and tin (II) oxide negative electrodes were successfully reconstructed and the geometric parameters were analyzed.[201,202] Heat generation was simulated based on the 3D microstructure of the $LiCoO_2$ cathode acquired by X-ray nano-computed tomography by Zhu et al..[216] With synchrotron radiation X-ray tomographic microscopy (SRXTM), 3D microstructure of $LiNi_{1/3}Mn_{1/3}Co_{1/3}O_2$ cathode was reconstructed and the particle size distribution of the cathode were analyzed using a segmentation algorithm that identifies the individual particles.[217] By tuning the X-ray energies appropriately, an optimum contrast for the cathode active materials $LiCoO_2$ (LCO) and NMC could be achieved, as shown in Figure 6.1.[204] However, one disadvantage of this method is the difficulty of distinguishing the carbon-doped binder phase from the pore space due to the small particle size and the low X-ray absorbance of the binder phase.[203,207] Recently, Thiele et al. managed to insert the carbon-binder domain of LCO cathode by combining statistical modeling with X-ray tomography,[207] but to obtain a complete 3D dataset including all the three phases with good spatial resolution remains a major challenge for X-ray tomography. Additional FIB-SEM 2D information was still needed for creating a complete 3D hierarchical reconstruction of the cathode.[208]

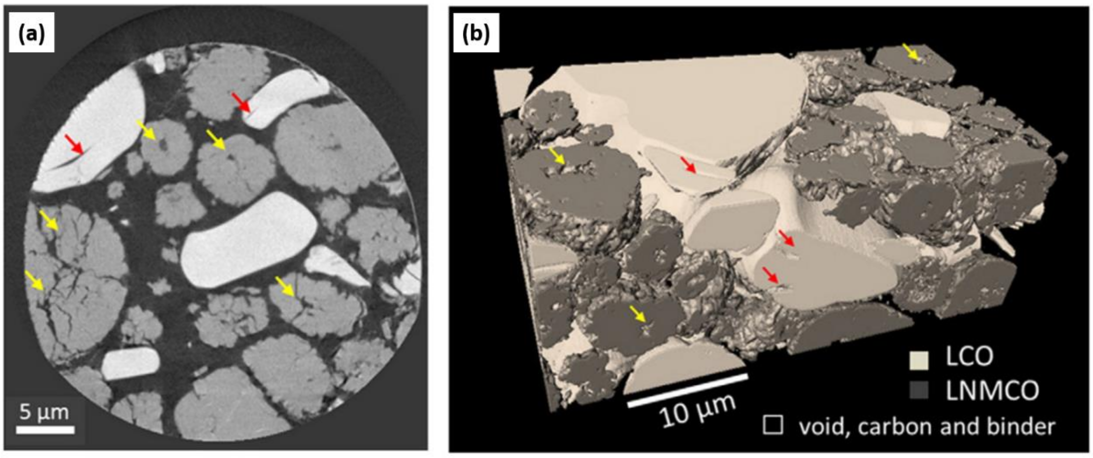

Figure 6.1 (a) A cross-section image from transmission X-ray tomography (TXM) reconstruction, a good contrast between the LCO and NMC is achieved. (b) 3D reconstructed volume of the electrode. From reference [204].

With the total volume sampling and higher spatial resolution, the reconstruction of lithium-ion battery electrodes with the FIB-SEM technique has been reported by several groups. [209–215] In previous work, Ender et al.[209,210] have successfully reconstructed the 3D structure of $LiFePO_4$ cathode and carried out detailed calculations on the microstructure parameters including particle size distribution and tortuosity, as shown in Figure 6.2. The 3D microstructure of LCO cathode has also been widely studied using FIB-SEM. Wang et al.[211] calculated the tortuosity based on an actual 3D structure while the internal cracks and grain boundaries of LCO active particle were discovered. The internal cracking and grain boundaries of LCO particles were observed from 3D reconstruction of a LCO electrode by Wilson et al..[212] The influence of these features on battery performance was evaluated. Whilst there are many detailed structural studies of different cathodes, the correlation between 3D microstructural changes and electrochemical cycling remains comparatively unexplored for cathode materials. Herein, we implement FIB-SEM 3D reconstruction to study the structural evolution of lithium-ion battery cathodes during electrochemical cycling, in order to obtain a more complete insight into the cathode degradation process.[218]

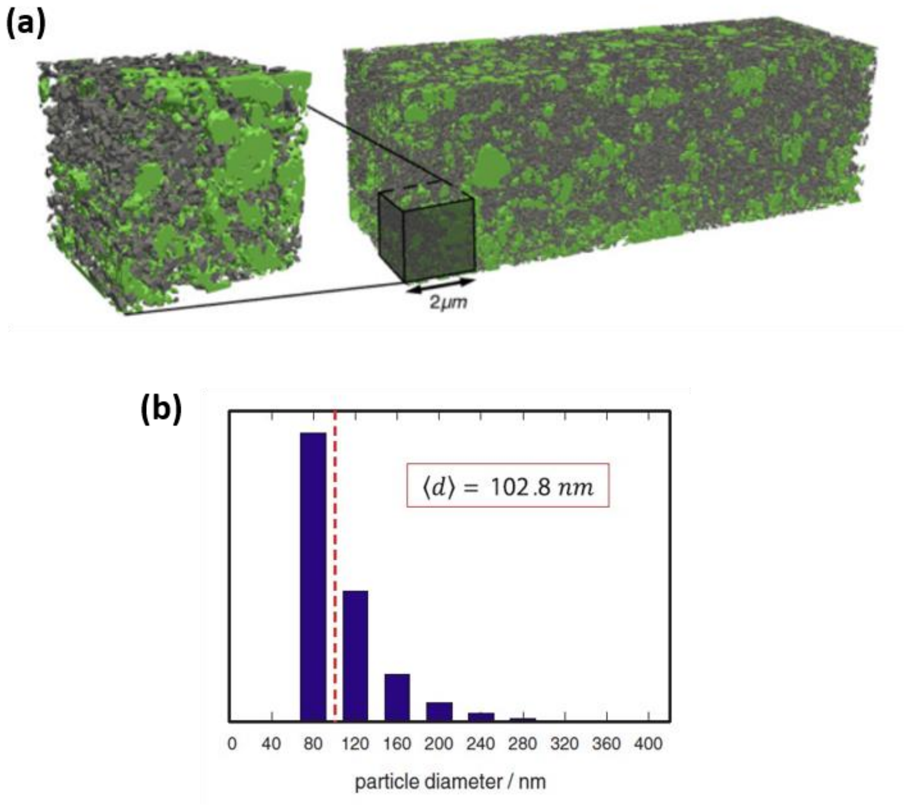

Figure 6.2 (a) Reconstructed 3D volume of $LiFePO_4$ electrode. $LiFePO_4$ is shown in green, carbon black is shown in dark gray, and pores are transparent. (b) Particle size distribution of the $LiFePO_4$ sample. From reference [209,210].

6.2 Sample Preparation and FIB-SEM 3D Reconstruction

6.2.1 Electrochemical Test

A commercial HKE-IMP-0660J0 battery (HECO, Shanghai, China) with $LiNi_xMn_yCo_{1-x-y}O_2$ (NMC) as the active material was studied. The battery was fully discharged, then disassembled and dried in a glove box. The NMC cathode sheet was cut into small circular pieces and constructed into coin cells with Li metal as the counter electrode and $LiPF_6$ in ethylene carbonate/dimethyl carbonate (EC/DMC 1:1-v/v) as electrolyte. The half-cells were then subjected to 20 and 50 electrochemical cycles, respectively, the cycling performances are shown in Figure 6.3. The cells were then disassembled and dried in the glove box. Note that the NMC cathode taken from a commercial battery may have undergone a few pre-cycles from battery manufacturer. In the following discussion, we refer the coin cell made with the commercial NMC cathode before cycling as a “pristine” sample, which relates to the NMC cathode before the cyclic test in a half-cell. In the following study, we use the microstructure observed in the pristine NMC sample as a starting point (with pre-existing features generated from pre-cycles) in contrast to the sample after cycling test.

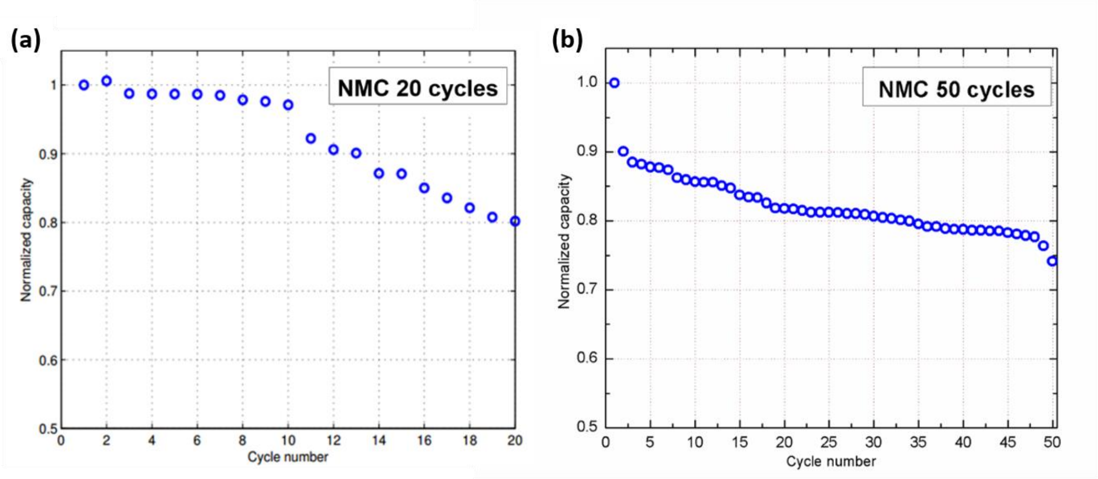

Figure 6.3 Cycling performance of NMC cathodes for: (a) 20 electrochemical cycles, (b) 50 electrochemical cycles.

The lab-scale $Li_{1.2}Ni_{0.13}Mn_{0.56}Co_{0.13}O_2$ (HENMC) cathode material was synthesized using the co-precipitation method. The details for cathode preparation is introduced in Chapter 5. The HENMC cathodes were constructed into half-cell configurations with Li as counter electrodectrode and 1M $LiPF_6$ EC/DMC (1:2-v/v) as electrolyte. The cells were subjected to 1 and 50 electrochemical cycles, respectively. The cycling performance of the HENMC cell subjected to 50 cycles is shown in Figure 6.4. The cells were then disassembled and dried in a glove box. All the cathode samples were positioned on the SEM stages using conducting carbon tape, with silver paste applied at the edge to enhance the conductivity.

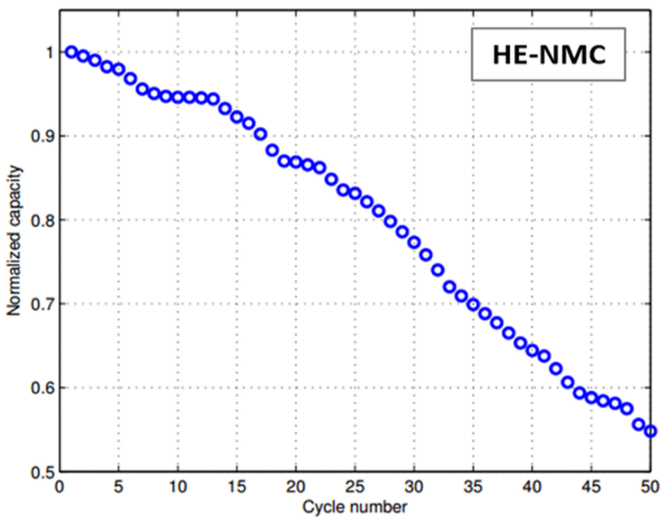

Figure 6.4 Cycling performance of HENMC cathode with 50 electrochemical cycles.

6.2.2 FIB-SEM Serial Sectioning

The samples were serial-sectioned and imaged with a Zeiss NVision 40 dual beam FIB-SEM equipped with a gallium (Ga) ion beam source and a Schottky Field Emission Gun (FEG). In general, the samples were milled by a high-energy Ga ion beam and a series of cross-sectional SEM images were acquired with the electron beam. Then, these SEM images were converted into a 3D dataset and analyzed. A tungsten (W) coating was deposited on top of the region of interest (ROI) to protect the sample's intrinsic surface morphology from high-energy Ga ions and reduce curtaining effects on the sectioned face. Figure 6.5a shows an SEM image of a NMC cathode after serial sectioning. As the duration time of the serial sectioning process is strongly dependent on the intensity of the ion beam used for milling (faster milling uses higher current), and the quality of the section is affected by the ion beam size, a relatively small ion beam current (1.5nA at 30KeV) was selected to mill and polish the cutting surface, in order to produce an ideal surface flatness with a reasonable time duration.

Because the incident electron beam does not scan the sectioned surface normal to the sectioning plane due to the intrinsic angle between the electron beam column and the ion beam column (54°from the electron beam and parallel to the surface), the apparent tilt (36°) of the image was compensated by software before image collection, as shown in the schematic diagram in Figure 6.5b. Also due to the geometry of the ion and electron beam columns with respect to the sample surface, an apparent image drift is generated with each slice. This effect was corrected by software using reference markers as the images will appear to shift upwards during serial sectioning. Markers were also used to calibrate and adjust slight drifts in the horizontal direction (on the image plane).

The sampling of the acquired SEM images is 1024 × 768 pixels with the pixel sizes of approximately 25 nm (for NMC cathode) and 35 nm (for HENMC cathode), while the spacing between each slice were 50 nm (for NMC cathode) and 70 nm (for HENMC cathode), respectively. A larger pixel size was chosen for HENMC cathode due to the larger size of the HENMC secondary particles compared with regular NMC. These imaging and sectioning parameters were selected to be consistent with the sampling needed to represent, with fidelity and given the time constraints of the sectioning work of a representative volume, the various components of the cathode (the features in NMC particles were consistently detected at the resolution provided by the SEM), so as to provide reasonably accurate 3D reconstruction. For the NMC cathode samples, 300 consecutive cross-section images were obtained from a volume of ~ 5100 μm^3, and 280 cross-section images were obtained from the HENMC cathode samples corresponding to a volume of ~11800 μm^3. The total 3D sampling volume is evaluated to be sufficient for this study as it yields the measured volume fraction consistent with the predetermined volume fraction of the cathode (see details in Appendix II).

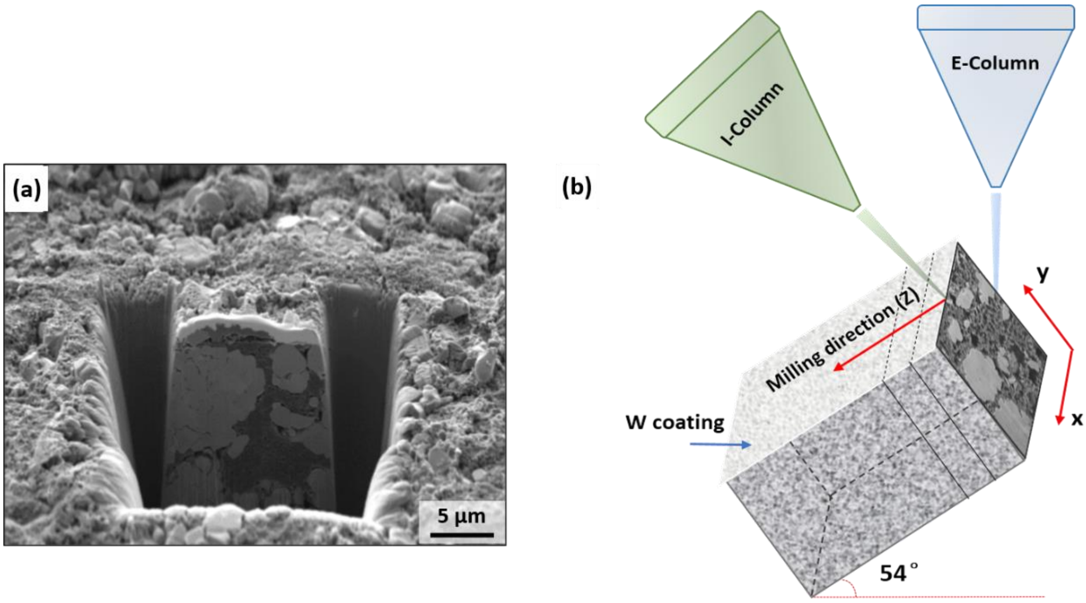

Figure 6.5 (a) An example SEM image of a NMC cathode after FIB milling. (b) Schematic of FIB serial-sectioning and image acquisition process.

For large scale sectioning and comparative purposes, an ion beam cross-section polisher (JEOL IB-09010CP) was also used to prepare the 2D cross-sections of the pristine and cycled NMC cathodes. The sample was mounted on a Mo block and a thin layer of Au was deposited on the sample surface with physical vapor deposition by Ar ion sputtering. The sample was then milled by the cross-section polisher with an Ar ion beam at 5 keV.

6.2.3 Image Segmentation

Before the raw 2D image dataset can be analyzed in a meaningful and systematic manner, the images must be digitally segmented into three distinct phases: (i) active material (AM), (ii) carbon-doped binder (CB), and (iii) pore spaces which are filled with electrolyte during operation. The term “carbon-doped binder” indicates the additive mixture of conductive agent (carbon black) and polymer binder (PVDF). Usually, the carbon black is mixed with PVDF to bind active particles together and enhance the conductivity of electrode, so they are defined as one phase of additives under segmentation. The epoxy infiltration is avoided in this work, so that the sample preparation is less invasive. The 3D reconstruction process is illustrated with our lab-scale NMC cathode as shown in Figure 6.6. The in-house segmentation algorithm is based on thresholding and gradient analysis implemented in MATLAB utilizing the IMAGE PROCESSING toolbox.† The key aspects of the electrode microstructure from SEM images that facilitate a reliable semi-autonomous segmentation are: (i) the separation in grey-scales of the different phases – the AM phase with lighter gray, the CB phase typically in medium gray, and pore spaces appearing as darkest features, and; (ii) the distinctive vertical grooves on the active material that are caused by the FIB and general milling process.

Despite minor artifacts which can be subsequently corrected afterwards, we are able to obtain good accuracy by carefully controlling the various parameters that characterize the weighting between grey-scale threshold and analysis of gradient values in an automated fashion. The systematic error arising from the image processing step is estimated by comparing the experimental volume fraction deduced by our algorithm with the expected volume fraction of a lab-made NMC cathode with known composition (based on weight ratio of AM, carbon black, and PVDF). A comparison of the measurements and expected values leads to a small systematic error of less than 2%. Figure 6.6a shows an example of a series of raw 2D images of a lab-scale NMC cathode, and the corresponding segmented images are shown in Figure 6.6b. A 3D image of the reconstructed cathode volume using the segmented images is shown in Figure 6.6c with: (i) AM in white; (ii) CB in yellow; and (iii) pore spaces in transparent. Separate 3D structures revealing the spatial distribution of the active material (NMC particles) and binder phases are shown in Figure 6.6d and 6.6e. These 3D rendered volumes show that the structure of these components is sufficiently well represented and can be subsequently used to calculate the volume of the particles and in any further modeling work aimed at predicting the transport properties of the cathodes.

---

† The Image processing algorithms were designed and modified by *Adam Gully* and *Jamie M. Foster* from McMaster University.

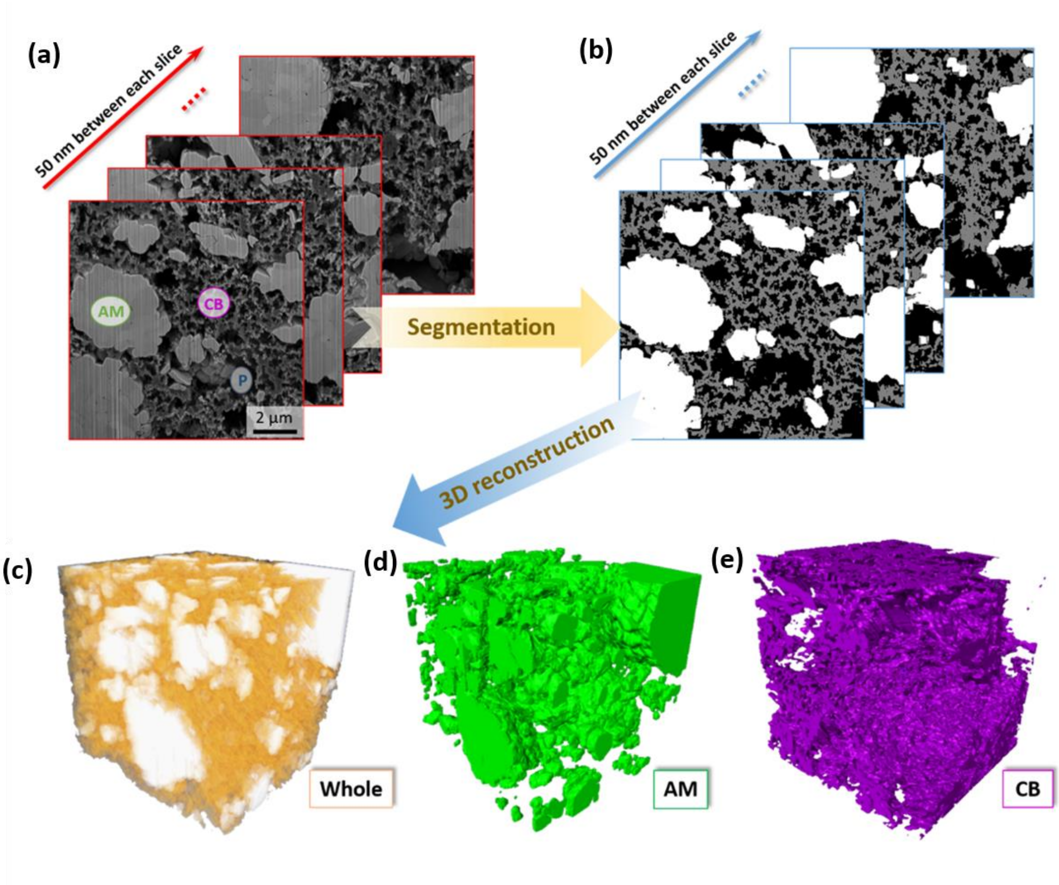

Figure 6.6 Schematic diagram of the 3D reconstruction approach: (a) a series of cross-sectional SEM images collected by FIB; (b) the segmented counterparts of the images shown in (a); (c) a whole view of the reconstructed 3D NMC cathode structure; (d) and (e) reconstructed 3D structures of active material (AM) and carbon-doped binder (CB), respectively.

6.2.4 Neighbor Counting Method

In order to assess the evolution of the relative positioning of the important phases, we quantified the segmented structure with a "neighbor counting" method. This approach provides statistical analysis to assess the degree of connectivity between the surfaces of the active particles and the carbon-doped binder matrix. A "neighbor counting" algorithm was used to scan along each row of pixels (for a 2D image) or each row and column of voxels (for the 3D structure) in the directions parallel to the separator and current collector of the segmented dataset. The number of occurrences of a pixel or voxel of the active particles being in direct contact with binder matrix were counted. More precisely, the technique computes the probability of binder being adjacent with active material (PBA) as a function of depth into the cathode (i.e., in the direction perpendicular to the separator and current collector). The algorithm counts the number of voxels of CB phase being contact with AM phase (defined as $\mathrm{No.}_{\mathrm{BA}}$), and the number of voxels of CB phase being contact with the pore space (defined as $\mathrm{No.}_{\mathrm{BP}}$). The PBA value is then calculated based on the equation

$$\mathrm{PBA} = \frac{No._{BA}}{No._{BA} + No._{BP}} \tag{6.1}$$

And the "loss in connectivity" is calculated as

$$\text{connectivity loss\%} = \frac{PBA_{pristine} - PBA_{cycled}}{PBA_{pristine}} \times 100\% \tag{6.2}$$

6.3 3D Reconstruction for NMC Cathode

Figure 6.7a shows a top-view SEM image of the NMC cathode before cycling. The NMC cathode has a relative smooth surface where the active particles were tightly embedded in the CB matrix. However, some cracks were observed in the large secondary NMC particles of the pristine sample, as shown in Figure 6.7b. This is consistent with the expectation that the calendering process could lead to particle fracture due to the high pressure applied to the cathode.[219] The presence of these cracks in the particles could enhance the Li diffusion, and thus improve the cycling kinetics, but would also generate more exposed surface area for the side reactions with electrolyte.[212]

Figure 6.7c shows a cross-sectional SEM image of the NMC cathode after 20 cycles. We note that large gaps have formed inside the cathode, separating the active particles and binder, as highlighted with red arrows. This will be discussed below. In addition, cracks inside the secondary active particles are also observed in the cycled NMC cathode, and appear similar to those observed in the pristine sample. However, it is difficult to ascertain, from visual inspection alone, whether there are more fractured particles after electrochemical cycling. Figure 6.7d and 6.7e show the 3D reconstructions of the AM and CB phases of the pristine NMC cathode. Based on the reconstructed 3D structure, the volume fraction of the three phases in the cathode was calculated as: (i) 69% active material; (ii) 24% carbon-doped binder; and (iii) 7% pore spaces. The result shows that the majority of the cathode volume is occupied by the active material which would be beneficial in achieving a high battery capacity.

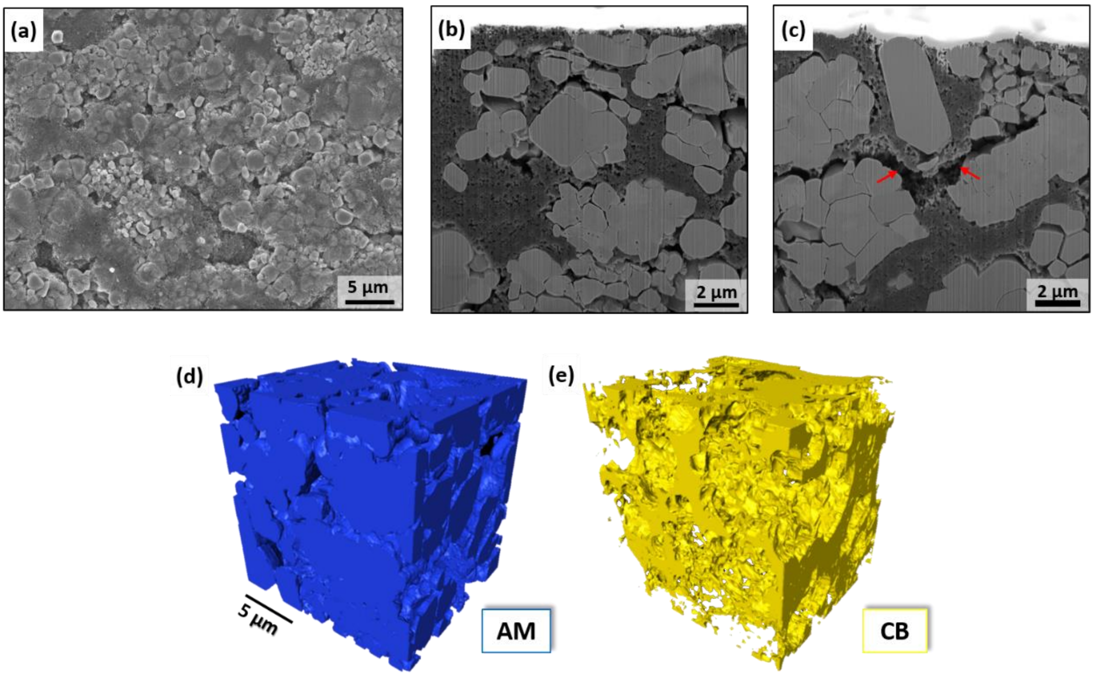

Figure 6.7 (a) A top-view SEM image of the pristine NMC cathode. (b), (c) Cross-sectional SEM images of the NMC cathode of pristine and 20 cycles, respectively. (d), (e) Reconstructed 3D structures of AM (active material) and CB (carbon-doped binder) of pristine NMC cathode, respectively.

In order to quantify the structural observations, particle size distribution analysis was performed on the segmented 3D dataset, and is shown in Figure 6.8a. The particle size was specified based on volume rather than diameter due to the irregular non-spherical shapes of NMC secondary particles. Because the sample contains both small fractured particles and large secondary ones, the particle size variation is large. Thus, the particle size distribution of active particles was calculated with different volume ranges, that is, the number of particles belonging to a given volume “bin” was counted. This should provide a general idea of the proportion of particles belonging to different size ranges. As shown in Figure 6.8a, the majority of NMC particles have sizes below 10 μm^3 and there are fewer large secondary particles with sizes above 100 μm^3. It is reasonable to expect few large particles due to the limited sampling volume. Compared with pristine NMC cathode, the cycled NMC cathode shows a small increase in the number of particles with smaller sizes (typically less than 1μm^3), indicating that there might be large particles fractured into small ones. It has been reported that the internal cracks may promote the particle fracture [212], so the cracks being observed from the pristine sample may contribute to the particle size change. However, local variations in the distribution of the AM phase cannot be ignored for the assessment of particle sizes, and the slight increase being observed in this comparison could be due to a combination factors, including the electrochemical cycling and sample inhomogeneity [220].

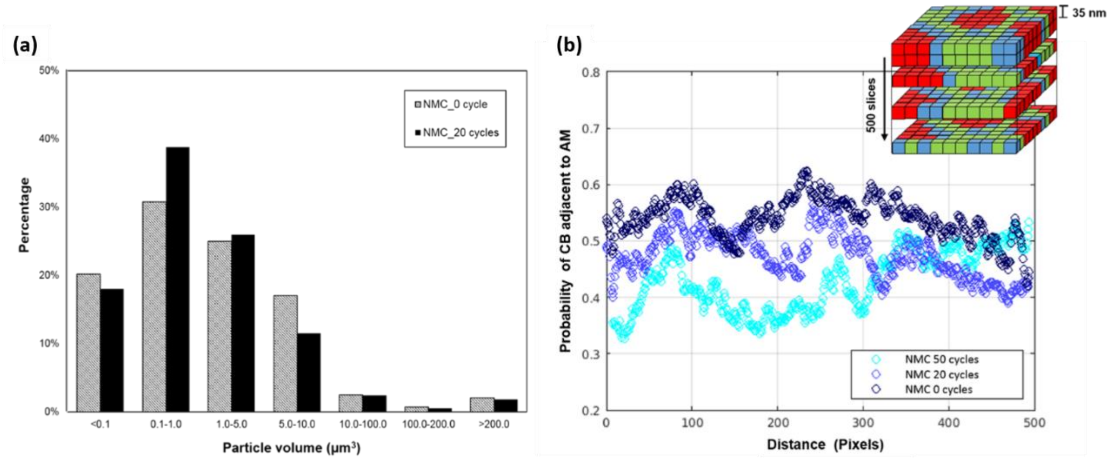

Figure 6.8 (a) Comparison of particle size distribution of pristine and 20 cycles NMC cathodes from 3D reconstruction. (b) Comparison of PBA of pristine, 20-cycle and 50-cycle NMC cathodes from 3D reconstruction.

From the comparison of pristine and cycled NMC cathodes, large gaps between active particles and binder are clearly visible from 2D cross-sectional images of the electrode after 20 cycles. To evaluate the connectivity between the CB phase and active particles, we performed an analysis based on the “neighbor counting” method to the segmented 3D dataset of the NMC cathodes at different cyclic numbers in order to extract the probability of carbon-doped binder being adjacent to the active particles (PBA) as a function of depth into the cathode. Comparing the pristine and cycled NMC cathodes, there is an obvious decrease in PBA of the whole sample with the increase number of cycles, as shown in Figure 6.8b. Each data point represents the probability of CB being in contact with active particle surface of each slice perpendicular to the depth of the 3D structure. The x-axis is the distance of each slice from the sample surface (close to the separator) in units of pixels, each pixel corresponding to the slice thickness (35 nm), as shown in the schematic diagram in Figure 6.8b. From the “neighbor counting” analysis, the average PBA of the pristine sample is around 0.54 and decreases to 0.48 after 20 cycles, thus an 11% loss in connectivity between AM and CB in the NMC cathode is observed after 20 cycles. We note that the value of the average PBA, e.g. 0.54, means 54% of the AM surface is in contact with the CB phase within the 3D volume. Moreover, the average PBA shows a further decrease to 0.43 when the cathode was subjected to additional cycling (50 cycles), the sample thus exhibits a 20% loss of AM/CB connection after 50 cycles. The results therefore indicate that the connectivity between AM and CB decreases with the increase number of cycles, where a cycling-induced detachment between the two phases was observed. However, local variations needs to be considered in order to assess the PBA changes.

To evaluate the influence of local microstructural variations and to validate the data obtained from 3D volumes, large cross-sectional images of the pristine and cycled NMC cathodes, with the depth covering the full cathode thickness and width of around 1 mm, were prepared using ion beam cross-section polishing. Three different locations were selected from each of the two samples, and a series of SEM images were collected at each location along the depth of the cathode.

Figure 6.9a and 6.9b are the large 2D cross-section images taken at one location within the pristine and 20-cycle NMC cathodes. As shown in Figure 6.9c and 6.9d, the PBA of the pristine NMC cathode has a relatively uniform distribution along the depth of the cathode indicating there is good contact between the AM and CB phases. Compared with the pristine sample, the contact area of the active particle and binder of the cycled NMC cathode decreased at some localized positions after electrochemical cycling where the PBA almost reached zero, and the average PBA dropped from 0.57 in the pristine state to 0.47 in the cathode after 20 cycles. The detachment of the CB phase from the active particle surface was revealed from the segmented 2D slice of the NMC cathode after 20 cycles, where a 17.5% decrease in PBA is detected, and this is consistent with the measurements in other locations of the cathode, as shown in Table 6.1. Based on the 3D and 2D “neighbor counting” results, the detachment between CB and AM appears to be prevalent in the NMC cathode after electrochemical cycling. We suggest that the origins of the binder detachment could be: (i) the volume expansion and contraction of the active particles induced stresses [221], and (ii) the local volume change of the anode which could influence indirectly the cathode structure especially the porous binder matrix.

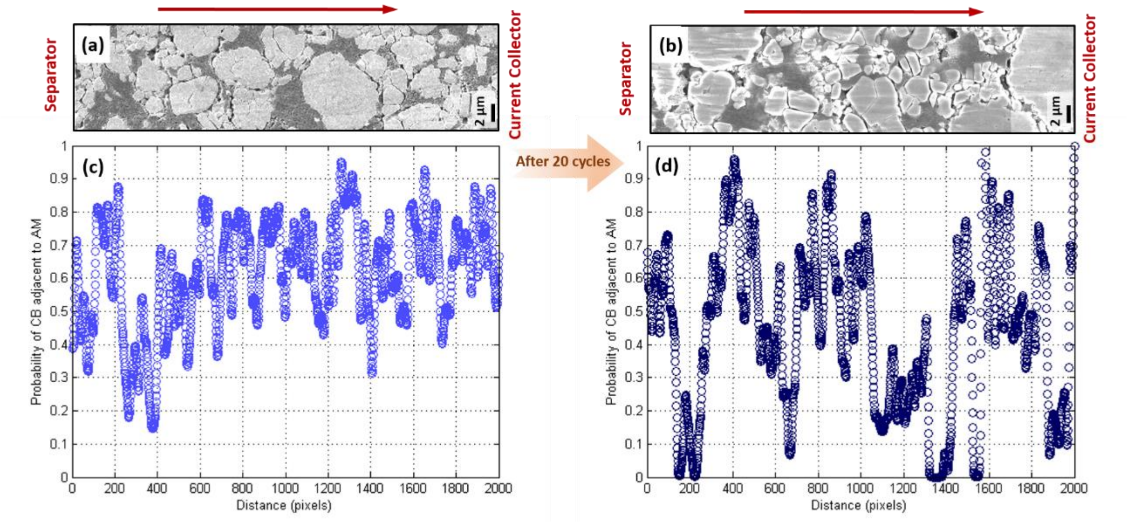

Figure 6.9 (a, b) Integrated 2D images of pristine and 20-cycle NMC cathodes within whole depth, respectively. (c, d) PBA of pristine and 20-cycle NMC cathodes, respectively.

Since the CB phase contains carbon black additive in order to enhance the electrical conductivity of the cathode, our results thus suggest that the detachment between the conductive CB phase and active particles will reduce the efficiency of electrons transport from the active particle (where Li^+ intercalation/deintercalation happens) to the current collector, in other words, it becomes increasingly difficult for electrons to connect from the active particles through the conductive CB network to the current collector. This effect could therefore contribute to the degradation of the battery performance after cycling (Figure 6.3). As shown in the results above, when the cell is suffering larger capacity loss from longer term cycling, from 20 cycles to 50 cycles, the cathode also loses AM/CB connectivity as indicated by the decreased average PBA values from 20 cycles to 50 cycles. The PBA loss as a function of cycle numbers therefore provides direct experimental evidence that the detachment effect correlates with the capacity loss. While we cannot exclusively attribute the cause-effect link between the PBA drop and the capacity loss at this point, the unambiguous drop of PBA evidenced from our measurements needs to be considered as a possible factor in the performance degradation, together with other effects such as electrolyte decomposition [97], and structure distortion of active materials,[36,40,140] while such effects have been observed from our study on NMC and HENMC cathodes that have been discussed in the previous chapters.

Table 6.1 Comparisons of the average PBA of 0 and 20 cycles NMC cathode at different locations.

	Average PBA		
	Location 1	Location 2	Location 3
NMC_0 cycles	0.57	0.56	0.58
NMC_20 cycles	0.47	0.48	0.49

6.4 3D Reconstruction for HENMC Cathode

Figure 6.10a shows a top-view SEM image of the single cycle HENMC cathode. In addition to the very large secondary particles, there are numerous significantly smaller primary HENMC particles embedded in the binder matrix with diameters in the order of hundreds of nanometers. Compared with the NMC cathode studied above, the HENMC active material has smaller primary particle sizes and these are less compact. The representative 2D cross-section images of the 1 and 50 cycles HENMC cathodes are shown in Figure 6.10b and 6.10c. In each 2D SEM cross-sectional image, the irregular shaped HENMC active particles are clearly visible in light grey intensity, while the CB phase appears in medium contrast as compared to the pores, which are seen as the darkest features. While the HENMC secondary particles have much smaller grains and pores, compared to the cracks existing in the NMC secondary particles, the pores distributed inside the HENMC particles appear to be poorly connected to the surface. This may limit electrolyte penetration within the HENMC secondary particles. The 3D reconstruction of active particles of the HENMC is shown in Figure 6.10d, the active material phase is composed of a variety of irregular shapes of small and very large particles. The corresponding carbon-doped binder phase is shown in Figure 6.10e.

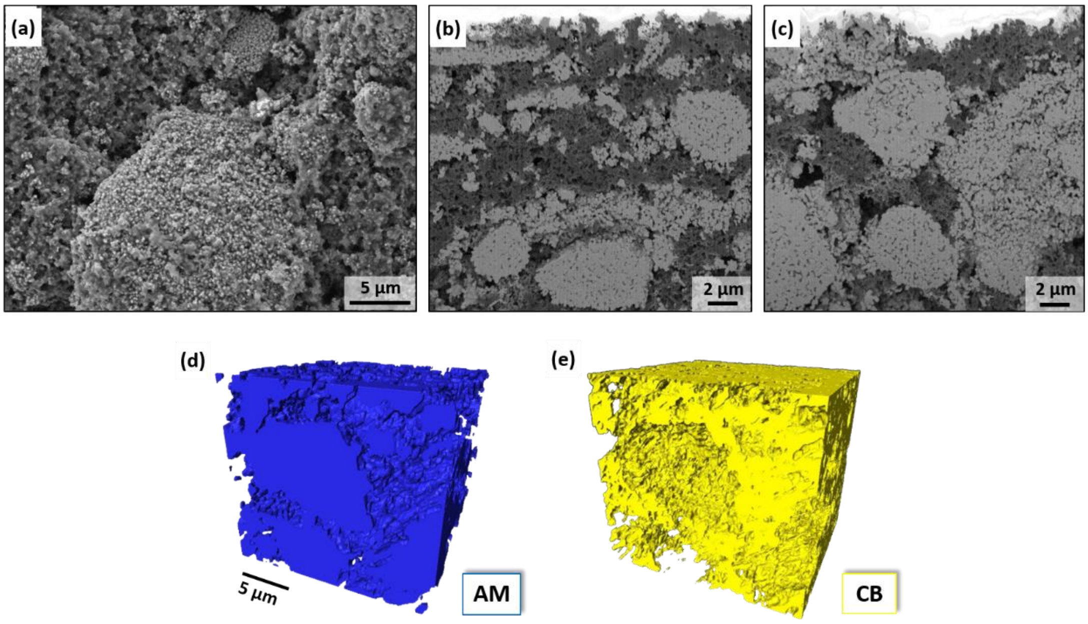

Figure 6.10 (a) A top-view SEM image of 1-cycle HENMC cathode. (b), (c) Cross-section SEM images of the HENMC cathode after 1 and 50 cycles, respectively. (d), (e) Reconstructed 3D structures of active material (AM) and carbon-doped binder (CB) of 1-cycle HENMC cathode, respectively.

As observed from the cross-sectional images, the size distribution of the HENMC active particles is broad, from submicron primary particles to large secondary ones. Figure 6.11a shows the comparison of the particle size distributions of HENMC samples at 1 and 50 cycles. The majority of particles are below 1 μm^3 and about 40% of the particles are hundreds of nanometers in diameter. Only a few large secondary particles are found contributing to less than 10% of the total distribution. The existence of a large fraction of small particles in the electrode-- has important implications on its performance. The specific surface area of the active material will be dramatically increased, thus facilitating electrode/electrolyte side reactions which adversely impact the battery capacity and lifetime (the cycling performance of the HENMC cathode is shown in Figure 6.4). After 50 cycles, there is an increase in the fraction of small particles (volume < 0.5μm^3). The medium sized particles thus appear to have fractured into small ones. However, yet again, local variation of the AM phase distribution has to be taken into account for the observed particle size changes.

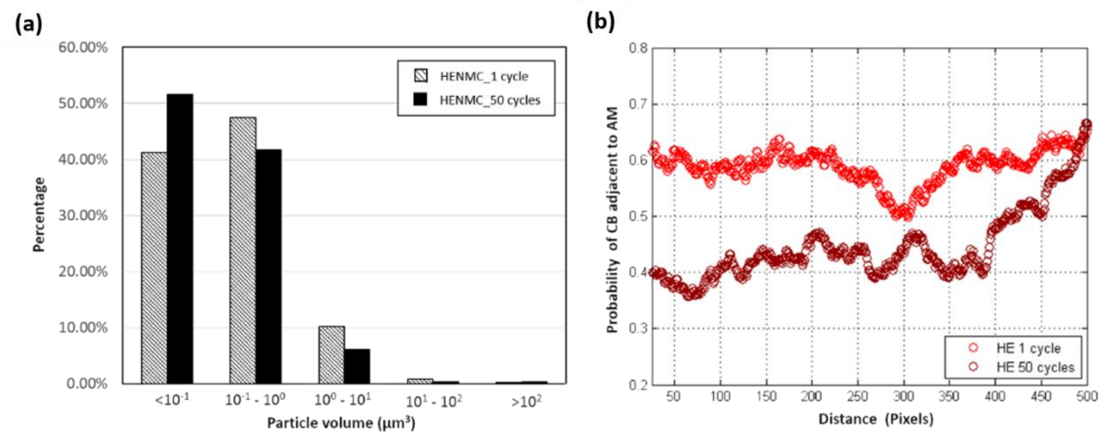

Figure 6.11 (a) Comparison of the particle size distribution of 1-cycle and 50-cycle HENMC cathodes from 3D reconstruction. (b) Comparison of PBA of 1-cycle and 50-cycle HENMC cathodes from 3D reconstruction.

The "neighbor counting" method was applied to the segmented 3D dataset of HENMC cathodes with different cycle numbers, and the PBA was calculated through the depth of the electrode, Figure 6.11b. Similar to the NMC samples, the PBA was calculated for each slice parallel to the separator and current collector across the depth of cathode. The averaged PBA of HENMC samples decreased from 0.60 at the first cycle to 0.46 after another 49 cycles. The 50-cycle HENMC electrode therefore shows a 22.5% decrease in AM and CB contact which is consistent with the PBA analysis on the NMC cathode. We note, however, that the cells were specifically cycled in harsh conditions over a large voltage window (2.0 V ~ 4.6 V) resulting in a dramatic ~ 45% loss in capacity (Figure 6.4). The significant PBA decrease is yet again correlated with the observed capacity fade, although we cannot exclude other factors evolving in parallel, i.e. undesired structural transformation and CEI layer formation that were revealed in Chapter 5. The PBA analysis of the HENMC electrode indicates that there would be a loss of electrical conductivity as a consequence of the detachment between the conductive binder matrix and active particles.

6.5 Conclusion

The 3D reconstruction of two types of lithium-ion battery cathode microstructures, NMC and HENMC, after different electrochemical cycling states were achieved using FIB-SEM combined with a refined segmentation algorithm without any epoxy resin infiltration. The particle size distribution analysis from the 3D reconstruction shows that the active particles in the NMC and HENMC cathodes exhibit no significant changes from the different cycling states. Measurements of the connectivity between active particles and binder phase of NMC cathode after electrochemical cycling were also carried out in order to assess the PBA, calculated with a “neighbor counting” method from 3D dataset. The results show significant decreases in PBA during cycling, revealing the loss of connectivity between the conductive CB and active particles. We noted a correlation between the drop in average PBA, indicative of detachment between the AM and CB phases, and cell capacity loss with increased number of cycles. Furthermore, detachment between the CB phase and AM is also discovered from the lab-made HENMC cathode after 50 cycles. These results thus suggest that the cycling-induced AM/CB detachment is a common trend regardless of the way that electrode is manufactured. In general, our findings show that the loss of electrical connectivity of the cathode, as inferred from the detachment between the phases, is one of the challenges in achieving and maintaining the high capacity and stable cycling performance of lithium-ion batteries.

Chapter 7

Conclusion

The work carried out in this thesis demonstrated the use of different electron microscopy techniques to investigate the degradation mechanisms of two types of layered structure cathode materials, aiming to unravel the possible mechanisms at the origin of performance deterioration of lithium-ion batteries. The structural changes and chemical evolutions of the layered cathodes were studied from the surface to the bulk of materials using state-of-the-art aberration-corrected TEM instrument equipped with a monochromator, therefore, enabling both high spatial resolution and energy resolution for the measurements. Meanwhile, the FIB-SEM sectioning and imaging technique provided the reconstruction of the 3D microstructure of lithium-ion battery cathodes, thus providing a more complete picture of the cathode degradation process.

In addition to demonstrate the charge transfer mechanism of TM cations in the NMC cathode, the inhomogeneous distribution of the electronic structure of TMs in NMC cathode material, from the surface to the bulk, were clearly revealed during the charge-discharge process using spatially-resolved STEM-EELS technique. Although bulk sensitive NMR indicated that the NMC bulk material maintains the Li-O-TM ordering, the TEM characterizations showed the formation of a surface reduction layer at NMC surface, which was associated with TM reduction to lower oxidation states. The particle surface transformed to a MO-type rock-salt phase (transition from $R\bar{3}m$ to $Fm\bar{3}m$) accompanied by lithium and oxygen loss during cycling. The results thus suggest that the surface degradation is initiated in the first charge process and continues in the subsequent cycles, which may contribute to the capacity fade and limit the charge transfer near the cathode surface, adversely influencing the cell performance.

Although the irreversible phase transformation and lithium and oxygen loss near the cathode surface have been revealed to be some of the reasons for the performance decay of lithium-ion battery from the study on NMC, the investigation on the HENMC cathode shows some differences in the degradation process. Unlike NMC cathodes that are stable in the bulk structure during cycling, the Li-rich HENMC cathodes not only suffer surface degradation (surface reconstruction and electrolyte decomposition at cathode-electrolyte interface), but also exhibits complexed changes in the bulk material. These include: (i) complete Li loss from TM layers accompanied with the bulk phase transformation ($C2/m$ solid-solution→$R\bar{3}m$); (ii) "nano-defect" domains arising from severe lattice distortions; (iii) and notably, formation of large-scale LiM_2O_4 (M=Mn, Co, Ni) spinel grains, with regions hundreds of nanometers across. The study uncovers the significant changes in the cathode internal structure, pointing out the main sources for the rapid capacity fade of Li-rich cathodes.

In addition to the 2D characterization, the 3D microstructural study performed on both pristine and cycled NMC and HENMC cathodes using FIB-SEM 3D reconstruction provided the spatial distribution of the three phases including active material, carbon-doped binder and pore spaces of the whole cathode. The results unravel the loss of connectivity between the active material and carbon-doped binder phases after cycling, suggesting a possible mechanism for cell deterioration.

The work carried out in this thesis unravels the initiation and development of degradation processes of layered cathode materials using complementary diagnostic tools. The results provide valuable insights into the origins of battery deterioration, shed light on the future design and modification of high-energy-density cathodes.

Chapter 8

Future Work

In the former chapters, we have shown the potential of TEM in the study of lithium-ion battery cathode materials. TEM is a powerful tool that can be used to analyze the electronic structure, composition, and crystallographic structure of the studied material. With the established characterization methods, more battery related materials can be investigated using TEM.

8.1 Study on Lithium-Rich Cathode

8.1.1 Investigation on the Role of Oxygen in Charge Transfer

The redox reaction of cathode materials during charge-discharge is critical to the capacity of lithium-ion batteries. It has been discussed in Chapter 3 that the lithium-rich cathode possesses abnormal high capacity, which is attributed to the participation of oxygen in the charge transfer process. As mentioned in section 3.5.1, DFT calculation predicted that the reactivity of the oxygen redox reaction relies on the existence of the Li-O-Li environment (Figure 3.17), whereas, no experimental data was presented. In order to understand the origins of the high-capacity of lithium-rich cathode, an in-depth understanding of the anionic redox reaction of oxygen during delithiaion-lithiation is important. Therefore, experiments can be designed to investigate the behavior of oxygen at different cyclic conditions using high-resolution EELS. To unravel if the Li-O-Li configuration is related with oxygen redox activity, (i) first, compare the O K-edge between the pristine HENMC and NMC cathode. We have obtained EELS data on the pristine HENMC and NMC cathode, which however, exhibit no obvious difference in the peak feature, as shown in Figure 8.1. This is in contradict with the calculated data reported in Ref 92, as extra oxygen states are predicted to be present due to the Li-O-Li configuration. (ii) Next, in order to further examine the proposed Li-O-Li configuration, the O K-edge features can be measured from the HENMC cathodes at different cyclic states. By comparing the O K-edge from different sets of charged samples, we can infer if the oxygen redox reaction occurs in particular environment.

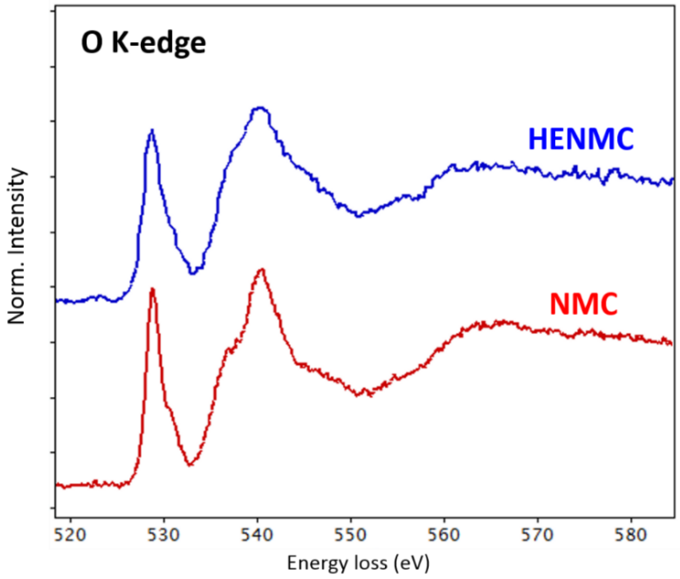

Figure 8.1 O K-edge spectra from pristine NMC and HENMC cathode materials.

Meanwhile, in order to further analyze the chemical and structural evolution during delithiation-lithiation and after extended cycling, a quasi in-situ experiment could be possibly designed as follows:

(i) a TEM sample of the cathode in the form of a thin slice needs to be prepared;

(ii) this small piece of cathode sample can be constructed into a electrochemical cell configuration, the cell will then be subjected to electrochemical cycling;

(iii) the cycled cathode sample will then be washed and dried in the glovebox, and transferred into TEM for further analysis.

From this experiment, the Li distribution within the cathode material during delithiation can be visualized using STEM-EELS technique. Meanwhile, the structural evolution can be studied in more details. The studied electrode sample can be either prepared from pristine state or after electrochemical cycling. This experimental design can also be applied to other electrode systems.

8.1.2 Study on the Evolution of Li-Rich Cathode during Cycling

As mentioned in Chapter 5, the significant bulk evolutions, in addition to the surface degradation, have been well recognized from the study on HENMC. With this knowledge on the degradation process, the structural analysis using aberration-corrected TEM can be carried on to another Li-rich cathode material. The Li-rich cathodes that undergo different number of cycles will be characterized, including long-term cycled cathode. In such case, the degradation process of Li-rich cathode can be further analyzed following extended numbers of electrochemical cycles. This also provides another chance to continue the investigation on the layered-to-spinel transition. Both the chemical evolution and phase transformation of the cycled Li-rich cathodes will be analyzed using EELS and atomic-resolution HAADF-STEM imaging techniques.

8.2 Study on the Surface Evolution of $LiMn_2O_4$ Cathode

As it has been shown in the study on NMC cathode material, with the usage of vacuum transfer holder and STEM-EELS technique, the electronic structure of the cathode material from surface to bulk at different state of charges (SOCs) can be clearly resolved. Using this established method, we can carry out investigations of the oxidation state to other types of cathode materials. The spinel $LiMn_2O_4$ (LMO) cathode is known to suffer Mn dissolution during cycling, therefore, the surface chemistry of LMO cathode is important in understanding this process. In this work, LMO cathode at different charge and discharge states will be analyzed. Using STEM-EELS, changes in the oxidation state of the Mn cations from the surface to the bulk of the LMO particles can be resolved and analyzed.

8.3 Study on the SEI Layer Formation

FIB-SEM has the power of synchronized milling and imaging, with this technique, the SEI layer formation on the electrode surface and the thickness variation of this surface layer under different cycling conditions can be analyzed. LMO-graphite cells using different separators exhibit great differences in the interfacial resistances of the electrodes. The cells with plain (Celgard 2500) separator show a much higher internal resistances than the cells using multifunctional separator. Therefore, in order to understand the origin for the increased resistances, the measurement of surface SEI layer on the electrodes from different cell configurations need to be carried out.

From preliminary SEM characterization of graphite anodes, significant differences have been observed between the pristine and cycled graphite anodes. Although the SEM images indicate the existence of the SEI layer on the anode surface, it is impossible to evaluate the thickness of the SEI layer from these top view images. Further FIB-SEM cross-sectional analysis is hence necessary in order to compare the thickness of the SEI layer from the anodes cycled in difference cell configurations.

8.4 Investigation on All-Solid-State Battery

Currently, great attention has been drawn to the development of all-solid-state lithium-ion batteries. The design of high-voltage and high-capacity cathodes can improve the energy density of lithium-ion batteries, however, the application of these high-energy-density cathodes are thwarted by many limiting factors. One of a major concern is the narrow operating voltage window of the conventional liquid electrolytes. The carbonate-based electrolytes become unstable above 4.3V operation voltage and will decompose and oxidize during electrochemical cycling, these flammable organic solvents thus generate serious safety concerns. The application of solid-state electrolyte in lithium-ion battery system can improve the safety of batteries. Meanwhile, the usage of solid-state electrolyte may prevent the lithium dendrite formation and the undesired consequences, therefore, leading to the possibility of introducing metallic lithium into the battery system. However, these all-solid-state batteries suffer major drawbacks of low ionic conductivity of the solid-state electrolyte and large interfacial resistance between the electrode and electrolyte.

Therefore, the application of TEM technique into the study of solid-state battery system would provide valuable insights into the development of all-solid-state lithium-ion batteries. The in-situ TEM technique can be applied to the direct observation of lithium transport in the solid-state electrolyte and electrode-electrolyte interface, which is of great relevance for understanding the charge transfer characteristics of the developed solid-state electrolyte. The exclusion of liquid electrolyte from in-situ experiment enables better EELS measurements since the sample thickness can be better controlled and limited. Thus, the spatial resolution may also be improved because of the reduced sample thickness. Meanwhile, characterization of the chemical and structural changes at the electrode-electrolyte interface during charge-discharge using TEM can provide useful information on the electrode-electrolyte interfacial structure and contact. There has already been a TEM study that identified the formation of structurally disordered interfacial layer between the cathode and electrolyte.[222] Hence, one of the future directions of TEM work in the field of lithium-ion battery materials could be the investigation of solid-state battery systems.

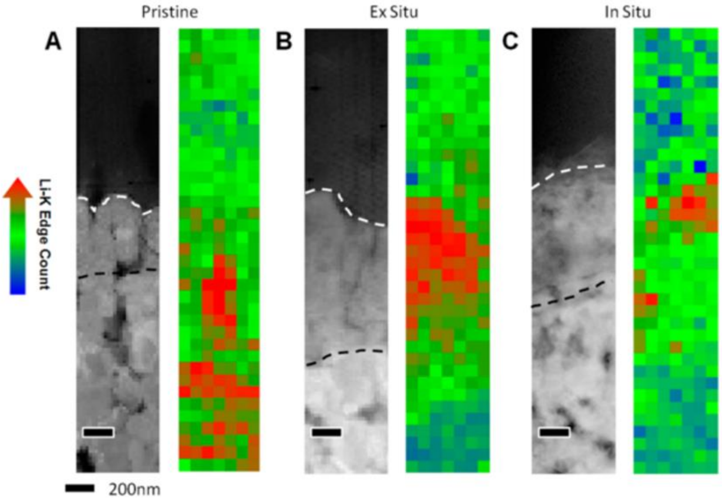

Figure 8.2 STEM-EELS characterization of $LiCoO_2$/LiPON/Si thin film battery. HAADF images and Li EELS maps of (a) pristine nanobattery; (b) ex-situ charged nanobattery at 4.2 V; (c) in-situ charged nanobattery at 4.2 V. From reference [222].

Appendix I

Multiple Linear Least Square fitting for EELS spectrum

The multiple linear least square method (MLLS) fits the reference spectra and/or models to a specified energy range of the selected spectrum. A model function consisting linear combination of the specified reference spectra will be formed and used to fit the spectrum acquired from the experiment, a general model equation as shown below:

$$\mathbf{S}(\mathrm{E}) = \beta_1 \, \mathrm{A}E^{-r} + \beta_2 \mathbf{S}(\mathrm{E})_{\mathrm{I}} + \beta_3 \mathbf{S}(\mathrm{E})_{\mathrm{II}} + \boldsymbol{\varepsilon}$$

β_1: fitting coefficient for background function with preset AE^{-r}

β_2: fitting coefficient for reference spectrum 1 (Mn^{2+}, Co^{2+} and Ni^{2+}, respectively)

β_3: fitting coefficient for reference spectrum 2 (Mn^{4+}, Co^{3+}, and $Ni^{3+/4+}$, respectively)

ε: the sum of squared residuals.

The fitting coefficient "β" will be adjusted to minimize the squared residuals "ε" between the linear fitted model and the selected spectrum. If correctly performed, the fit coefficient can be interpreted as the relative contribution of each reference spectrum or the contribution maps with the same dimensionality of the input spectrum image.

In our case, the reference spectra of Ni, Mn and Co used for the fitting were directly extracted from the experimental EELS spectrum image (SI). The fit coefficient maps represent the relative contribution of the two reference spectra (which representing the two valence states of the TM element) at each pixel from the entire SI, therefore reflect the valence distribution in the sample. Thus, fitting coefficient maps are named as valence maps.

Appendix II

Representative Volume Evaluation for 3D Reconstruction

In order to test the effectiveness of the volume size, we compared the volume ratio of AM to CB phases from the obtained 3D dataset with the area ratio of AM to CB from 2D large cross-sections along different depth of cathode film.

1. For the commercial NMC cathode, due to the lack of independent knowledge of the composition, we can only evaluate the sample homogeneity by comparing the variation between different regions. First, we calculated the volume ratio of AM to CB from the 3D dataset of pristine NMC cathode and this is equal to 2.88. Then, we took a large 2D cross-section with a width of 20μm and covering ~60μm depth of the cathode (nearly the full depth of the NMC cathode film) and segmented the image into the three phases. The area ratio AM to CB calculated from the large 2D slice is 2.89, which is practically identical to what we obtained from the 3D volume. Then the 2D slice was separated into three sections (the depth of the 3D volume is about 18μm, which is similar with each 2D section) from top to bottom, the AM/CB ratio at different depth and the corresponding variation from the 3D volume fraction is listed below:

Top: $\frac{\mathrm{AM}}{\mathrm{CB}} = 2.71$, variation with respect to the 3D volume fraction measurement: -5.9%;

Middle: $\frac{\mathrm{AM}}{\mathrm{CB}} = 3.01$, variation with respect to the 3D volume fraction measurement: 4.2%;

Bottom: $\frac{\mathrm{AM}}{\mathrm{CB}} = 2.97$, variation with respect to the 3D volume fraction measurement: 2.8%.

The above comparison indicates that the variation of phase distribution in NMC cathode is not significant with the evaluated sampling size ($< \pm 6\%$). Therefore, the 3D volume used in this study should be representative of the cathode structure.

2. For the HENMC, we have used the composition of our lab-scale HENMC electrode as a validation test. This lab-scale electrode has the weight ratio of 80:10:10 (active material: PVDF: carbon). The density for each component is 4.4 g/cc, 1.78 g/cc, and 1.98 g/cc, respectively. With this prior knowledge on the material we produced, we calculated the expected volume fraction for each component and this is 63%, 19% and 18% for the active material, PVDF and carbon respectively. If we combine the carbon and binder volume, the volume ratio between active material and carbon/binder is expected to be

$$\text{AM to CB ratio} = \frac{\text{AM}}{\text{CB}} = \frac{63\%}{37\%} = 1.71$$

The volume ratio of AM to CB calculated from the 3D dataset of single cycled HENMC cathode in this study is 1.81, which shows only about 5.8% variation from the nominal ratio. To validate the sampling volume, we obtained again a large 2D cross-section image covering 80μm depth of the cathode (nearly the full depth of the cathode film). We then compared the area ratio of AM and CB at different depths (the depth of 3D volume is about 23μm) to evaluate the phase distribution along the depth of the cathode. The ratio and the corresponding variation between the experimental data and calculated value (expected from the synthesis parameters as calculated above: 1.71) is listed below:

Top: $\frac{\text{AM}}{\text{CB}} = 1.75$, variation from the calculated value: 2.3%;

Middle: $\frac{\text{AM}}{\text{CB}} = 1.82$, variation from the calculated value: 6.4%;

Bottom: $\frac{\text{AM}}{\text{CB}} = 1.63$, variation from the calculated value: -4.7%.

The variation of phase distribution in HE-NMC cathode with the evaluated sampling size is not significant, all within the range of $\pm 7\%$. Therefore, we believe that the 3D volume size of HENMC cathode in this study is considered to be sufficient.

References

[1] D. J. Lockwood, *Nanotechnology for Lithium-Ion Batteries*, **2013**.

[2] D. Larcher, S. Beattie, M. Morcrette, K. Edström, J.-C. Jumas, J.-M. Tarascon, *J. Mater. Chem.*, **2007**, *17*, 3759.

[3] Y. Qi, S. J. Harris, *J. Electrochem. Soc.*, **2010**, *157*, A741.

[4] K. E. Aifantis, S. A. Hackney, R. V. Kumar, *High Energy Density Lithium Batteries,* Wiley-VCH, **2010**.

[5] C A Vincent, B. Scrosati, *Modern Batteries,* Butterworth-Heinemann, **1997**.

[6] T. B. Reddy, *Linden's Handbook of Batteries,* McGraw-Hill Education, **2011**.

[7] M. S. Whittingham, *Science*, **1976**, *192*, 1126.

[8] D. W. Murphy, F. J. Di Salvo, J. N. Carides, J. V. Waszczak, *Mater. Res. Bull.*, **1978**, *13*, 1395.

[9] B. Lazzari, M. Scrosati, *J. Electrochem. Soc.*, **1980**, *127*, 773.

[10] J. B. Goodenough, K. Mizuchima, *U. S. Pate*nt, **1981,** *4302518.*

[11] J. M. Tarascon, M. Armand, *Nature* **2001**, *414*, 359.

[12] S. Patoux, L. Sannier, H. Lignier, Y. Reynier, C. Bourbon, S. Jouanneau, F. Le Cras, S. Martinet, *Electrochim. Acta* **2008**, *53*, 4137.

[13] B. Dunn, H. Kamath, J.-M. Tarascon, *Science* **2011**, *334*, 928.

[14] C. Mikolajczak, M. Kahn, K. White, R. T. Long, *Lithium-Ion Batteries Hazard and Use Assessment*, Springer, **2011**.

[15] J.-K. Park, *Principles and Applications of Lithium Seconary Batteries*, Wiley-VCH, **2012**.

[16] J. Li, C. Ma, M. Chi, C. Liang, N. J. Dudney, *Adv. Energy Mater.* **2015**, *5*, 1401408.

[17] Z. Wang, J. Z. Lee, H. L. Xin, L. Han, N. Grillon, D. Guy-bouyssou, E. Bouyssou, M. Proust, Y. S. Meng, *J. Power Sources* **2016**, *324*, 342.

[18] D. Chung, E. Elgqvist, S. Santhanagopalan, *Automotive Lithium-Ion Cell Manufacturing: Regional Cost Structures and Supply Chain Considerations,* Technical report, **2016**,

[19] J. M. F. Rodríguez, J. Morales, J. L. Tirado, *React. Solids* **1987**, *4*, 163.

[20] D. R. Diercks, M. Musselman, A. Morgenstern, T. Wilson, M. Kumar, K. Smith, M. Kawase, B. P. Gorman, M. Eberhart, C. E. Packard, *J. Electrochem. Soc.* **2014**, *161*, F3039.

[21] J. R. Dahn, U. Vonsacken, M. W. Juzkow, H. Aljanaby, *J. Electrochem. Soc.* **1991**, *138*, 2207.

[22] T. Ohzuku, A. Ueda, M. Nagayama, *J. Electrochem. Soc.* **1993**, *140*, 1862.

[23] P. G. Bruce, A. R. Armstrong, R. L. Gitzendanner, *J. Mater. Chem.* **1999**, *9*, 193.

[24] J. N. Reimers, J. R. Dahn, *J. Electrochem. Soc.* **1992**, *139*, 2091.

[25] R. Kanno, H. Kubo, Y. Kawamoto, T. Kamiyama, F. Izumi, Y. Takeda, M. Takano, *J. Solid State Chem.* **1994**, *110*, 216.

[26] J. R. Dahn, E. W. Fuller, M. Obrovac, U. von Sacken, *Solid State Ionics* **1994**,

69, 265.

[27] A. R. Armstrong, P. G. Bruce, *Nature* **1996**, *381*, 499.

[28] G. Vitins, K. West, *J. Electrochem. Soc.* **1997**, *144*, 2587.

[29] N. Yabuuchi, T. Ohzuku, *J. Power Sources* **2003**, *119–121*, 171.

[30] I. Belharouak, Y. K. Sun, J. Liu, K. Amine, *J. Power Sources* **2003**, *123*, 247.

[31] M. Noh, J. Cho, *J. Electrochem. Soc.* **2013**, *160*, A105.

[32] J. Xiao, N. A. Chernova, M. S. Whittingham, *Chem. Mater.* **2008**, *20*, 7454.

[33] K. M. Shaju, P. G. Bruce, *Adv. Mater.* **2006**, *18*, 2330.

[34] J. Li, J. Camardese, R. Shunmugasundaram, S. Glazier, Z. Lu, J. R. Dahn, *Chem. Mater.* **2015**, *27*, 3366.

[35] Y. Koyama, I. Tanaka, H. Adachi, Y. Makimura, T. Ohzuku, *J. Power Sources* **2003**, *119–121*, 644.

[36] H. Liu, M. Bugnet, M. Z. Tessaro, K. J. Harris, M. J. R. Dunham, M. Jiang, G. R. Goward, G. A. Botton, *Phys. Chem. Chem. Phys.* **2016**, *18*, 29064.

[37] N. Yabuuchi, K. Yoshii, S. T. Myung, I. Nakai, S. Komaba, *J. Am. Chem. Soc.* **2011**, *133*, 4404.

[38] C. S. Johnson, N. Li, C. Lefief, M. M. Thackeray, *Electrochem. commun.* **2007**, *9*, 787.

[39] C. S. Johnson, N. Li, C. Lefief, J. T. Vaughey, M. M. Thackeray, *Chem. Mater.* **2008**, *20*, 6095.

[40] F. Lin, I. M. Markus, D. Nordlund, T.-C. Weng, M. D. Asta, H. L. Xin, M. M. Doeff, *Nat. Commun.* **2014**, *5*, 3529.

[41] D. Kim, S. Park, O. B. Chae, J. H. Ryu, Y.-U. Kim, R.-Z. Yin, S. M. Oh, *J. Electrochem. Soc.* **2012**, *159*, A193.

[42] J. Zheng, M. Gu, A. Genc, J. Xiao, P. Xu, X. Chen, Z. Zhu, W. Zhao, L. Pullan, C. Wang, J. G. Zhang, *Nano Lett.* **2014**, *14*, 2628.

[43] B. Ellis, K. Lee, L. Nazar, *Chem. Mater.* **2010**, *22*, 691.

[44] Y. Shao-Horn, S. A. Hackney, A. J. Kahaian, K. D. Kepler, E. Skinner, J. T. Vaughey, M. M. Thackeray, *J. Power Sources* **1999**, *81–82*, 496.

[45] B. Deng, H. Nakamura, M. Yoshio, *J. Power Sources* **2008**, *180*, 864.

[46] D. T. Murphy, S. Schmid, J. R. Hester, P. E. R. Blanchard, W. Miiller, *Inorg. Chem.* **2015**, *54*, 4636.

[47] K. Petrov, R. M. Rojas, P. J. Alonso, J. M. Amarilla, M. G. Lazarraga, J. M. Rojo, *Solid State Sci.* **2005**, *7*, 277.

[48] M. Lee, S. Lee, P. Oh, Y. Kim, J. Cho, *Nano Lett.* **2013**, *14*, 993.

[49] B. L. Ellis, K. T. Lee, L. F. Nazar, *Chem. Mater.* **2010**, *22*, 691.

[50] J. Lu, C. Zhan, T. Wu, J. Wen, Y. Lei, A. J. Kropf, H. Wu, D. J. Miller, J. W. Elam, Y.-K. Sun, X. Qiu, K. Amine, *Nat. Commun.* **2014**, *5*, 5693.

[51] A. Jarry, S. Gottis, Y.-S. Yu, J. Roqué-Rosell, C. Kim, J. Cabana, J. Kerr, R. Kostecki, *J. Am. Chem. Soc.* **2015**, *137*, 3533.

[52] A. K. Padhi, K. S. Nanjundaswamy, J. B. Goodenough, *J. Electrochem. Soc.* **1997**, *144*,1188.

[53] S.-Y. Chung, J. T. Bloking, Y.-M. Chiang, *Nat. Mater.* **2002**, *1*, 123.

[54] S. W. Oh, S. T. Myung, S. M. Oh, K. H. Oh, K. Amine, B. Scrosati, Y. K. Sun,

Adv. Mater. **2010**, *22*, 4842.

[55] Z. Xiao, Y. Zhang, G. Hu, *J. Appl. Electrochem.* **2014**, *45*, 225.

[56] B. Sun, Y. Wang, B. Wang, H.-S. Kim, W.-S. Kim, G. Wang, *J. Nanosci. Nanotechnol.* **2013**, *13*, 3655.

[57] I. Bilecka, A. Hintennach, M. D. Rossell, D. Xie, P. Novák, M. Niederberger, *J. Mater. Chem.* **2011**, *21*, 5881.

[58] C. Sun, S. Rajasekhara, J. B. Goodenough, F. Zhou, *J. Am. Chem. Soc.* **2011**, *133*, 2132.

[59] M.-H. Lee, J.-Y. Kim, H.-K. Song, *Chem. Commun.* **2010**, *46*, 6795.

[60] I. Nakai, *Electrochem. Solid-State Lett.* **1999**, *1*, 259.

[61] J. M. Rosolen, M. Abbate, *Solid State Ionics*, **2001**, *139*, 83.

[62] L. A. Montoro, M. Abbate, J. M. Rosolen, *J. Electrochem. Soc.* **2000**, *147*, 1651.

[63] L. A. Montoro, J. M. Rosolen, *Electrochim. Acta* **2004**, *49*, 3243.

[64] W.-S. Yoon, M. Balasubramanian, X.-Q. Yang, Z. Fu, D. a. Fischer, J. McBreen, *J. Electrochem. Soc.* **2004**, *151*, A246.

[65] M. Jiang, B. Key, Y. S. Meng, C. P. Grey, *Chem. Mater.* **2009**, *21*, 2733.

[66] C. P. Grey, N. Dupré, *Chem. Rev.* **2004**, *104*, 4493.

[67] A. Ueda, T. Ohzuku, *J. Electrochem. Soc.* **1994**, *141*, 2010.

[68] J. M. Paulsen, J. R. Mueller-Neuhaus, J. R. Dahn, *J. Electrochem. Soc.* **2000**, *147*, 508.

[69] A. R. Armstrong, M. Holzapfel, P. Novák, C. S. Johnson, S.-H. Kang, M. M. Thackeray, P. G. Bruce, *J. Am. Chem. Soc.* **2006**, *128*, 8694.

[70] D. W. Shin, C. A. Bridges, M. P. Paranthaman, A. Manthiram, *Chem. Mater.* **2012**, *24*, 3720.

[71] D. Chen, S. Indris, M. Schulz, B. Gamer, R. Mönig, *J. Power Sources* **2011**, *196*, 6382.

[72] A. Ito, K. Shoda, Y. Sato, M. Hatano, H. Horie, Y. Ohsawa, *J. Power Sources* **2011**, *196*, 4785.

[73] S. Zheng, R. Huang, Y. Makimura, Y. Ukyo, C. a. J. Fisher, T. Hirayama, Y. Ikuhara, *J. Electrochem. Soc.* **2011**, *158*, A357.

[74] D. B. Williams, C. B. Carter, *Transmission Electron Microscopy*, Springer, **2009**.

[75] G. Botton, *Analytical Electron Microscopy,* Springer, **2007**.

[76] R. F. Egerton, *Electron Energy-Loss Spectroscopy in the Electron Microscope*, Springer, **2011**.

[77] A. Deb, U. Bergmann, S. P. Cramer, E. J. Cairns, *J. Appl. Phys.* **2006**, *99*, 63701.

[78] M. S. Islam, R. A. Davies, J. D. Gale, *Chem. Mater.* **2003**, *15*, 4280.

[79] J. Stöhr, *NEXAFS Spectroscopy,* Springer, **1992**.

[80] J. G. Chen, *Surf. Sci. Rep.* **1997**, *30*, 1.

[81] J. M. Kim, H. T. Chung, *Electrochim. Acta* **2004**, *49*, 937.

[82] M. G. Kim, H. J. Shin, J.-H. Kim, S.-H. Park, Y.-K. Sun, *J. Electrochem. Soc.* **2005**, *152*, A1320.

[83] W. Yoon, M. Balasubramanian, K. Y. Chung, X. Yang, J. Mcbreen, C. P. Grey, D. A. Fischer, *J. Am. Chem. Soc.* **2005**, *127*, 17479.

[84] S. Miao, M. Kocher, P. Rez, B. Fultz, Y. Ozawa, R. Yazami, C. C. Ahn, *J. Phys. Chem. B* **2005**, *109*, 23473.

[85] Z. Q. Deng, A. Manthiram, *J. Phys. Chem. C* **2011**, *115*, 7097.

[86] M. M. Thackeray, S.-H. Kang, C. S. Johnson, J. T. Vaughey, R. Benedek, S. a. Hackney, *J. Mater. Chem.* **2007**, *17*, 3112.

[87] Z. Chen, Z. Lu, J. R. Dahn, *J. Electrochem. Soc.* **2002**, *149*, A1604.

[88] H. Koga, L. Croguennec, M. Ménétrier, P. Mannessiez, F. Weill, C. Delmas, *J. Power Sources* **2013**, *236*, 250.

[89] A. Ito, Y. Sato, T. Sanada, M. Hatano, H. Horie, Y. Ohsawa, *J. Power Sources* **2011**, *196*, 6828.

[90] E. McCalla, A. M. Ahakumov, M. Saubanere, D. Foix, E. J. Berg, G. Rousse, M.-L. Doublet, D. Gonbeau, P. Novak, G. Van Tendeloo, R. Dominko, J.-M. Tarascon, *Science* **2015**, *350*, 1516.

[91] K. Luo, M. R. Roberts, R. Hao, N. Guerrini, D. M. Pickup, Y.-S. Liu, K. Edström, J. Guo, A. V. Chadwick, L. C. Duda, P. G. Bruce, *Nat. Chem.* **2016**, *8*, 684.

[92] D. Seo, J. Lee, A. Urban, R. Malik, S. Kang, G. Ceder, *Nat. Chem.* **2016**, *8*, 692.

[93] L. Terborg, S. Weber, F. Blaske, S. Passerini, M. Winter, U. Karst, S. Nowak, *J. Power Sources* **2013**, *242*, 832.

[94] M. B. Pinson, M. Z. Bazant, *J. Electrochem. Soc.* **2013**, *160*, A243.

[95] K. Y. Chung, W. S. Yoon, K. B. Kim, B. W. Cho, X. Q. Yang, *J. Appl. Electrochem.* **2011**, *41*, 1295.

[96] M. Balasubramanian, H. S. Lee, X. Sun, X. Q. Yang, A. R. Moodenbaugh, J. McBreen, D. a. Fischer, Z. Fu, *Electrochem. Solid-State Lett.* **2002**, *5*, A22.

[97] P. Verma, P. Maire, P. Novák, *Electrochim. Acta* **2010**, *55*, 6332.

[98] K. Edström, T. Gustafsson, J. O. Thomas, *Electrochim. Acta* **2004**, *50*, 397.

[99] S. Malmgren, K. Ciosek, M. Hahlin, T. Gustafsson, M. Gorgoi, H. Rensmo, K. Edström, *Electrochim. Acta* **2013**, *97*, 23.

[100] H. Shin, J. Park, A. M. Sastry, W. Lu, *J. Power Sources* **2015**, *284*, 416.

[101] E. Peled, D. Bar Tow, A. Merson, A. Gladkich, L. Burstein, D. Golodnitsky, *J. Power Sources* **2001**, *97–98*, 52.

[102] X. Xiao, Z. Liu, L. Baggetto, G. M. Veith, K. L. More, R. R. Unocic, *Phys. Chem. Chem. Phys.* **2014**, *16*, 10398.

[103] S. K. Martha, J. Nanda, G. M. Veith, N. J. Dudney, *J. Power Sources* **2012**, *216*, 179.

[104] J. Vetter, P. Novák, M. R. Wagner, C. Veit, K. C. Möller, J. O. Besenhard, M. Winter, M. Wohlfahrt-Mehrens, C. Vogler, A. Hammouche, *J. Power Sources* **2005**, *147*, 269.

[105] D. S. Eastwood, V. Yufit, J. Gelb, A. Gu, R. S. Bradley, S. J. Harris, D. J. L. Brett, N. P. Brandon, P. D. Lee, P. J. Withers, P. R. Shearing, *Adv. Energy Mater.* **2014**, *4*, 1300506.

[106] B. Xu, C. R. Fell, M. Chi, Y. S. Meng, *Energy Environ. Sci.* **2011**, *4*, 2223.

[107] S. M. Bak, K. W. Nam, W. Chang, X. Yu, E. Hu, S. Hwang, E. A. Stach, K. B. Kim, K. Y. Chung, X. Q. Yang, *Chem. Mater.* **2013**, *25*, 337.

[108] K.-W. Nam, S.-M. Bak, E. Hu, X. Yu, Y. Zhou, X. Wang, L. Wu, Y. Zhu, K.-Y. Chung, X.-Q. Yang, *Adv. Funct. Mater.* **2013**, *23*, 1047.

[109] P. K. Nayak, J. Grinblat, M. Levi, Y. Wu, B. Powell, D. Aurbach, *J. Electroanal. Chem.* **2014**, *733*, 6.

[110] L. Wu, K. W. Nam, X. Wang, Y. Zhou, J. C. Zheng, X. Q. Yang, Y. Zhu, *Chem. Mater.* **2011**, *23*, 3953.

[111] D. P. Abraham, R. D. Twesten, M. Balasubramanian, J. Kropf, D. Fischer, J. McBreen, I. Petrov, K. Amine, *J. Electrochem. Soc.* **2003**, *150*, A1450.

[112] S.-K. Jung, H. Gwon, J. Hong, K.-Y. Park, D.-H. Seo, H. Kim, J. Hyun, W. Yang, K. Kang, *Adv. Energy Mater.* **2013**, *4*, 1300787.

[113] S. Hwang, W. Chang, S. M. Kim, D. Su, D. H. Kim, J. Y. Lee, K. Y. Chung, E. A. Stach, *Chem. Mater.* **2014**, *26*, 1084.

[114] S. Hwang, S. M. Kim, S. M. Bak, B. W. Cho, K. Y. Chung, **2015**, *2*, 503278.

[115] S. Hwang, S. M. Kim, S. M. Bak, S. Y. Kim, B. W. Cho, K. Y. Chung, J. Y. Lee, E. A. Stach, W. Chang, *Chem. Mater.* **2015**, *27*, 3927.

[116] J. Zheng, M. Gu, J. Xiao, P. Zuo, C. Wang, J.-G. Zhang, *Nano Lett.* **2013**, *13*, 3824.

[117] F. Amalraj, M. Talianker, B. Markovsky, L. Burlaka, N. Leifer, G. Goobes, E. M. Erickson, O. Haik, J. Grinblat, E. Zinigrad, D. Aurbach, J. K. Lampert, J.-Y. Shin, M. Schulz-Dobrick, A. Garsuch, *J. Electrochem. Soc.* **2013**, *160*, A2220.

[118] S.-H. Kang, Y. K. Sun, K. Amine, *Electrochem. Solid-State Lett.* **2003**, *6*, A183.

[119] M. M. Thacheray, C. S. Johnson, J. T. Vaughey, N. Li, S. A. Hackney, *J. Mater. Chem.* **2005**, *15*, 2257.

[120] H. Yu, H. Zhou, *J. Mater. Chem.* **2012**, *22*, 15507.

[121] Q. Y. Wang, J. Liu, A. V. Murugan, A. Manthiram, *J. Mater. Chem.* **2009**, *19*, 4965.

[122] C. H. Lei, J. Bareño, J. G. Wen, I. Petrov, S. H. Kang, D. P. Abraham, *J. Power Sources* **2008**, *178*, 422.

[123] Y. S. Meng, G. Ceder, C. P. Grey, W.-S. Yoon, M. Jiang, J. Bréger, Y. Shao-Horn, *Chem. Mater.* **2005**, *17*, 2386.

[124] D. Mohanty, E. A. Payzant, A. S. Sefat, J. Li, D. P. Abraham, D. L. Wood, C. Daniel, *Chem. Mater.* **2013**, *25*, 4064.

[125] M. M. Thackeray, S.-H. Kang, C. S. Johnson, J. T. Vaughey, R. Benedek, S. a. Hackney, *J. Mater. Chem.* **2007**, *17*, 3112.

[126] M. M. Thackeray, S. H. Kang, C. S. Johnson, J. T. Vaughey, S. A. Hackney, *Electrochem. commun.* **2006**, *8*, 1531.

[127] S.-H. Kang, P. Kempgens, S. Greenbaum, A. J. Kropf, K. Amine, M. M. Thackeray, *J. Mater. Chem.* **2007**, *17*, 2069.

[128] X. Yu, Y. Lyu, L. Gu, H. Wu, S. M. Bak, Y. Zhou, K. Amine, S. N. Ehrlich, H. Li, K. W. Nam, X. Q. Yang, *Adv. Energy Mater.* **2014**, *4*, 1300950.

[129] H. Yu, R. Ishikawa, Y.-G. So, N. Shibata, T. Kudo, H. Zhou, Y. Ikuhara, *Angew. Chemie Int. Ed.* **2013**, *52*, 5969.

[130] D. Kim, J. Gim, J. Lim, S. Park, J. Kim, *Mater. Res. Bull.* **2010**, *45*, 252.

[131] J.-S. Kim, C. S. Johnson, J. T. Vaughey, M. M. Thackeray, S. A. Hackney, W. Yoon, C. P. Grey, *Chem. Mater.* **2004**, *16*, 1996.

[132] Z. Lu, D. D. MacNeil, J. R. Dahn, *Electrochem. Solid-State Lett.* **2001**, *4*, A191.

[133] K. A. Jarvis, Z. Deng, L. F. Allard, A. Manthiram, P. J. Ferreira, *Chem. Mater.* **2011**, *23*, 3614.

[134] K. A. Jarvis, Z. Deng, L. F. Allard, A. Manthiram, P. J. Ferreira, *J. Mater. Chem.* **2012**, *22*, 11550.

[135] A. K. Shukla, Q. M. Ramasse, C. Ophus, H. Duncan, F. Hage, G. Chen, *Nat. Commun.* **2015**, *6*, 8711.

[136] Z. Lu, J. R. Dahn, *J. Electrochem. Soc.* **2002**, *149*, A815.

[137] F. La Mantia, F. Rosciano, N. Tran, P. Novák, *J. Appl. Electrochem.* **2008**, *38*, 893.

[138] C. R. Fell, D. Qian, K. J. Carroll, M. Chi, J. L. Jones, Y. S. Meng, *Chem. Mater.* **2013**, *25*, 1621.

[139] N. Tran, L. Croguennec, M. Ménétrier, F. Weill, P. Biensan, C. Jordy, C. Delmas, *Chem. Mater.* **2008**, *20*, 4815.

[140] A. Boulineau, L. Simonin, J. F. Colin, C. Bourbon, S. Patoux, *Nano Lett.* **2013**, *13*, 3857.

[141] A. Boulineau, L. Simonin, J.-F. Colin, E. Canévet, L. Daniel, S. Patoux, *Chem. Mater.* **2012**, *24*, 3558.

[142] M. Bettge, Y. Li, K. Gallagher, Y. Zhu, Q. Wu, W. Lu, I. Bloom, D. P. Abraham, *J. Electrochem. Soc.* **2013**, *160*, A2046.

[143] F. Dogan, J. R. Croy, M. Balasubramanian, M. D. Slater, H. Iddir, C. S. Johnson, J. T. Vaughey, B. Key, *J. Electrochem. Soc.* **2015**, *162*, A235.

[144] K. G. Gallagher, J. R. Croy, M. Balasubramanian, M. Bettge, D. P. Abraham, A. K. Burrell, M. M. Thackeray, *Electrochem. commun.* **2013**, *33*, 96.

[145] C. H. Shen, Q. Wang, F. Fu, L. Huang, Z. Lin, S. Y. Shen, H. Su, X. M. Zheng, B.-B. Xu, J. T. Li, S.-G. Sun, *ACS Appl. Mater. Interfaces* **2014**, *6*, 5516.

[146] P. Yan, A. Nie, J. Zheng, Y. Zhou, D. Lu, X. Zhang, R. Xu, I. Belharouak, X. Zu, J. Xiao, K. Amine, J. Liu, F. Gao, R. Shahbazian-Yassar, J.-G. Zhang, C.-M. Wang, *Nano Lett.* **2015**, *15*, 514.

[147] P. Y. Liao, J. G. Duh, J. F. Lee, H. S. Sheu, *Electrochim. Acta* **2007**, *53*, 1850.

[148] J. Hong, D.-H. Seo, S.-W. Kim, H. Gwon, S.-T. Oh, K. Kang, *J. Mater. Chem.* **2010**, *20*, 10179.

[149] B. Song, Z. Liu, M. O. Lai, L. Lu, *Phys. Chem. Chem. Phys.* **2012**, *14*, 12875.

[150] D. Mohanty, J. Li, D. P. Abraham, A. Huq, E. A. Payzant, D. L. Wood, C. Daniel, *Chem. Mater.* **2014**, *26*, 6272.

[151] A. Boulineau, L. Simonin, J.-F. Colin, C. Bourbon, S. Patoux, *Nano Lett.* **2013** *13*, 3857.

[152] J. Zheng, M. Gu, J. Xiao, B. J. Polzin, P. Yan, X. Chen, C. Wang, J. Zhang, *Chem. Mater.* **2014**, *26*, 6320.

[154] M. Gu, I. Belharouak, J. Zheng, H. Wu, J. Xiao, A. Genc, K. Amine, S. Thevuthasan, D. R. Baer, J. G. Zhang, N. D. Browning, J. Liu, C. Wang, *ACS Nano* **2013**, *7*, 760.

[155] C. Zhan, J. Lu, A. J. Kropf, T. Wu, A. N. Jansen, Y.-K. Sun, X. Qiu, K. Amine, *Nat. Commun.* **2013**, *4*, 2437.

[156] P. Niehoff, M. Winter, *Langmuir* **2013**, *29*, 15813.

[157] T. Zhao, S. Chen, R. Chen, L. Li, X. Zhang, M. Xie, F. Wu, *ACS Appl. Mater. Interfaces*, **2014**, *6*, 21711.

[158] S. K. Martha, J. Nanda, Y. Kim, R. R. Unocic, S. Pannala, N. J. Dudney, *J. Mater. Chem. A* **2013**, *1*, 5587.

[159] F. Wu, N. Li, Y. Su, L. Zhang, L. Bao, J. Wang, L. Chen, Y. Zheng, L. Dai, J. Peng, S. Chen, *Nano Lett.* **2014**, *14*, 3550.

[160] F. Wu, N. Li, Y. Su, H. Shou, L. Bao, W. Yang, L. Zhang, R. An, S. Chen, *Adv. Mater.* **2013**, *25*, 3722.

[161] S. H. Kang, M. M. Thackeray, *Electrochem. commun.* **2009**, *11*, 748.

[162] B. Song, M. O. Lai, Z. Liu, H. Liu, L. Lu, *J. Mater. Chem. A* **2013**, *1*, 9954.

[163] F. Zheng, C. Yang, X. Xiong, J. Xiong, R. Hu, Y. Chen, M. Liu, *Angew. Chemie Int. Ed.* **2015**, *54*, 13058.

[164] L. Li, B. H. Song, Y. L. Chang, H. Xia, J. R. Yang, K. S. Lee, L. Lu, *J. Power Sources* **2015**, *283*, 162.

[165] D. Ye, K. Ozawa, B. Wang, D. Hulicova-Jurcakova, J. Zou, C. Sun, L. Wang, *Nano Energy* **2014**, *6*, 92.

[166] X. Feng, Z. Yang, D. Tang, Q. Kong, L. Gu, Z. Wang, L. Chen, *Phys. Chem. Chem. Phys.* **2015**, *17*, 1257.

[167] L. S. Cahill, S.-C. Yin, A. Samoson, I. Heinmaa, L. F. Nazar, G. R. Goward, *Chem. Mater.* **2005**, *17*, 6560.

[168] I. Hung, L. Zhou, F. Pourpoint, C. P. Grey, Z. Gan, *J. Am. Chem. Soc.* **2012**, *134*, 1898.

[169] F. de Groot, A. Kotani, *Core Level Spectroscopy of Solids*, CRC Press, **2008**.

[170] H. Ikeno, I. Tanaka, Y. Koyama, T. Mizoguchi, K. Ogasawara, *Phys. Rev. B,* **2005**, *72*, 075123.

[171] Y. Koyama, T. Mizoguchi, H. Ikeno, I. Tanaka, *J. Phys. Chem. B* **2005**, *109*, 10749.

[172] C. P. Grey, N. Dupre, *Chem. Rev.* **2004**, *104*, 4493.

[173] D. Zeng, J. Cabana, J. Bréger, W.-S. Yoon, C. P. Grey, *Chem. Mater.* **2007**, *19*, 6277.

[174] J. H. Paterson, O. L. Krivanek, *Ultramicroscopy* **1990**, *32*, 319.

[175] J. van Elp, J. L. Wieland, H. Eskes, P. Kuiper, G. A. Sawatzky, F. M. F. de Groot, T. S. Turner, *Phys. Rev. B*, **1991**, *44*, 6090.

[176] J.-H. Cheng, C.-J. Pan, J.-F. Lee, J.-M. Chen, M. Guignard, C. Delmas, D. Carlier, B.-J. Hwang, Chem. Mater. **2014**, *26*, 1219.

[177] S. Hwang, W. Chang, S.Kim, D. Su, D. H. Kim, J. Y. Lee, K. Y. Chung, E. A. Stach, *Chem. Mater.* **2014**, *26*, 1084.

[178] G. Alva, C. Kim, T. H. Yi, J. B. Cook, L. P. Xu, G. M. Nolis, J. Cabana, *J. Phys. Chem. C* **2014**, *118*, 10596.

[179] J. Bréger, M. Jiang, N. Dupré, Y. S. Meng, Y. Shao-Horn, G. Ceder, C. P. Grey, *J. Solid State Chem.* **2005**, *178*, 2575.

[180] A. Boulineau, L. Croguennec, C. Delmas, F. Weill, *Chem. Mater.* **2009**, *21*, 4216.

[181] J. Bréger, N. Dupré, P. J. Chupas, P. L. Lee, T. Proffen, J. B. Parise, C. P. Grey, *J. Am. Chem. Soc.* **2005**, *127*, 7529.

[182] J. Breger, K. Kang, J. Cabana, G. Ceder, C. P. Grey, *J. Mater. Chem.* **2007**, *17*, 3167.

[183] L. S. Cahill, S. C. Yin, A. Samoson, I. Heinmaa, L. F. Nazar, G. R. Goward, *Chem. Mater.* **2005**, *17*, 6560.

[184] M. Gu, A. Genc, I. Belharouak, D. Wang, K. Amine, S. Thevuthasan, D. R. Baer, J. Zhang, N. D. Browning, J. Liu, C. Wang, *Chem. Mater.* **2013,** *25*, 2319.

[185] D. Qian, B. Xu, M. Chi, Y. S. Meng, *Phys. Chem. Chem. Phys.* **2014**, *16*, 14665.

[186] D. Mohanty, S. Kalnaus, R. A. Meisner, K. J. Rhodes, J. Li, E. A. Payzant, D. L. Wood, C. Daniel, *J. Power Sources* **2013**, *229*, 239.

[187] M. Sathiya, A. M. Abakumov, D. Foix, G. Rousse, K. Ramesha, M. Saubanère, M. L. Doublet, H. Vezin, C. P. Laisa, A. S. Prakash, D. Gonbeau, G. VanTendeloo, J.-M. Tarascon, *Nat. Mater.* **2015**, *14*, 230.

[188] A. D. Robertson, A. R. Armstrong, P. G. Bruce, *Chem. Mater.* **2001**, *13*, 2380.

[189] D. Seo, J. Lee, A. Urban, R. Malik, S. Kang, *Nat. Chem.* **2016**, *8*, 692.

[190] M. D. Uchic, M. A. Groeber, D. M. Dimiduk, J. P. Simmons, *Scr. Mater.* **2006**, *55*, 23.

[191] D. J. Jensen, E. M. Lauridsen, L. Margulies, H. F. Poulsen, S. Schmidt, H. O. Sørensen, G. B. M. Vaughan, *Mater. Today* **2006**, *9*, 18.

[192] T. Link, S. Zabler, A. Epishin, A. Haibel, M. Bansal, X. Thibault, *Mater. Sci. Eng. A* **2006**, *425*, 47.

[193] W. Ludwig, P. Reischig, A. King, M. Herbig, E. M. Lauridsen, G. Johnson, T. J. Marrow, J. Y. Buffire, *Rev. Sci. Instrum.* **2009**, *80*, 033905.

[194] P. Pietsch, V. Wood, *Annu. Rev. Mater. Res* **2017**, *471229*, 1.

[195] A. C. Lewis, A. B. Geltmacher, *Scr. Mater.* **2006**, *55*, 81.

[196] M. A. Mangan, G. J. Shiflet, *J. Microsc.* **1997**, *188*, 36.

[197] J. Lin, W. Heeschen, J. Reffner, J. Hook, *Microsc. Microanal.* **2012**, *18*, 266.

[198] L. A. Giannuzzi, F. A. Stevie, *Introduction To Focused Ion Beams,* Springer, **2005**.

[199] L. Holzer, B. Muench, M. Wegmann, P. Gasser, R. J. Flatt, *J. Am. Ceram. Soc.* **2006**, *89*, 2577.

[200] B. Munch, P. Gasser, L. Holzer, R. Flatt, *J. Am. Ceram. Soc.* **2006**, *89*, 2586.

[201] M. Ebner, F. Marone, M. Stampanoni, V. Wood, *Science* **2013**, *342*, 716.

[202] P. R. Shearing, L. E. Howard, P. S. Jørgensen, N. P. Brandon, S. J. Harris, *Electrochem. commun.* **2010**, *12*, 374.

[203] B. Yan, C. Lim, L. Yin, L. Zhu, *J. Electrochem. Soc.* **2012**, *159*, A1604.

[204] Y. K. Chen-Wiegart, Z. Liu, K. T. Faber, S. A. Barnett, J. Wang, *Electrochem. commun.* **2013**, *28*, 127.

[205] F. Tariq, V. Yufit, M. Kishimoto, P. R. Shearing, S. Menkin, D. Golodnitsky, J. Gelb, E. Peled, N. P. Brandon, *J. Power Sources* **2014**, *248,* 1014.

[206] J. Gonzalez, K. Sun, M. Huang, J. Lambros, S. Dillon, I. Chasiotis, *J. Power Sources* **2014**, *269*, 334.

[207] L. Zielke, T. Hutzenlaub, D. R. Wheeler, I. Manke, T. Arlt, N. Paust, R. Zengerle, S. Thiele, *Adv. Energy Mater.* **2014**, *4*, 1301617.

[208] L. Zielke, T. Hutzenlaub, D. R. Wheeler, C.-W. Chao, I. Manke, A. Hilger, N. Paust, R. Zengerle, S. Thiele, *Adv. Energy Mater.* **2014**, 1401612.

[209] M. Ender, J. Joos, T. Carraro, E. Ivers-Tiffée, *Electrochem. commun.* **2011**, *13,* 166.

[210] M. Ender, J. Joos, T. Carraro, E. Ivers-Tiffee, *J. Electrochem. Soc.* **2012**, *159*, A972.

[211] Y. K. Chen-Wiegart, R. DeMike, C. Erdonmez, K. Thornton, S. A. Barnett, J. Wang, *J. Power Sources* **2014**, *249,* 349.

[212] J. R. Wilson, J. S. Cronin, S. A. Barnett, S. J. Harris, *J. Power Sources* **2011**, *196*, 3443.

[213] Z. Liu, J. Scott Cronin, Y. K. Chen-Wiegart, J. R. Wilson, K. J. Yakal-Kremski, J. Wang, K. T. Faber, S. A. Barnett, *J. Power Sources* **2013**, *227*, 267.

[214] D. E. Stephenson, B. C. Walker, C. B. Skelton, E. P. Gorzkowski, D. J. Rowenhorst, D. R. Wheeler, *J. Electrochem. Soc.* **2011**, *158*, A781.

[215] A. Gully, H. Liu, S. Srinivasan, A. K. Sethurajan, S. Schougaard, B. Protas, *J. Electrochem. Soc.* **2014**, *161*, E3066.

[216] B. Yan, C. Lim, L. Yin, L. Zhu, *Electrochim. Acta* **2013**, *100*, 171.

[217] M. Ebner, F. Geldmacher, F. Marone, M. Stampanoni, V. Wood, *Adv. Energy Mater.* **2013**, *3*, 845.

[218] H. Liu, J. M. Foster, A. Gully, S. Krachkovskiy, M. Jiang, Y. Wu, X. Yang, B. Protas, G. R. Goward, G. A. Botton, *J. Power Sources* **2016**, *306*, 300.

[219] C.-W. Wang, Y.-B. Yi, A. M. Sastry, J. Shim, K. A. Striebel, *J. Electrochem. Soc.* **2004**, *151*, A1489.

[220] D. Kehrwald, P. R. Shearing, N. P. Brandon, N. K. Sinha, S. J. Harris, *J. Electrochem. Soc.* **2011**, *158*, 7.

[221] M. Balasubramanian, X. Sun, X. Q. Yang, J. McBreen, *J. Power Sources* **2001**, *92*, 1.

[222] Z. Wang, D. Santhanagopalan, W. Zhang, F. Wang, H. L. Xin, K. He, J. Li, N. Dudney, Y. S. Meng, *Nano Lett.* **2016**, 16, 3760.